UCLouvain

epl

École polytechnique de Louvain

Topology optimization of the conductive track of an electrodynamic suspension for MAGLEV trains

Author: **Thomas Derneden**
Supervisor: **Bruno Dehez**
Readers: **Christophe Craeye, Louis Beauloye**
Academic year 2023–2024
Master [120] in Electro-mechanical Engineering

Acknowledgements

Je tiens à exprimer ma profonde gratitude à toutes les personnes qui ont contribué à la réalisation de ce mémoire.

Tout d'abord, je souhaite exprimer mes remerciements les plus sincères à mon promoteur, le Professeur Bruno Dehez, pour son encadrement, ses conseils, et son soutien constant tout au long de ce travail. Son engagement envers le projet, lors de nos nombreuses réunions, a été un élément essentiel pour mener à bien cette recherche.

Je souhaite également remercier chaleureusement Louis Beauloye pour son accompagnement rigoureux et son dévouement sans faille. Sa disponibilité et son écoute ont été d'une aide précieuse, surtout lors des moments où j'ai rencontré des difficultés. Toujours prêt à discuter et à m'aider à surmonter les blocages, son soutien a joué un rôle crucial dans l'avancement et la finalisation de ce mémoire.

Enfin, je tiens à exprimer ma gratitude à mes proches pour leur soutien, leur patience, et leurs encouragements tout au long de cette aventure. Leur présence à mes côtés a été une source de force et de sérénité indispensable pour mener à bien ce projet.

Utilisation de l'Intelligence Artificielle

L'intelligence artificielle, en particulier ChatGPT, a été utilisée dans ce travail comme un outil d'amélioration de l'écriture et de correction orthographique. Ce recours à l'IA a permis d'affiner la qualité rédactionnelle de ce mémoire.

Abstract

The growing demand for efficient and sustainable transportation systems, driven by the necessity for faster and more affordable travel, highlights the critical need for innovative technological solutions. Magnetic levitation (MAGLEV) technology, with its potential for high-speed travel combined with minimal environmental impact, emerges as a promising answer to these global challenges. This thesis presents a comprehensive approach to the topology optimization of conductive tracks for Electrodynamic Suspension (EDS) systems in MAGLEV trains, aiming to enhance performance while reducing material costs.

Central to this research is the development of advanced mathematical models based on equivalent electrical circuits, designed to accurately simulate the complex electromagnetic interactions inherent in Permanent Magnet Electrodynamic Suspension (PM-EDS) systems. These models, which include simplified and advanced plate models, were rigorously validated against Finite Element Method (FEM) simulations, demonstrating their capability to predict the behavior of the system under various operational conditions. The validated models serve as a robust foundation for the exploration and optimization of track topologies.

The study leverages density-based topology optimization techniques to explore innovative configurations of the conductive tracks. The primary objective of this optimization is to improve the Lift-to-Drag ratio (LDR), a key performance metric, and minimize material usage. The optimization results underscore the potential of novel track designs that could achieve significant improvements in performance, efficiency and cost.

The research also investigates intuitive topologies inspired by obtained results and prior knowledge. These intuitive designs provide complementary elements to potentially enhance the Topology Optimization (TO) results.

This work contributes to the advancement of MAGLEV technology by providing a detailed framework for the optimization of conductive tracks. The findings offer valuable pathways to developing more efficient and cost-effective high-speed rail systems, with the potential to impact the future of transportation.

Nomenclature

Abbreviations

AVM Adjoint Variable Method

EDS Electrodynamic Suspension

EDW Electrodynamic Wheels

EMF Electromotive Force

EMS Electromagnetic Suspension

FEA Finite Element Analysis

FEM Finite Element Methods

HPMA Halbach Permanent Magnet Array

KVL Kirchhoff Voltage Law

LDR Lift-to-Drag Ratio

LIM Linear Induction Motor

LSM Linear Synchronous Motor

LWR Lift-to-Weight Ratio

MAGLEV Magnetic Levitation

MIS Material Interpolation Scheme

MMA Method of Moving Asymptotes

PM Permanent Magnet

PM-EDS Permanent Magnet Electrodynamic Suspension

RAMP Rational Approximation of Material Properties

SCM SuperConducting Magnet

SIMP Simplified Isotropic Material with Penalization

TO	Topology Optimization	

Greek letters

$\boldsymbol{\lambda}$	Adjoint variable	
$\boldsymbol{\theta}$	Design variables	
δ_{skin}	Penetration depth	[m]
λ	Wavelength of PM array	[m]
μ	Magnetic permeability of the material	[H/m]
ω	Angular frequency	[rad/s]
ϕ_n	Magnetic flux through a discrete loop	[Wb]
ρ	Electrical resistivity of the material	$[\Omega m]$
σ	Electrical conductivity	[S/m]
τ_c	Coil pitch	[m]
τ_m	Pole pitch	[m]

Alpha numeric symbols

Δx	Discretization length along the x-axis	[m]
Δy	Discretization length along the y-axis	[m]
$\mathbf{B}$	Magnetic flux density	[T]
B_0	Peak magnetic flux density	[T]
J	Current density	$[A/m^2]$
N_m	Number of mutual inductances in the longitudinal direction	
N_w	Number of adjacent windows considered in the equivalent inductance computation in the advanced plate model	
p_{max}	Number of mutual inductances in the transverse direction	
t_c	Thickness of the track	[m]
t_m	Thickness of the permanent magnets	[m]
t_{ag}	Air gap thickness	[m]
v_x	Longitudinal velocity of the magnetic field	[m/s]
w_c	Width of the track	[m]

w_m	Width of the permanent magnets	[m]
$w_{tc} \times w_{lc}$	Cross-sectional area of the branches	[m^2]
E	Induced voltage	[V]
L	Inductance	[H]
R	Resistance	[Ω]

Contents

List of Figures

List of Tables

Chapter 1

Introduction

This chapter provides an introduction to Magnetic levitation (MAGLEV) transportation, setting the stage for research. It begins with a general overview, discussing the environmental and operational benefits of MAGLEV systems along with an initial look at some existing challenges. We then shift to a brief historical perspective, highlighting the evolution and current trends in MAGLEV globally. Detailed insights into the principal MAGLEV technologies, Electromagnetic Suspension (EMS) and Electrodynamic Suspension (EDS), are explored in Section 1.3, with the EDS technology being central in this study. The chapter concludes by clearly defining the objectives, scope, and methodology of the research.

1.1 Overview of MAGLEV Transportation Systems

As Lee, Kim, and Lee discuss in [16], as the global population increases and living areas expand, the limitations of traditional automobiles, air services, and other conventional transportation methods become apparent, especially for mass transit. This growing demand for rapid, reliable, safe, and efficient transport systems calls for innovative solutions that are sustainable, convenient, low-maintenance, and broadly applicable [18]-[4].

MAGLEV train technology, which is based on the use of magnetic forces from strategically placed magnets or electromagnets to levitate, guide and propel the vehicle electromechanically a short distance above the guideway, as shown in Fig. 1.1, represents a leap forward in transportation. The propulsion of such MAGLEV trains is assured by a linear motor, that can be either a Linear Induction Motor (LIM) or a Linear Synchronous Motor (LSM)[19]-[21]. This MAGLEV technology eliminates the need for traditional components such as wheels, axles, and bearings, offering speeds that traditional systems can't match with the added benefit of having a minimal environmental impact[16],[4],[22].

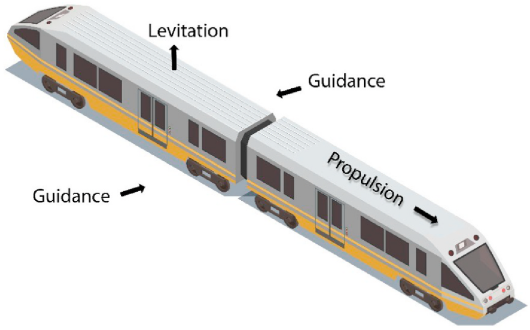

Figure 1.1: MAGLEV train Simplified Working Principle [1].

Unlike wheeled trains, which face limitations due to frictional wear and tear and the impact of weather conditions [16],[22], MAGLEV trains are designed to mitigate these challenges, offering a more durable and efficient mode of transport. The frictionless operation of MAGLEV trains circumvents issues like mechanical strain and deterioration caused by friction encountered by high-speed conventional trains, promising higher speeds without the associated rapid wear of components, thus reducing maintenance costs [23],[24].

MAGLEV trains also provide several additional benefits. They operate without wheels, drastically reducing noise and vibrations and inherently preventing derailments [1],[22],[3], which enhances safety. Even in the event of malfunctions, emergency systems can be readily implemented [25]. Their superior performance in terms of acceleration and deceleration facilitates better hill-climbing capabilities, and they require smaller radii for curves. This flexibility allows for more relaxed route selection criteria, ultimately reducing construction costs as mentioned by Kim et al. [4].

Evidence of MAGLEV's superiority can be seen in Table 1.1, illustrating a clear comparison between MAGLEV and traditional wheel-on-rail systems. While MAGLEV technology offers substantial advancements in transportation, several challenges still require attention.

Safety considerations and comfort are paramount in the operation of MAGLEV trains notably due to the intense magnetic fields produced by the electromagnets and superconducting magnets that drive their levitation and propulsion systems. While these magnetic intensities are kept within human safety thresholds, as mentioned in [16], they may still adversely affect the comfort of passengers. To alleviate these concerns and improve passenger experience, it is vital to implement robust magnetic shielding methods. Techniques like integrating iron sheets [26],[27] or using Halbach permanent magnet arrays [23][28]-[30] are effective in diminishing magnetic field exposure, thereby enhancing safety and comfort aboard MAGLEV trains.

Table 1.1: MAGLEV Trains and Traditional Wheel-On-Rail Systems Characteristics, adapted from [16],[1],[17].

Performance	MAGLEV Train	On-Wheel-Rail Systems
Speed domain	Medium-low speed: 80–200 km/h Medium speed: 200–400 km/h High speed: 400–1000 km/h	High-speed trains: 250–350 km/h Subway: 30–60 km/h Light rail: 40 km/h Monorail: 20–35 km/h
Maintenance	1.2% of the total investment	4.4% of the total investment
Noise	No mechanical contact 60–65 dB	Contact between wheels and rails, 75–80 dB
Curve	In 30 m in radius	In 150 m in radius
Grade	About 80–100/1000	About 30–50/1000
Safety	No possible derailment	Derails from minor defects
Specific energy consumption	45–54 Wh/pl/km	48.5–59 Wh/pl/km
Cost of construction	High	Low
Energy consumption	Very little	Mechanical resistance and wheel-rail resistance
Service life	The life of rail is 80 years, and the life of vehicle is 35 years	The life of rail is less than 50–60 years, and the life of vehicle is 20–25 years
Mode of track change	High difficulty and cost	Simple and low cost

Additionally, the term "MAGLEV" not only refers to the vehicles but also to the specialized railway systems they depend on. These technologies often face compatibility issues with traditional wheeled train systems and conventional rail tracks, necessitating the development of entirely new infrastructure for MAGLEV operations. Among these challenges is the difficulty in achieving smooth and easy branching within the MAGLEV guideways [31], a significant technical hurdle that is always being actively researched [23].

1.2 Historical Point

The realm of MAGLEV technology is always evolving with ambitious projects [32],[33], including the notable development of Japan's Tokyo-to-Osaka MAGLEV line. Anticipated to be operational by 2037, this line aims to dramatically reduce travel times using an EDS MAGLEV train that utilizes the superconductive null-flux method [7] known as the MLX [34]-[38], as depicted in Fig. 1.2.

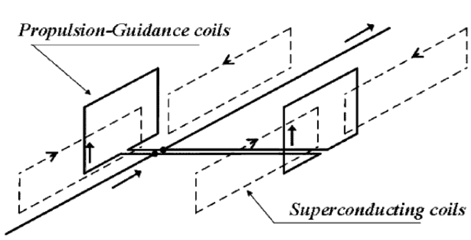

(a) Propulsion-guidance coils [16].

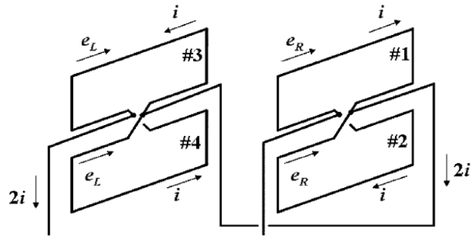

(b) Levitation-guidance coils [16].

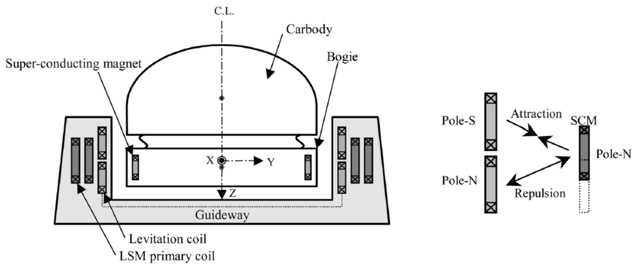

(c) Working Principle [38].

Figure 1.2: Japanese MAGLEV MLX principle.

Concurrently, advancements in MAGLEV technology were not limited to Japan. Starting in 1969, the German company Krauss-Maffei developed the world's inaugural MAGLEV train model, demonstrating the feasibility of electromagnetic levitation with a modest setup [22]. This pioneering model paved the way for subsequent developments, including the successful implementation of the TR08, that will give birth to the Shanghai Transrapid shown in Fig 1.3. This train operates on the line from Shanghai Pudong Airport to Longyang Road subway station and marked the inauguration of the world's first commercial MAGLEV line [39]-[41].

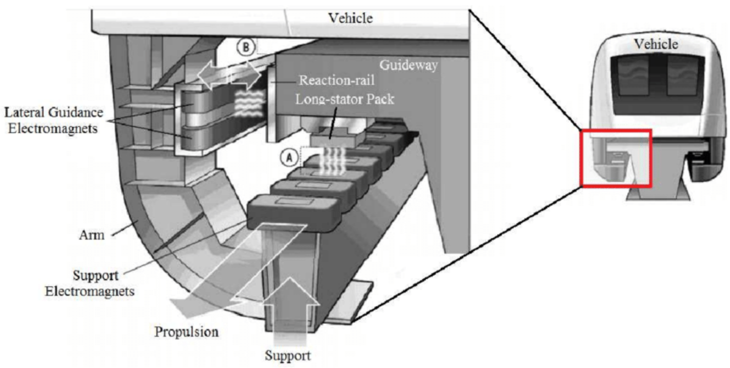

Figure 1.3: Transrapid Principle [2].

Following Germany's lead, Japan acquired the TR04, leading to the development of the low-speed MAGLEV train HSST, depicted in Fig. 1.4, which has been operational since March 2005 near Nagoya in Aichi Prefecture. South Korea also embraced MAGLEV technology to address urban traffic challenges, culminating in the development of the low-speed MAGLEV train UTM [42]. By 2006, Korea initiated commercial operations of this train at Incheon International Airport, highlighting the successful integration of MAGLEV technology into urban infrastructure. In 2016, the Ecobee MAGLEV train, shown in Fig. 1.5, began service, exemplifying this progress [43].

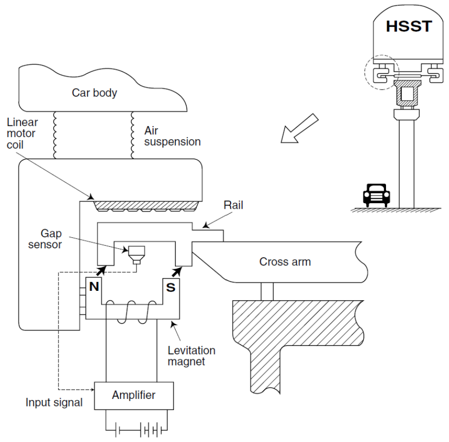

Figure 1.4: HSST MAGLEV System Description [3].

Figure 1.5: ECOBEE, Korean's MAGLEV Train [4].

The development of MAGLEV transportation over the past century underscores a significant journey of innovation, initiated by German engineer Hermann Kemper in 1922. Despite early challenges, significant progress by the late 20th century transitioned MAGLEV from a theoretical concept to a practical application [22].

The appeal of MAGLEV systems is rooted in their operational efficiency. However, the considerable expense involved in constructing MAGLEV lines, with costs of several dozens of millions of dollars per mile, presents a significant obstacle. This financial hurdle has resulted in the cancellation of many projects. While the operational costs of MAGLEV trains are generally lower than those of traditional rail systems, the initial investment has sparked ongoing debates among critics and supporters about the feasibility of broad MAGLEV deployment [31].

1.3 Classification of MAGLEV Trains Technologies

The two primary technologies in MAGLEV train systems are EMS and EDS, each with distinct mechanisms and applications.

As said in Section 1.2, MAGLEV technology evolved from conceptual designs to practical applications. Nowadays, the attention has increasingly turned towards optimizing system components for better performance and reduced environmental impact. After introducing the two principal MAGLEV technologies—EMS and EDS—this study delves into EDS technology. Specifically, this study explores the optimization of EDS track designs. The existing track designs will be extensively reviewed in Chapter 2. Starting with a ladder type of track, then reaching conductive sheet guideways and progressing toward identifying alternative track topologies, this study aims at finding topologies that enhance system performance and cost-efficiency.

1.3.1 Electromagnetic Suspension (EMS)

EMS technology utilizes the attractive force between onboard electromagnets and a ferromagnetic guideway. This technology is characterized by its requirement for precise air-gap control to maintain a consistent separation of approximately 8-10 mm between the train and the track. The control of this air gap is critical, especially as train speeds increase, making the maintenance of stability more challenging. However, in terms of technical implementation, EMS is often considered simpler compared to EDS [16][1]-[22].

EMS can be further divided based on the integration of levitation and guidance systems [16]. The integrated type, exemplified by Japan's HSST and Korea's UTM systems [42], combines these functions of levitation and guidance to reduce costs and complexity but faces challenges at higher speeds. In contrast, the separated type, such as Germany's Transrapid, uses distinct mechanisms for levitation and guidance, which is advantageous for high-speed operations as it minimizes interference but requires more controllers, potentially increasing complexity and cost, as mentioned by Lee, Kim, and Lee in [16].

1.3.2 Electrodynamic Suspension (EDS)

Conversely, EDS is based on repulsive forces generated by the interaction of onboard magnets (either permanent magnets (PM) or superconducting magnets (SCM)) with conducting coils on the guideway or a conductive sheet used as the guideway [44],[6]. The relative movement of the magnetic field induces current in the track. Subsequently, the moving field produces a lift force by interacting with the induced current [22]. This system is inherently stable and does not require active control of the air gap. With a typical air gap of around 100 mm, EDS systems are reliable and can accommodate various types of loads [16],[4],[45].

EDS is particularly suited for high-speed MAGLEV trains because it supports higher speeds without the need for precise track and levitation control

[36],[46]. However, EDS trains require a minimum speed (around 100 km/h) to generate sufficient levitation forces, necessitating the use of auxiliary wheels at lower speeds. This also means that infrastructure capable of handling the low-speed regime must be present along the entire track to accommodate emergency stops.

When it comes to the magnetic field source, in this study, the focus is on EDS using PMs, specifically referred to as Permanent Magnet Electrodynamic Suspension (PM-EDS). This suspension system is made possible thanks to the adoption of rare-earth permanent magnets capable of generating sufficiently strong magnetic fields to levitate MAGLEV vehicles [6]. Additionally, the integration of Halbach Arrays is being explored for their ability to enhance EDS performance by more effectively concentrating the magnetic field [47]-[51], as discussed in Section 1.1. Although SCM are prevalent in EDS applications, their reliance on elaborate and expensive cooling solutions introduces additional complexity.

1.3.3 Operational Considerations and System Comparisons

While EMS offers the advantage of operating effectively across all speeds, including starting levitating from a stationary position, it does suffer from higher energy consumption due to the need for constant air gap control [18],[17]. This is less of an issue with EDS, which operates more efficiently at high speeds but cannot provide levitation at low speeds or when stationary.

The financial implications of both technologies also differ significantly. The construction and maintenance costs of EMS systems are influenced by the complexity of the electromagnetic systems required for operation. In contrast, EDS systems tend to have higher initial setup costs due to the use of expensive superconducting materials, but potentially lower long-term maintenance costs.

With all of that said, it is important to note that the realm of MAGLEV trains, regardless of the technology used (EMS or EDS), is continually being explored with increasing depth [32],[33],[52]. Research and developments are occurring globally, consistently yielding new findings and advancements that enhance the viability and efficiency of MAGLEV technologies.

1.4 Objectives and Scope of the Study

This study explores the potential for advancements in the optimization of track topologies for PM-EDS MAGLEV trains. Grounded in electrical circuit theory, it aims to develop a robust mathematical model capable of simulating existing track designs and discovering innovative configurations that could enhance system performance and efficiency. This model will allow for a detailed examination of how changes in design can influence overall system dynamics.

The primary goal is to create optimized topologies for PM-EDS MAGLEV rails that effectively integrate theoretical insights with practical design enhancements. This study utilizes Topology Optimization (TO) methods to identify track designs that not only improve operational efficiency and performances but also prioritize material reduction to support environmental sustainability. By achieving these design improvements, the model is expected to facilitate the development and choice of rail designs, potentially participating in enhancing the overall performance of PM-EDS MAGLEV systems.

1.5 Research Methodology

The research began with the development of a mathematical model utilizing equivalent electrical circuit principles. To streamline the computations, the model was based on a ladder track configuration model, an already established analytical model used in PM-EDS systems and that will be discussed in Chapter 2. This initial model served as a baseline, enabling basic simulation of track interactions and was validated using *Comsol Multiphysics*® to ensure its accuracy and reliability.

Building upon the validated ladder track model, the research progressed to a simplified conductive plate model. This model allowed for the simulation of more detailed interactions within the track system. An advanced plate track model was then developed, which included variations such as the introduction of 'holes'—alterations in the density of elements within the electrical equivalent circuit's mesh to simulate potential material and geometric optimizations. Both configurations, with and without these density variations, were validated using a *Comsol Multiphysics*® model to confirm their effectiveness.

The core of the research involved TO method, where a simplified density-based approach was employed to explore a wide array of track configurations. The goal was not to produce designs ready for immediate manufacturing but to discover innovative and efficient topologies. The optimization process utilized the Method of Moving Asymptotes (MMA), with gradient calculations performed using the Adjoint Variable Method (AVM). This will further be discussed in Chapter 6.

Multiple optimization scenarios were executed, focusing on varying objectives such as minimizing drag while maintaining lift force, and adjusting the density of elements in the mesh to create holes and hence possibly uncover new EDS track topologies.

In conclusion, this research aimed to advance the design of PM-EDS MAGLEV track systems and laid the groundwork for future work in this area. The methodologies developed and insights gained may opened new opportunities for improving both the sustainability and efficiency of MAGLEV systems in future work ultimately leading to more practical and effective implementations worldwide.

Chapter 2

State of the Art in PM-EDS Track Topologies

This chapter provides a review of the research and developments in PM-EDS track topologies for MAGLEV systems. It reviews the literature and studies relevant to the design and optimization of EDS tracks, establishing the context for this thesis. By exploring both continuous and discrete track types, the chapter highlights their technological implications, performance metrics, and the potential for cost reduction and environmental adaptability in MAGLEV transportation. This sets the stage for detailed investigations into optimizing EDS topologies in subsequent chapters of the thesis.

2.1 Optimization Considerations for PM-EDS Systems

In Section 1.3, EDS technology has already been reviewed and explained. In this subsection, the aim is to emphasize the purpose and importance of optimizing the design of MAGLEV trains, which involves the choice of track topologies.

As noted by Thompson, Thornton, and Kondoleon in their 1999 study on flux-canceling electrodynamic MAGLEV suspension [53], the primary challenge in high-speed ground transportation—whether MAGLEV or traditional high-speed trains—is the cost associated with guideway construction. This issue of exorbitant initial costs [12] and complexity [54] has, as mentioned in Section 1.2, led many countries to cancel MAGLEV projects and instead continue upgrading existing rail systems and other forms of transportation.

Nevertheless, researchers agree that if the initial cost can be reduced [12], EDS MAGLEV technology could indeed become more cost-effective than traditional rail-on-wheel systems. Considering both the infrastructure installation and operating costs, as discussed in Section 1.1, it is clear that MAGLEV could potentially offer a cost-effective solution with lower maintenance, reduced energy consumption, and a more attractive travel time, thereby decreasing the capital cost per user [53].

In this context, it is clear that the successful design of an EDS system depends on minimizing initial costs, reducing operational expenses, and maintaining high efficiency to ensure very low power loss [53]. These aspects are directly related to the track topology and PM configuration, meaning the design of the propulsion and suspension systems.

Beyond cost, as mentioned in Section 1.1, comfort and safety also play a crucial role in the final design. EDS systems have inherent stability issues, being highly underdamped [53]. Therefore, it is necessary to introduce specific and practical damping measures for suspension control to ensure passenger comfort [55],[56].

In addition to the above considerations, as discussed in Section 1.1, reducing the magnetic field in passenger compartments is crucial for the design of MAGLEV trains. The arrangement of permanent magnets in PM-EDS systems significantly impacts this aspect and is therefore a key part of the design process. Common configurations for PM-EDS magnetic field source include an alternating pattern of magnetic poles with a back-iron to close the magnetic flux lines, as stated by Beauloye and Dehez in [6], but also the Halbach Permanent Magnet Array (HPMA), able to polarize the magnetic field in one preferred direction.

The HPMA creates a strong, periodic magnetic field on the track side to enhance levitation efficiency, while nearly canceling the field on the vehicle side [30],[57], as shown in Fig. 2.1. This setup provides greater comfort for passengers by avoiding disturbances to sensitive electronic equipment [30]. The different topologies of magnetic field source for PM-EDS are depicted in Fig. 2.2. As mentioned in Section 1.3, superconducting magnets can also be used but are more complex and costly. Therefore, PM-based configurations are preferred here as they simplify the system [57].

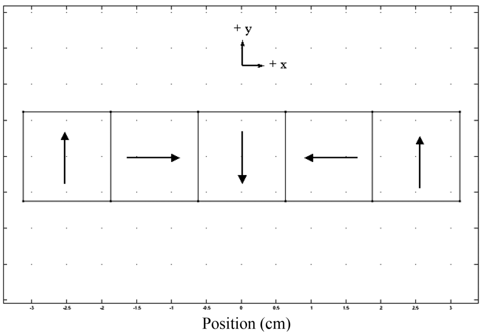

(a) Magnetization Orientation [5].

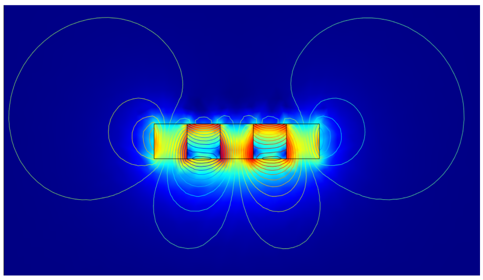

(b) Magnetic field color lines [5].

Figure 2.1: HPMA Principle [5].

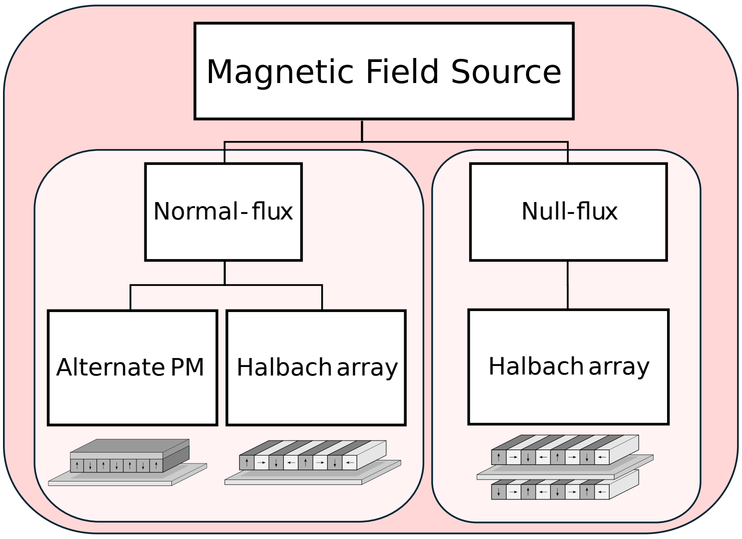

Figure 2.2: Magnetic Field Source Topologies for EDS systems (adapted from [6]).

Having reviewed the magnetic field source topologies, the attention is now turned toward track topologies, which are crucial for the performance and cost analysis of PM-EDS systems. Track topologies come in two main types: continuous and discrete tracks.

The various configurations of PM-EDS tracks are illustrated in Fig. 2.3, highlighting the differences between continuous and discrete types.

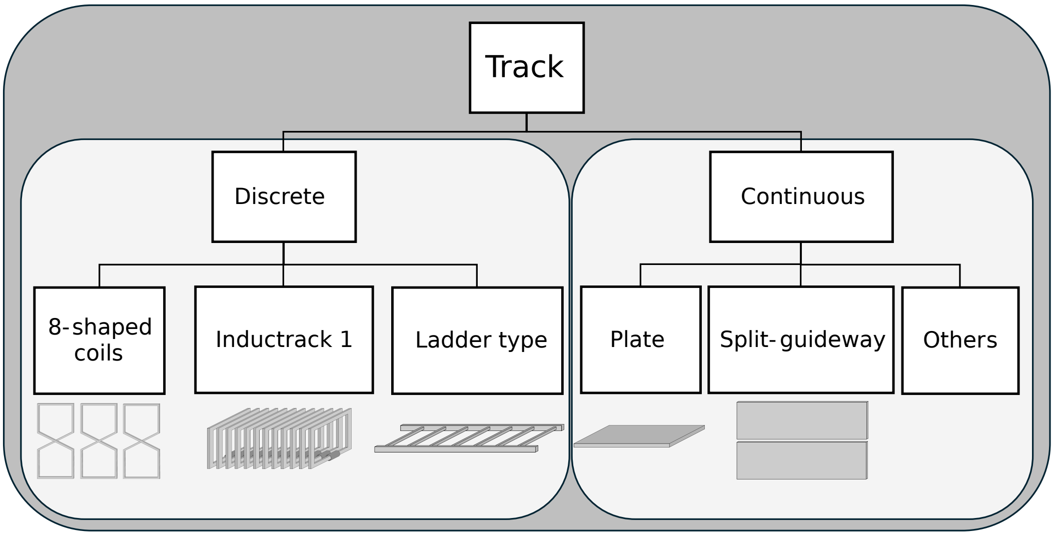

Figure 2.3: Track Topologies of EDS Systems (adapted from [6]).

- **Continuous Tracks :** Continuous tracks, as shown in Fig. 2.4a and 2.4b, are known for their simplicity and cost-effectiveness [12]. Typically made from uniform sheets of non-ferromagnetic conductive material [30], such as aluminum or copper, these tracks reduce initial costs by enabling easier manufacturing processes, being simpler to install [10], even in already existing infrastructures. Their flat shape, as mentioned by Bird and Lipo [12], offers significant advantages in terms of electromagnetic directional switches, maintenance costs, and reliability.

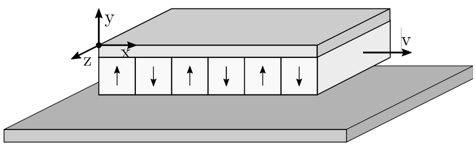

(a) Conductive Sheet, Plate track [6].

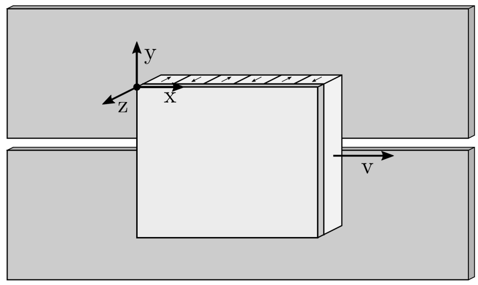

(b) Split-Guideway [6].

Figure 2.4: Continuous Track Configurations [6].

- **Discrete Tracks :** Discrete tracks, as opposed to continuous topologies, have complex design, and most of the time due to their complexity, result in higher initial costs. As the name suggests, these tracks can consist of repeated separate loops made of conductive [10], as seen in Fig. 2.5b and 2.5c. These loops can also be interconnected, as is the case with ladder-type tracks (see Fig. 2.5a), and can even be superposed in some cases [6].

2.1.1 Performance and Cost Assessment Metrics

After mentioning the different configurations for the magnetic field source and tracks, this section will discuss the assessment of the performance and cost-effectiveness of PM-EDS systems. To choose the optimal design for a specific application, associating a magnetic field source configuration with a track configuration, it is essential to use tools to evaluate the performance of the design. One of the most commonly used performance indicators is the Lift-to-Drag ratio, noted as LDR and defined as:

$$LDR = \frac{F_{lift}}{F_{drag}} \tag{2.1}$$

This LDR indicator is based on the lift (F_{lift}) and drag forces (F_{drag}). The lift force allows the MAGLEV train to levitate, while the drag force opposes its motion. Fig. 2.6 illustrates these forces acting on a moving PM above the track for a discrete and continuous configuration. They are generated through the interaction between the conductive track and the train's magnetic field.

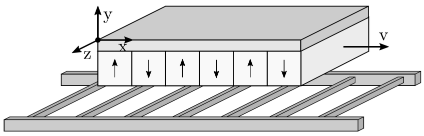

(a) Ladder-type [6].

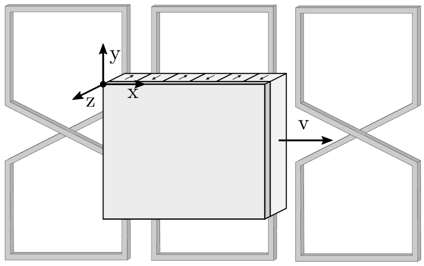

(b) 8-shaped coils [6].

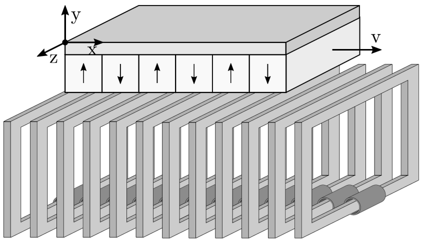

(c) Inductrack [6]

Figure 2.5: Discrete Track Configurations [6].

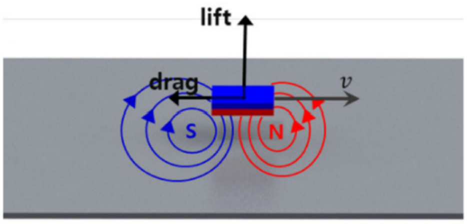

(a)

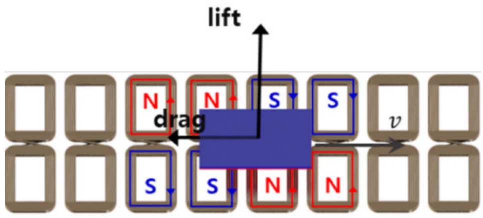

(b)

Figure 2.6: Lift and Drag forces acting on a PM moving above two track configurations a) conductive sheet, b) 8-shaped coils [7].

As discussed in Section 1.3.2, the relative movement of the permanent magnets above the track induces Eddy currents within it. These induced currents will then interact with the train's magnetic field, resulting in those two forces [6]. The behavior of these forces with respect to speed is generally consistent across all PM-EDS configurations and is illustrated in Fig. 2.7.

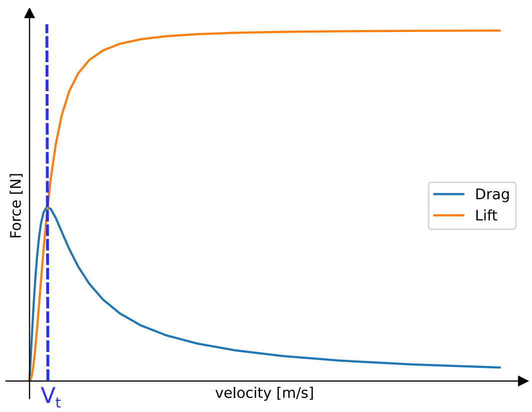

Figure 2.7: Lift and Drag Forces Variation with Speed in an EDS System.

The LDR provides insight into the long-term efficiency and operational cost of the system at a given speed. A high LDR indicates enhanced performance, with a large levitation force and low resistive force. While the LDR at high speed is vital for understanding operational efficiency, it is also important to consider other indicators to gain a comprehensive view of the system's performance and cost-effectiveness. One such indicator is the Lift-to-Weight Ratio, noted LWR, presented by Beauloye and Dehez in [6] and further developed in their subsequent paper [10]. This indicator is more related to the initial cost and material use by providing insights into the lift force per unit weight of the permanent magnets:

$$LWR = \frac{F_{lift}}{W_{PM}} \tag{2.2}$$

In addition, the "figure of merit" (f_m) can be considered. Developed by Chen and Feng in [8], it is a dimensionless indicator that integrates various influential factors for evaluating the performance of a MAGLEV system at a given speed. They defined it as follows:

$$f_m = 2\pi h_{eff} \sqrt{\frac{F_{lift}}{\mu_0 I^2} \frac{F_{lift}}{v_x F_{drag}} \frac{1}{\mu_0 \sigma V}} \tag{2.3}$$

where:

- v_x is the velocity of the vehicle,
- σ is the conductivity of the guideway material,
- V is the volume per meter of the guideway material,
- F_{drag} is the drag force,
- F_{lift} is the lift force,
- h_{eff} is the effective distance between the vehicle and the guideway.

This indicator gives insights on the long-term efficiency and power dissipation by using the LDR in the second term $\frac{F_{lift}}{v_x F_{drag}}$. It also encompasses material cost with the last term $\frac{1}{\mu_0 \sigma V}$. Hence, it can be seen as integrating both long-term operational cost and initial cost.

In the design process, it is crucial to consider both the initial cost, which can be related to the LWR, and the long-term operational cost, which can be related to the LDR. Finding a balance between these factors is essential to achieve the desired performance and cost in the design of an PM-EDS system for a given application. Using the f_m indicator can also provide valuable insights. Of course, when assessing the performance of a configuration using these indicators, it is important to consider the entire range of velocities, as these indicators will vary with respect to speed.

Next, a succinct review and comparison of the different track topologies will be done to provide more context for this study. This review aims to highlight key aspects and performance metrics of various configurations without delving into exhaustive detail. For a more comprehensive analysis and in depths optimization of these configurations, readers are encouraged to refer to the following detailed studies: [6],[30],[12],[54],[57]-[11].

2.1.2 Focus on Discrete Tracks

Ladder type track

The ladder track configuration is a type of PM-EDS track consisting of longitudinal conductive bars interconnected by transverse rungs, as seen in Fig. 2.5a. This type of track has been extensively analyzed, demonstrating its performance compared to other types of tracks. Beauloye and Dehez show in [10] that the ladder track can offer a very high lift force and a high LWR but a quite low LDR. Additionally, a large body of research, including [54] and [8], aims at optimizing their performance by varying the design and observing the changes in the electromagnetic interaction between the track and the magnetic field source.

In [8], Chen and Feng varied the thickness of the ladder's rungs and the coil pitch which is the distance between the centers of two consecutive coils in the guideway and will be noted as τ_c in the next chapters, to observe the impact on system performance based on the figure of merit. A simplified schematic representing these parameters on the ladder guideway is presented in Fig. 2.8. Their findings indicate that the best performance for ladder tracks is achieved with a length-to-width ratio of one and using thick transverse and longitudinal bars.

Additionally, Akinbiyi et al. in [54] investigated the effects of varying the pole pitch, which is the distance between the centers of two consecutive magnetic poles of the same polarity in a permanent magnet array and will be noted as τ_m in the next chapters, relative to the coil pitch τ_c. In Fig. 2.9, a schematic of a ladder-type track with HPMA above it is depicted. In this schematic, τ_c and the wavelength of the array field (λ) are indicated. Typically, τ_m corresponds to half the wavelength or half the period of the PMs.

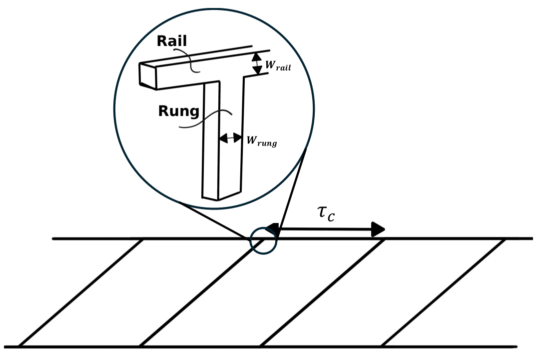

Figure 2.8: Simplified stick schematic of the ladder track and dimensions (adapted from [8]).

The authors highlighted the need to find a balance between a large ratio $\frac{\tau_m}{\tau_c}$, which offers a high lift force and small fluctuations in the levitation force for a low LDR, and a smaller ratio, which provides a lower lift force and larger fluctuations in the levitation force for a higher LDR.

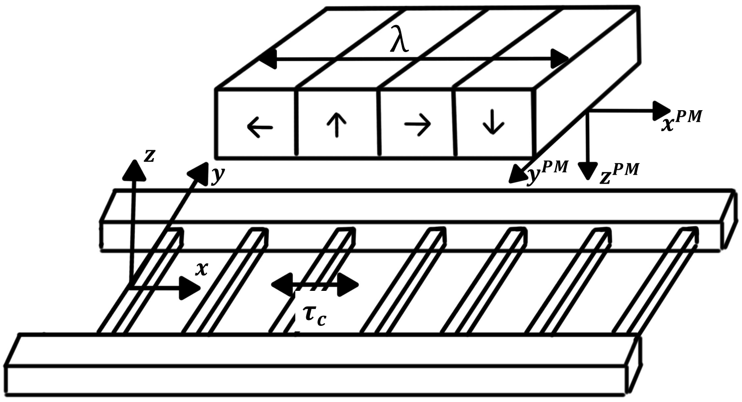

Figure 2.9: Simplified model of a HPMA above a the ladder track (inspired by [9]).

Physically, a smaller $\frac{\tau_m}{\tau_c}$ can be seen as reducing the length between two transverse bars. It has been shown that the transverse bars primarily influence the drag, while the lift is mostly influenced by the longitudinal bars [8]. Hence, reducing the ratio can be seen as having more transverse bars per pole pitch, which increases the drag and negates the increase in lift. Therefore, a smaller ratio, longer coil lengths, tends to decrease the drag force and result in a higher LDR [54].

In the case of the ladder track, the behavior observed in Fig. 2.7 can be explained easily. For discrete tracks, each loop can be represented using a filament model, as introduced by Hoppie [8],[59]. By using a lumped parameter equivalent circuit [9], as shown in Fig. 2.10, it is possible to represent the loops with parameters R, L, and E, which stand for the global resistance, inductance, and induced back-electromotive force respectively, as demonstrated by Beauloye and Dehez [6]. The authors demonstrated that this simple model allows us to derive expressions linking the lift and drag forces to the reactive and active power:

$$\mathbf{F}_{\text{drag}} = \frac{P}{v} = \frac{1}{v}\frac{E^2 R}{R^2 + (\omega L)^2} \tag{2.4}$$

$$\mathbf{F}_{\text{lift}} = \frac{Q}{v} = \frac{1}{v}\frac{E^2 \omega L}{R^2 + (\omega L)^2} \tag{2.5}$$

A detailed explanation of how these equations account for the behavior of lift and drag forces with respect to speed in discrete tracks can be found in Beauloye [6]. It is shown that, increasing the inductive effects help in achieving better operational efficiency. This idea will be discussed further in the context of inductive loading in the Inductrack configuration (see Fig. 2.5c).

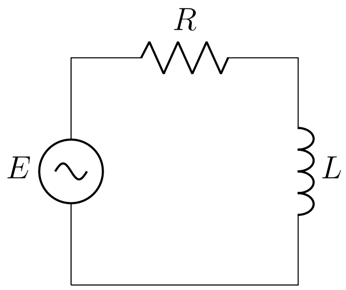

Figure 2.10: Lumped parameters equivalent circuit.

Inductrack

The Inductrack configuration, depicted in Fig. 2.5c, integrates a Halbach Permanent Magnet Array mounted on the vehicle, which interacts with a track composed of a longitudinally packed array of shorted coils [6],[57],[58]. The use of the HPMA enhances the system performances by optimizing the magnetic field distribution and focusing a strong magnetic field onto the track. This configuration is capable of achieving very high LDR, reaching values of 200:1 and more at operational speeds [57],[58].

In [57], Post and Ryutov developed an analytical model based on circuit theory and derived an expression for the LDR as:

$$LDR = \frac{F_{lift}}{F_{drag}} = \frac{\omega L}{R} = \frac{2\pi v_x}{\lambda}\left[\frac{L}{R}\right] \tag{2.6}$$

With the excitation frequency, ω, determined by the wavelength of the Halbach array field, λ [m]. This expression shows that the LDR increases monotonically with velocity, while the drag varies inversely with velocity at high speed.

The authors also introduced a quantity called the transition velocity, denoted as v_t. This velocity corresponds to the point where the lift and drag forces are equal and is shown in Fig. 2.7 with the dashed vertical bar. A low transition velocity generally indicates that the system can levitate the vehicle at very low speeds because the lift reaches a higher value much faster, significantly enhancing the system's performance and efficiency. In the case of the Inductrack, this transition velocity can be as low as a few kilometers per hour, allowing the lift forces to increase rapidly and stabilize at a high value at relatively low speeds, while the drag forces decrease quickly as the system approaches its operational speed.

This configuration offers numerous advantages, including low levitation speed and a high LDR, which leads to high operational efficiency. It is an ideal choice for MAGLEV train applications requiring quick starts, high speeds, and efficiency. In this type of setup, an inductive loading can be done by adding ferromagnetic material to the lower side of the coil, as it can be seen in Fig.

2.5c, further increasing the LDR as mentioned in the subsection concerning the ladder topology [6]. However, it does reduce the maximal levitation force achievable per unit area [57].

Despite these advantages, the configuration can be costly due to the amount of conductive material required and it's really low LWR indicator. They also exhibits inherently low, and even negative, lateral stiffness [6]. As a result, guiding systems are necessary, which introduces both initial and long-term costs that need to be considered.

The Inductrack is continuously being explored with new projects. Post and Ryutov, following their successful work detailed in [57] are now being sponsored by NASA for another small-scale design to investigate the feasibility of launching rockets using a MAGLEV track.

Simple discrete loops

The behavior of the simple discrete loops configuration, shown in Fig. 2.11, is very similar to the ladder-type track. In fact, the ladder track can be seen as a simple discrete loop configuration where the transverse bars are connected to one another [8]. In terms of LDR and LWR, in [10], Beauloye and Dehez consider the simple discrete loops configuration as a trade-off between the two previous track configurations, offering good performances and reducing the amount of materials compared to the Inductrack.

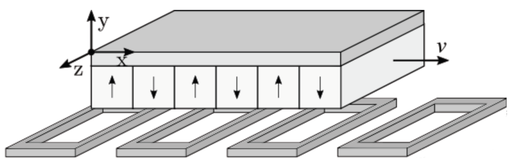

Figure 2.11: Simple discrete loops track [10].

8-shaped coils, Null-flux

The 8-shaped, null-flux coils configuration, as depicted in Fig. 2.5b, was introduced by Danby and Powell in 1966 [60],[61]. It was first based on the use of superconducting magnets and 8-shaped coils, called the ground coils. This initial proposition led to numerous new designs and improvements, including a practical implementation with the Japanese MAGLEV train, MLX, mentioned in Section 1.2, and based on these SCMs and null-flux track topology.

This configuration exhibits the same behavior in the evolution of lift and drag forces with respect to speed. Cai et al. in [11] show that at high speed, the lift and guidance forces stabilize. The drag force, which can be related to power loss, increases monotonically at low speed. Once the speed is sufficiently high, the drag force starts decreasing proportionally with $v^{-\frac{1}{2}}$ and stabilizes.

In the case of null-flux configuration, the 8-shaped coils can be mounted on the lateral walls as has been done for the MLX MAGLEV train (see Fig. 1.2). One advantage of this track configuration is the existence of a vertical equilibrium position when the magnetic field source is perfectly centered between the upper and lower loops of the 8-shaped coils of the track. In that position, there is no current in the coils, generating no losses [6]. However, if the magnets deviate from this centered position, a current is induced in the coils. According to Lenz's law, this induced eddy current generates a magnetic field opposing the changes in the source field [11]. This force is seen as a restoring force acting as a spring [53], ensuring stability.

Regarding lateral stiffness, in classical EDS systems using the null-flux configuration, the 8-shaped coils are positioned on the left and right sides of the vehicle (see Fig. 1.2b). When the vehicle is centered horizontally, the difference in forces from each side is null, no guidance forces are applied on the vehicle. However, when a lateral displacement occurs, the forces generated on the left and right sides of the vehicle become unequal, leading to different drag and lift forces across the train [11]. One way to overcome this issue, is the cross-connected structure. As depicted in Fig. 2.12, this structure improves the guidance of the system by connecting the left and right sides together. When the train is off-center, it generates guidance forces that tend to return it to the center of the track. These forces reach their minimum when the train is effectively back at the center.

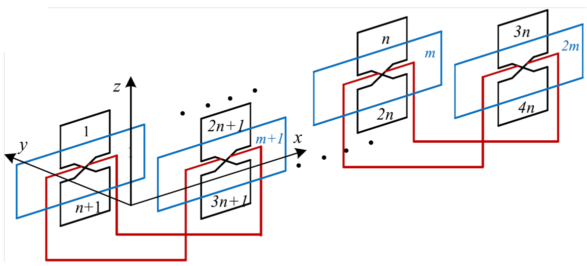

Figure 2.12: Schematic of the guidance and levitation systems on a cross-connected null-flux coils structure [11].

The configuration using SCMs offers excellent lateral stiffness but is very complex and expensive. The configuration using permanent magnets aims to mitigate these issues. However, when compared to other configurations, it has the lowest LWR, and although its LDR is high, it is not sufficient to compensate for the low LWR. This results in a relatively low lift with respect to the weight of the PMs [10]. Given this, the configuration could still be used, but it should be supplemented by other systems to achieve better performance and hence increasing the costs.

2.1.3 Continuous Tracks

Plate, Conductive sheet track

This track configuration is shown in Fig. 2.4a. It is a continuous type of track using sheets of non-ferromagnetic conductive materials, as mentioned in Section 2.1. The advantages of these tracks have already been covered: simplicity resulting in lower initial costs, reduced material requirements, and easier installation.

When compared to ladder or flat discrete coil configurations, these tracks exhibit higher lift and generally provide a relatively low LDR. Their simplicity also works to their advantage, as they offer an easier way to achieve high lift and great stability.

However, complex phenomena are generally not considered when assessing the performance of conductive sheet tracks. Similarly, discrete tracks modelling is highly simplified. For example, although the overall behavior of the lift and drag forces is similar to the one depicted in Fig. 2.7, the inherent electromagnetic interactions are much more complex. In the case of continuous plate tracks, the skin effect and diffusion angle, which will be explained in more detail in Chapter 3, have a significant impact on the electromagnetic interactions and performance of the track [6]. These factors are often overlooked, leading to potential significant inaccuracies in LDR and cost predictions.

When compared not only to the ladder track but to all configurations, continuous tracks have certain advantages, such as lower initial cost, as demonstrated by a high LWR, along with their simple form and installation process. However, their LDR is among the lowest of all track configurations as explained in Beauloye [10]. Additionally, they suffer from poor transverse stability [54], a common issue in EDS systems using flat tracks [6]. When the PMs above a single flat guideway are off-center, the induced currents generate a force that pushes the vehicle even further off-center. Resulting in high operational costs due to the need for additional systems for lateral stabilization and increased power losses.

Split-guideway

The split guideway track, similar to the conductive sheet track, utilizes non-ferromagnetic conductive materials such as aluminum or copper sheets, thereby retaining all the advantages of continuous plates. However, it features a unique design where the guideway is split into two sections (see Fig. 2.4b), which impacts its performance and electromagnetic characteristics.

The concept of the split guideway track has been extensively reviewed by Bird and Lipo in [12]. The authors linked the split-guideway to the use of Electrodynamic Wheels (EDW), as shown in Fig. 2.13, which generate lift, thrust, and guidance forces as the magnets rotate over the split sheets. They demonstrated that this type of guideway, in contrast to the conductive sheet configuration, offers good transverse stability. When the wheel is off-center, guidance forces are passively generated to return the vehicle to the center of the track.

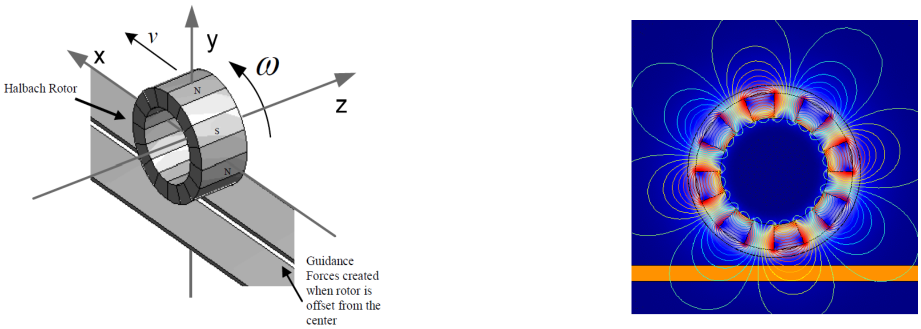

(a) (b)

Figure 2.13: EDW and Split-guideway a) EDW above split-guideway [12], b) Halbach array rotor (EDW) over flat guideway [13].

In conclusion, while this configuration has slightly lower lift and overall performance than the plate configuration, it allows for lower operational costs since it does not require additional lateral stability systems.

2.2 Conclusion and Research Objectives

In this chapter, we reviewed the advantages and disadvantages of existing EDS track topologies, laying the groundwork for the research presented in this thesis. Our goal in this research is to identify new topologies that can subsequently be considered and optimized in shape to determine the best design for specific applications. The final goal of this thesis is to create an efficient method for discovering new useful track topologies. Our focus is on flat tracks, starting from a continuous plate. The resulting topologies can be continuous or discrete, as the ladder track.

To effectively assess the performance of a track and optimize its shape and topology, it is essential to develop accurate models—both analytical or numerical. Several documents provide in-depth analyses and models for both discrete and continuous tracks. For instance, analytical models using equivalent electrical circuit models have been extensively developed for different discrete track topologies, such as the ladder track, as seen in the works by Beauloye and Dehez [6],[10], and in the work of Storset and Paden [9],[62], as well as the inductrack in the studies by Post and Ryutov [57], among other works.

Building upon these existing methodologies, this thesis develops a similar type of model for the conductive sheet track. The first step involves using equivalent electrical circuits, as demonstrated in previous research on ladder tracks. This approach is then refined until reaching a conductive plate model flexible enough to serve as the framework for a density-based topology optimization (see Chapter 6).

In summary, by leveraging an existing model—the ladder track model, developed in the next chapter—this study develops and validates a new analytical model while verifying the feasibility of using this model in TO. This final comprehensive model allows the potential access to new track configurations, and subsequently can also be used to refine the shapes to enhance their performances or the performances of already existing track topologies.

Chapter 3

Initial Model Development, Ladder Track Model and Validation

In this chapter, the initial concept that led to the development of the analytical model for the topology optimization and performance modeling of flat tracks in PM-EDS systems is presented. The first section covers the general methodology, including the assumptions and simplifications made. The mathematical development of this initial model is then discussed. Finally, the methodology and the initial model are validated using a finite element method (FEM) model developed in Comsol Multiphysics®.

3.1 Basic Modeling Concepts

The objective is to present the fundamental concept that leads to the development of an analytical model enabling the use of density-based TO on a conductive plate track.

For this conductive sheet model, a network of equivalent electrical circuits was employed to represent the physical electromagnetic domain. The domain was decomposed into elements via a mesh, as illustrated in Fig. 3.1. Each element in the mesh is represented by an equivalent circuit consisting of four lumped inductances (L_l, L_r, L_u, L_d), four resistances (R_l, R_r, R_u, R_d), and induced voltages (E_u, E_d) in the transverse direction, along the y-axis. The structure of this circuit closely resembles that shown in Fig. 3.1, providing a detailed schematic representation of the electromagnetic interactions within the system.

The values of the inductances and resistances are determined by the discretization of the region being studied and the dimensions of the cross-section considered for the discrete equivalent circuit branches. The resistance for each element can be expressed mathematically as follows:

$$R_l = R_r = \frac{\rho \Delta x/2}{w_{tc} \times w_{lc}}, \quad R_u = R_d = \frac{\rho \Delta y/2}{w_{tc} \times w_{lc}} \tag{3.1}$$

In this expression, ρ denotes the electrical resistivity of the material, $w_{tc} \times w_{lc}$ is the cross-sectional area of the conductive branches, taken as identical for the vertical and horizontal branches for the rest of the study, and Δx and Δy represent the discretization lengths along the x-axis and y-axis, respectively.

The induced voltages within the system are derived based on the relative motion between the magnetic field and the conductive material. This derivation takes into account the speed and geometry of the system as well as the mesh configuration.

This representation, which employs a network of equivalent electrical circuits, allows for precise modeling of the electromagnetic interactions within the system. It sets up a robust framework for the application of TO.

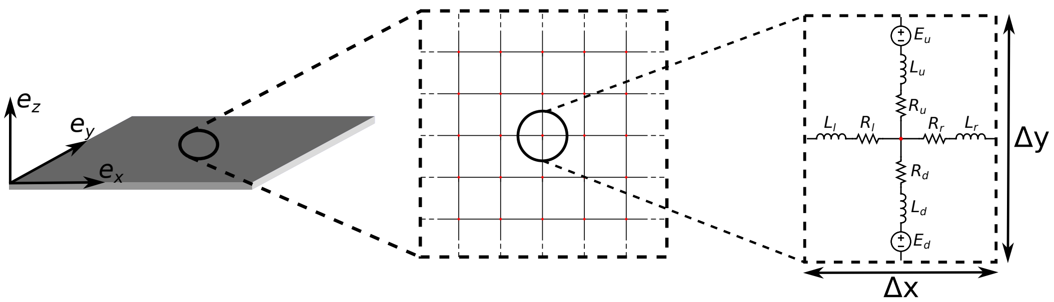

Figure 3.1: Mesh representation of the physical domain and its equivalent circuit elements.

3.1.1 Assumptions

Modeling a continuous track using equivalent circuit models necessitates assumptions and simplifications that might limit the model's ability to capture the complex electromagnetic interactions within the system accurately. One key assumption pertains to the distribution of the induced current in the conductors, which is considered uniform across the entire cross-section, locally induced currents being disregarded [10].

A significant effect neglected under this assumption is the skin effect. The skin effect describes how alternating currents and magnetic fields tend to be confined closer to the surface and to a smaller effective cross-sectional area within a conductor at high frequencies [6]. According to Wheeler [63], the penetration depth of the currents is dependent on the angular frequency of the alternating current or magnetic field (ω) and the properties of the conductive material, including its resistivity (ρ) and permeability (μ), and is defined as:

$$\delta_{skin} = \sqrt{\frac{2\rho}{\omega\mu}} \tag{3.2}$$

The angular frequency (ω) can be expressed as:

$$\omega = \frac{\pi v_x}{\tau_m} \tag{3.3}$$

where:

- v_x is the longitudinal velocity of the magnetic field.
- τ_m is the pole pitch of magnetic source field.

The Fig. 3.2 illustrates this effect for multiple values of v_x. It is evident that the penetration depth decreases as speed increases. Additionally, the electromagnetic field diffuses into the conductive material at an angle rather than perpendicularly to the surface. As speed increases, this diffusion angle also increases, thereby altering the current distribution in the discrete conductors considered.

To mitigate inaccuracies, thin plates are often studied, as larger cross-sections of the discrete branches would exacerbate the inaccuracies at higher speeds. The finite thickness of the conductive sheet is then accounted for only by adjusting the resistance values.

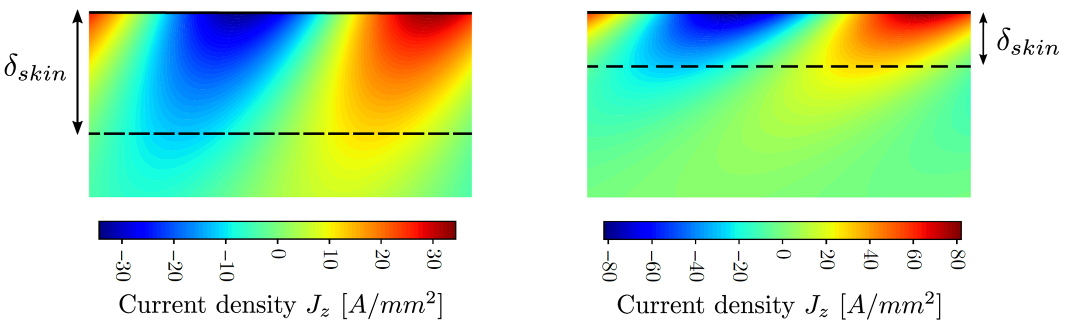

(a) (b)

Figure 3.2: Current Density Distribution in Conductive Plates Showing the Skin Effect and Diffusion Angle at varying speed. (a) at 10 m/s (b) at 50 m/s [6].

An approach to address these complexities involves using a three-dimensional (3D) modeling method by dividing the plate into infinitesimally thin layers, each decomposed into a mesh of equivalent electrical circuits, which are then electrically connected to one another vertically. This method allows for a more accurate representation of the skin effect and the angle of diffusion, as each layer accounts for varying current densities and magnetic field penetrations at different depths. However, implementing a full 3D model increases computational complexity. The relevance and potential benefits of such a 3D model for optimizing the topology of flat PM-EDS tracks will be discussed in Chapter 8.

Additional assumptions in the modeling process include the following [9],[10]:

- Considering the geometry as infinite along the x-axis [6], neglecting end effects.
- Assuming the magnetic field moves at a constant speed v_x in the x-axis direction.
- Considering a constant air gap, noted as t_{ag}, between the track and the magnetic field source.
- Assuming the magnetic field as periodic.

With these assumptions, the model enables the static analysis of electromagnetic interactions and, consequently, the computation of static forces for a given longitudinal speed v_x and a constant air gap value t_{ag}.

3.1.2 Simplifications Toward the Ladder Track Model

To develop the final model for the topology optimization of the flat track, it is essential to establish a strong foundation. Therefore, the process began with a simplified model.

Rather than immediately working with a full conductive sheet, an already developed topology, the ladder track, was initially considered. This topology has been previously modeled in previous works using equivalent electrical circuits [10],[9], providing a robust basis for the development of a more advanced model.

From the mesh representation of the physical domain shown in Fig. 3.1, the equivalent circuit for a ladder track can be derived. The Fig. 3.3 demonstrates how a row of the mesh can be seen as the equivalent circuit of a ladder track.

The Fig. 3.4 illustrates the ladder topology with a HPMA moving above the track at a speed of v_x and with an air gap t_{ag} between the track and the HPMA array. This figure depicts most of the geometric parameters of the PM-EDS system while Table 3.1 summarizes all its parameters.

3.1.3 Magnetic Field Source

In this study, a HPMA can be considered as the magnetic field source, as depicted in Fig. 3.4. This type of permanent magnet array produces a quasi-sinusoidal periodic magnetic field. The expression for the magnetic flux density generated by such array is given by Halbach in [64] and further developed

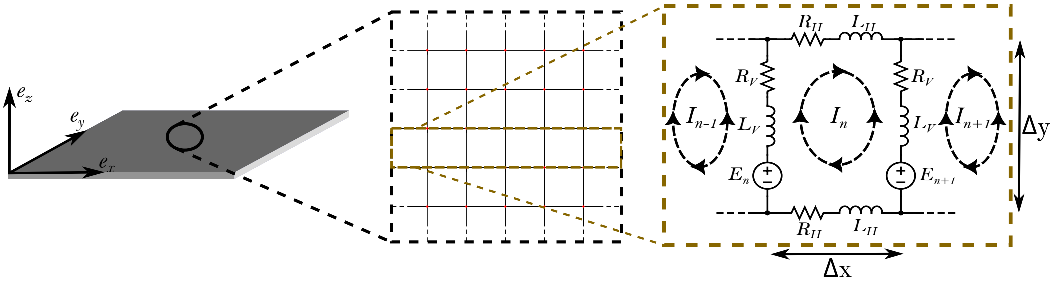

Figure 3.3: Transformation of a Mesh Representation to a Ladder Track Equivalent Circuit.

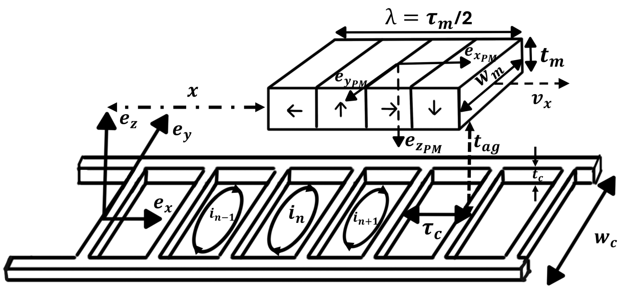

(a)

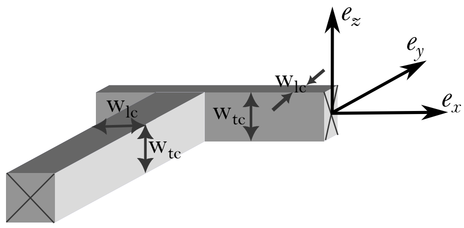

(b)

Figure 3.4: Geometric Representation of the Ladder Track Topology with Halbach Array. (a) Depiction of the ladder topology with a HPMA moving above the track (inspired by [9]). (b) Illustration of the cross-sectional view of the track.

by Storset and Paden in [9]. The authors describe the magnetic flux density $\mathbf{B}(x, z)$ the following way:

$$\mathbf{B}(x, z) = B_0 e^{-k\omega z} \sum_{v=0}^{\infty} (\hat{e}_x \sin(k\omega x) + \hat{e}_z \cos(k\omega x)) \tag{3.4}$$

where B_0 is the peak magnetic flux density, ω is the wave number, k is a harmonic number, x and z are spatial coordinates, and e^x and e^z are unit vectors in the x and z directions, respectively.

The peak magnetic flux density B_0 is given by:

$$B_0 = B_r \left(1 - e^{-k\omega t_m}\right) \frac{\sin(k\epsilon\pi/N)}{k\pi/N} \tag{3.5}$$

where B_r is the remanent magnetic flux density of the permanent magnet material, t_m is the thickness of the magnets, ϵ is the fractional slot opening, and N is the number of slots per wavelength.

The wave number ω and harmonic number k are defined as:

$$\omega = \frac{2\pi}{\lambda}, \quad k = 1 + vN \tag{3.6}$$

where λ is the wavelength of the magnetic field.

For the analytical models developed in this study, the ability to account for magnetic fields composed of numerous harmonics was considered. However, retaining only the first harmonic dominating the field [64] still provides a valid approximation of the total field generated, as mentioned by Storset and Paden in [9].

Therefore, for the validation of the analytical ladder model, as well as for the validation of subsequent models using FEM models, a simple sinusoidal magnetic field of the following form was used:

$$B_z(x, y) = A(t_{ag}) \cdot \sin\left(\frac{2\pi}{\lambda}\left(x + \frac{\tau_m}{2}\right)\right) \tag{3.7}$$

with A being the maximum amplitude value of the B-field, function of the air gap t_{ag}, and therefore the distance between the track and the PM array. This field is considered uniform along the y-axis.

To conclude, given the assumptions on the analytical model, the magnetic source field is considered periodic, infinitely long in along x-axis direction, and is taken wider than the track ($w_m > w_c$), where w_m is the width of the PM array and w_c is the width of the track. The edge effects are neglected, and the magnetic field is assumed to be independent of the transverse coordinate along the y-axis. Thus being uniform on the all width of the track.

Symbol	Quantity	Value
τ_m	Pole pitch of the PMs	0.2 m
w_m	Width of the PMs	0.4 m
t_m	Thickness of the PMs	0.05 m
t_{ag}	Air gap thickness	- mm
τ_c	Coil pitch	- m
w_c	Width of the track	0.4 m
t_c	Thickness of the track	- m
$w_{tc} \times w_{lc}$	Wire cross-section	- mm^2
$\sigma = \rho^{-1}$	Electrical conductivity	3.5×10^7 S/m
v_x	Translational speed	- m/s
Δx	Discretization along x-axis	- m
Δy	Deiscretization along y-axis	- m

Table 3.1: Electromagnetic and Structural Parameters of the System (adapted from [10]).

3.2 Analytical Model Development

In this section, the induced currents and forces in the ladder track are computed using the model depicted in Fig. 3.5.

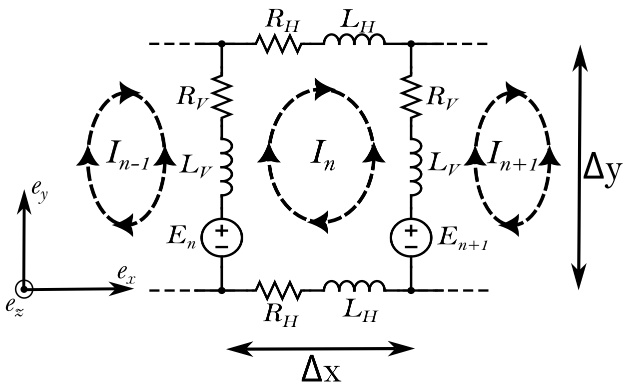

Figure 3.5: Ladder track equivalent circuit model.

3.2.1 Derivation of the Induced Current Formula

By applying Kirchhoff's Voltage Law (KVL) to the n-th loop, the following equation is obtained:

$$
\begin{aligned}
&2R_H I_n + R_V\left(2I_n - I_{n-1} - I_{n+1}\right) \\
&\quad + \sum_m L_{Vm}\frac{d}{dt}(I_{n+m} - I_{n-1+m}) \\
&\quad + \sum_m L_{Vm}\frac{d}{dt}(I_{n+m} - I_{n+1+m}) \\
&\quad + \sum_m 2L_{Hm}\frac{d}{dt}I_{n+m} \\
&= E_n - E_{n+1}
\end{aligned}
\tag{3.8}
$$

Here, L_{Vm} represents the mutual inductance between a transverse branch of the n-th loop and the corresponding transverse branch of the $(n+m)$-th loop. Similarly, L_{Hm} denotes the mutual inductance for longitudinal branches. L_{V0} and L_{H0} are the self-inductances of a transverse and a longitudinal branch of the n-th loop, respectively. The resistances of the transversal and longitudinal branches, R_V and R_H, are defined as:

$$
R_H = \frac{\rho \Delta x}{w_{tc} \times w_{lc}}, \quad R_V = \frac{\rho \Delta y}{w_{tc} \times w_{lc}} \tag{3.9}
$$

In this context, the transversal and longitudinal conductors are assumed to have the same cross-section. For the ladder model, the lengths of the longitudinal and transverse branches are taken as Δx and Δy, respectively. Specifically, for the specific case of the ladder track, the following holds: $\Delta x = \tau_c$, $\Delta y = w_c$.

Each conductor in the equivalent circuit corresponds to the fusion of two branches of two adjacent mesh elements—top and bottom for the transverse branches, and left and right for the longitudinal branches— a visual representation aiding understanding is shown in Fig. 3.6. The resistance values are dependent on the geometry of the mesh elements. In this initial ladder model, it is assumed that each mesh element has the same geometry, simplifying the expression of the resistance. However, the resistance values are refined later to allow for different resistivities for each mesh element, facilitating the use of a non-uniform mesh and building a framework for the TO.

In the vehicle's reference frame, the magnetic field remains constant, and the vehicle's speed (v_x) and the air gap (t_{ag}) are assumed constant as well. In discrete models such as the ladder track, the current patterns on the track in the vehicle's reference frame are time-dependent. To obtain a stationary image of the induced current in the moving reference frame, the track current can be sampled at specific times as mentioned by Storset and Paden in [9]. This specific time interval is dependent on the speed and the coil pitch, and is

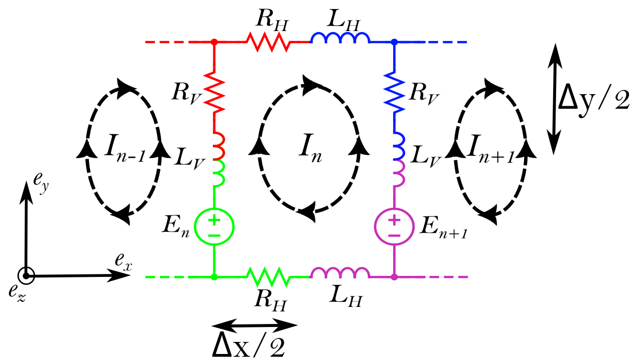

Figure 3.6: Ladder track equivalent circuit model with mesh element dimensions

given by $T_s = \frac{\tau_c}{v_x}$. To this time interval, called the time shift, corresponds an equivalent spatial shift, representing the displacement achieved during the time interval T_s. Consequently, the currents and induced voltages can be sampled and expressed as follows:

$$\text{Time shift: } I_{n+m}(t) = I_n(t - mT_s), \quad E_{n+m}(t) = E_n(t - mT_s) \tag{3.10}$$
$$\text{Space shift: } I_{n+m}(x) = I_n(x - m\tau_c), \quad E_{n+m}(x) = E_n(x - m\tau_c) \tag{3.11}$$

Providing a stationary image and model in the moving reference frame with constant speed and air gap. Therefore, the total time derivative is expressed as [8]:

$$\frac{d}{dt} = \frac{\partial x}{\partial t}\frac{\partial}{\partial x} = v_x \frac{\partial}{\partial x}. \tag{3.12}$$

Using Eq. 3.10, 3.11, and 3.12, the KVL can be rewritten as:

$$\begin{aligned} &2R_H I_n + R_V\left(2I_n - I_n(x+\tau_c) - I_n(x-\tau_c)\right) \\ &\quad + \sum_m L_{Vm} v_x \frac{\partial}{\partial x}\left(I_n(x - m\tau_c) - I_n(x-(m-1)\tau_c)\right) \\ &\quad + \sum_m L_{Vm} v_x \frac{\partial}{\partial x}\left(I_n(x - m\tau_c) - I_n(x-(m+1)\tau_c)\right) \\ &\quad + \sum_m 2L_{Hm} v_x \frac{\partial}{\partial x} I_n(x - m\tau_c) \\ &= E_n - E_n(x - m\tau_c) \end{aligned} \tag{3.13}$$

Fourier series can then be used to solve this first-order ODE [8]. For a magnetic field composed of N_h harmonics, the induced current and voltage can be written as Fourier series [10]:

$$I_n = \sum_k^{N_h} I_{nk} e^{j\omega_k x}, \quad E_n = \sum_k^{N_h} E_{nk} e^{j\omega_k x} \tag{3.14}$$

with $\omega_k = \frac{k\pi}{\tau_m}$ being the spatial frequency depending on the PM array's pole pitch.

By introducing the Fourier series, the KVL for each harmonic of the system can be expressed as:

$$\begin{aligned}
&2\left[R_H + j\omega_k v_x\left(L_{H0} + \sum_{m=1} L_{Hm}(e^{j\omega_k m\tau_c} + e^{-j\omega_k m\tau_c})\right)\right] I_{nk} \\
&+\left[R_V + j\omega_k v_x\left(L_{V0} + \sum_{m=1} L_{Vm}\left(e^{j\omega_k m\tau_c} + e^{-j\omega_k m\tau_c}\right)\right)\right] I_{nk}(1-e^{-j\omega_k\tau_c}) \\
&+\left[R_V + j\omega_k v_x\left(L_{V0} + \sum_{m=1} L_{Vm}\left(e^{j\omega_k m\tau_c} + e^{-j\omega_k m\tau_c}\right)\right)\right] I_{nk}(1-e^{j\omega_k\tau_c}) \\
&= E_{nk}(1-e^{j\omega_k\tau_c})
\end{aligned} \tag{3.15}$$

The equivalent inductances L_{Veq} and L_{Heq} are commonly used in discrete PM-EDS track modeling with periodic shapes and conditions [65]. They are defined as:

$$L_{Veq} \triangleq L_{V0} + 2\sum_{m=1} L_{Vm}\cos(m\omega_k\tau_c) \tag{3.16}$$

$$L_{Heq} \triangleq (L_{H0} + M_{H0}) + 2\sum_{m=1}(L_{Hm} + M_{Hm})\cos(m\omega_k\tau_c) \tag{3.17}$$

The term $2\cos(m\omega_k\tau_c)$ arises due to the symmetry of the system, where $L_{H-m} = L_{H+m}$ and $L_{V-m} = L_{V+m}$, and the shifts in the current loops leading to (similarly for L_{Hm}) :

$$L_{V-m}I_{nk}e^{(-m\omega_k\tau_c)} + L_{Vm}I_{nk}e^{(m\omega_k\tau_c)} = 2L_{Vm}I_{nk}\cos(m\omega_k\tau_c)$$

For the equivalent inductance L_{Heq}, the mutual inductance between the considered longitudinal conductor and with the longitudinal branches on the opposite side of the loops are also accounted for with the term M_{Hm}. A representative schematic, shown in Fig. 3.7, aids in understanding these equivalent inductances, and Section 3.3 delves more into an analysis of their behavior with changes in the geometry of the system.

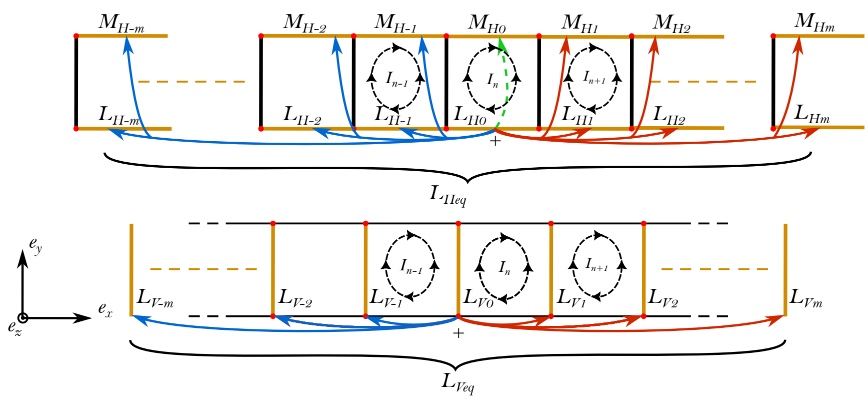

Figure 3.7: Equivalent Inductances in Ladder Track: symmetric Inductance Contributions

The final equation is thus simplified as:

$$2\left(R_H + R_V + j\omega_k v_x L_{Heq} + j\omega_k v_x L_{Veq} - (R_V + j\omega_k v_x L_{Veq})\cos(\omega_k \tau_c)\right) I_{nk} \\ = E_{nk}(1 - e^{j\omega_k \tau_c}) \tag{3.18}$$

The induced electromotive force (EMF) is derived from the fundamental principle of the Lorentz force law. It accounts for the velocity of the magnetic source and the magnetic field distribution along the conductor's length:

$$E_{nk} = \int_{-\frac{w_c}{2}}^{\frac{w_c}{2}} \mathbf{v} \times \mathbf{B}_{nk}\, dy \tag{3.19}$$

Every harmonic of the current I_{nk} can be obtained, allowing for the reconstruction of the total current in the m-th loop as:

$$I_m = \Re\left\{\sum_k I_{nk} e^{j\omega_k (x + m\tau_c)}\right\} \tag{3.20}$$

3.2.2 Derivation of the Static Forces

The drag and lift forces can be computed using various methods. In [8], Chen and Feng utilized the concepts of energy and magnetic co-energy. Here, the forces are computed using a local approach based on the Lorentz force equation:

$$d\mathbf{F} = I d\mathbf{l} \times \mathbf{B} \tag{3.21}$$

With this method, the magnetic flux density $\mathbf{B}$ is evaluated for each branch of the ladder. The drag force is directly related to the transverse branches of the track through the component B_z of the B-field, as discussed in Subsection 2.1.2. The lift force is associated with the longitudinal and transverse branches through the B_y and B_x components of the magnetic flux density, respectively.

Another method to compute these static forces involves using the intercepted flux passing through the loops of the ladder. In this approach, the lift and drag forces are expressed as:

$$F_{drag} = I_n \frac{d\Phi_n}{dx}, \quad F_{lift} = I_n \frac{d\Phi_n}{dz} \tag{3.22}$$

where Φ_n is the flux intercepted by a loop:

$$\Phi_n = \iint \mathbf{B} \cdot d\mathbf{s} = \int_{x-\frac{\Delta x}{2}}^{x+\frac{\Delta x}{2}} \int_{-\frac{\Delta y}{2}}^{\frac{\Delta y}{2}} B_z\, dx\, dy \tag{3.23}$$

This latter method is used in this thesis as it simplifies the implementation and requires only the z-component of the magnetic flux density.

3.3 Analysis of Equivalent Inductances Behavior

Understanding the behavior of the equivalent inductances L_{Veq} and L_{Heq} is crucial, as it provides insights into the number of mutual inductances that should be considered. The impact of a loop that is too far from the considered loop is negligible. Consequently, restricting the number of adjacent loops can reduce computation time without sacrificing accuracy. The expressions of the equivalent inductances, limited to a number N_m of mutual inductances, are defined as:

$$L_{Veq} \triangleq L_{V0} + 2\sum_{m=1}^{N_m} L_{Vm}\cos(m\omega_k\tau_c) \tag{3.24}$$

$$L_{Heq} \triangleq (L_{H0} + M_{H0}) + 2\sum_{m=1}^{N_m} (L_{Hm} + M_{Hm})\cos(m\omega_k\tau_c) \tag{3.25}$$

These inductances are influenced by the system's geometry, notably by the coil-pitch τ_c and the magnetic pole pitch τ_m through $\omega_k = \frac{k\pi}{\tau_m}$.

In Fig. 3.8, the evolution of L_{Veq} with respect to the number of adjacent loops or equivalently mutual inductances considered is shown. The behavior of L_{Heq} is analogous.

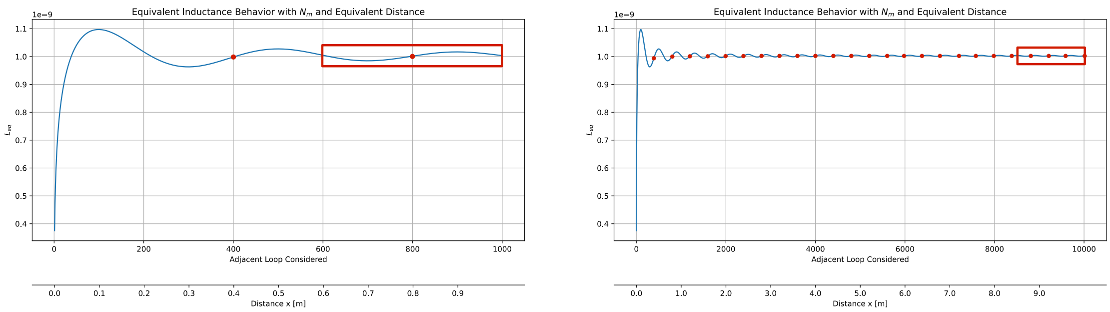

(a) (b)

Figure 3.8: Equivalent Inductance Behavior with N_m and Equivalent Distance. (a) shows the behavior for $N_m = 1000$, while (b) illustrates the behavior for $N_m = 10000$ adjacent loops considered.

Fig. 3.8 demonstrates that for a large N_m, the mean value of the last evaluations converges as it correspond to a larger distance. Given this behavior, the mean of the last evaluations is always taken as the final value for these equivalent inductances. These last evaluations are indicated with a red box in the figure.

By changing the coil-pitch τ_c and hence Δx in the ladder case, the frequency of the oscillations changes. With a quicker convergence in the case of a larger value of τ_c since larger distance are reached for a smaller N_m or a more time-consuming convergence in the case of a smaller value since a larger N_m is needed to reach a large enough distance. In Fig. 3.9, both cases are shown for smaller $\tau_c = 1$ mm and larger $\tau_c = 5$ mm. Once again, this behavior is expected because, for the same number of mutual inductances considered, a larger τ_c means that the distance between the n-th loop and the $(n+m)$-th loop is significantly greater. Therefore, limiting the number of adjacent loops considered still reaches distances large enough to make the equivalent inductance converge.

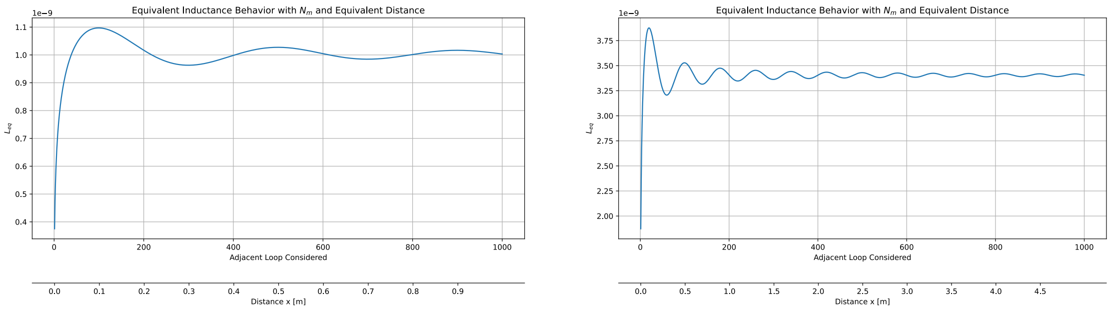

(a) $\tau_c = 1$ mm (b) $\tau_c = 5$ mm

Figure 3.9: Equivalent Inductance Behavior with N_m and Equivalent Distance for Different τ_c Values. (a) Convergence for smaller $\tau_c = 1$ mm. (b) Convergence for larger $\tau_c = 5$ mm.

To obtain the final value of the equivalent inductances, the mean value of the last iterations can be taken as mentioned earlier. Alternatively, to further reduce N_m, another method involves selecting a point corresponding to the first point of each period of oscillation. These points are highlighted in red in Fig. 3.8 and correspond to an exact number N_m given by:

$$N_m = p\frac{\tau_m}{\tau_c}, \quad p \in \mathbb{Z}, \quad p = 0, 1, \ldots, P \tag{3.26}$$

However, this method is less convenient as the number N_m needs to be adapted for each discretization value.

A value of $N_m = 10000$ is used for the ladder track as it ensures the convergence of the equivalent inductances for very small discretizations and is not excessively time-consuming. Increasing beyond this value of N_m does not justify the additional computing time needed. This value allows convergence for a discretization of $\Delta x = 0.1$ mm, larger than what we will be considering.

Appendix A provides a concise analysis, validation, and discussion of the formulas employed in this study for calculating mutual inductance, which subsequently form the basis for determining the equivalent inductances values.

3.4 Validation of the Ladder Track Model

To validate the ladder track model, a 2D FEM model was constructed using *Comsol Multiphysics®*. A visual representation of this model is depicted in Fig. 3.10.

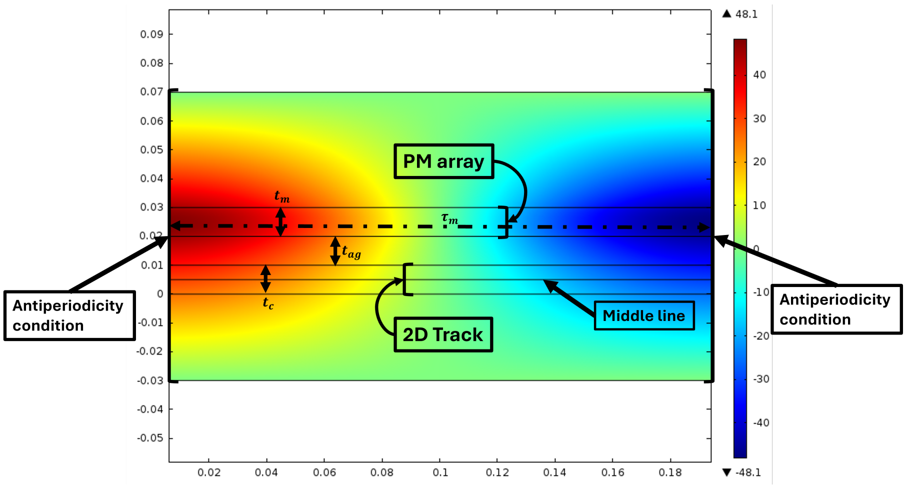

Figure 3.10: 2D FEM model of the ladder track created in *Comsol Multiphysics®*.

Given the periodicity of the system, the analysis was confined to half a period of the PM array, τ_m, imposing a condition of anti-periodicity on the model's boundaries. In the FEM model, a depth of 1 m was considered, which corresponds to setting $w_c = 1$ m in the analytical model. The initial parameter values used for PM-EDS are detailed in Table 3.2.

Symbol	Quantity	Value
τ_m	Pole pitch of the PMs	0.2 m
w_m	Width of the PMs	1 m
t_m	Thickness of the PMs	0.05 m
t_{ag}	Air gap thickness	5 mm
τ_c	Coil pitch	1 mm
w_c	Width of the track	1 m
t_c	Thickness of the track	5 mm
$w_{tc} \times w_{lc}$	Wire cross-section	5 mm^2
$\sigma = \rho^{-1}$	Electrical conductivity	3.5×10^7 S/m
v_x	Translational speed	1.15 m/s
Δx	Discretization along x-axis	τ_c m
Δy	Discretization along y-axis	w_c m

Table 3.2: Electromagnetic and Structural Parameters of the Ladder Model (adapted from [10]).

The geometric parameters in the analytical model were chosen to mimic a slitted plate (see Fig. 4.1a) with infinitesimally thin slits, more closely approximating the behavior of the 2D FEM plate model.

The z-component of the magnetic flux density used in this validation is chosen as:

$$A = 47.18e^{(-14.70t_{ag})} - 2.91 \tag{3.27}$$

$$B_z = A \sin\left(\frac{\pi}{\tau_m}\left(x + \frac{\tau_m}{2}\right)\right) \tag{3.28}$$

The amplitude function, A, which is a function of t_{ag} or the position of the PM array along the z-axis, is obtained by fitting the maximum value of the amplitude of B_z in the FEM model for different values of t_{ag}. This fitting process is illustrated in Fig. 3.11b.

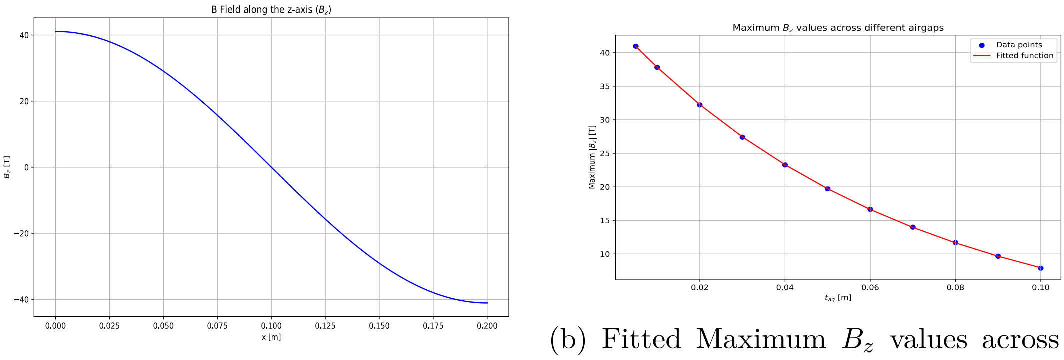

(a) B Field along the z-axis (B_z)

(b) Fitted Maximum B_z values across different air gaps

Figure 3.11: (a) Magnetic flux density B_z along the z-axis and (b) fitting of maximum B_z values for different air gaps.

The validation of the ladder model was conducted by varying several parameters, such as the speed v_x, the air gap t_{ag}, the discretization $\Delta x = \tau_c$ in the case of the ladder model, and the thickness of the conductors t_c. This validation process involved comparing local variables, the induced currents, and global variables, the drag and lift forces.

3.4.1 Validation of Analytical Model Through Current Densities and Forces Comparisons

The validation of the model begins with an analysis of the impact of varying v_x, as depicted in Fig. 3.12.

The study was limited to a velocity of 20 m/s. We can predict that, as the speed increases, the penetration depth δ_{skin}, mentioned in Section 3.1.1, will decrease, and the angle of diffusion will increase, leading to a more significant deviation between the analytical model and the 2D FEM reference model. Additionally, simulating high-velocity systems with periodic or anti-periodic conditions in FEM models like the one used here presents several challenges

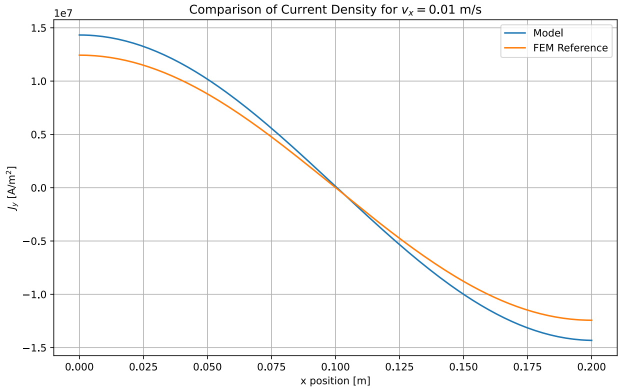

(a) Comparison of current density in the transverse conductors J_y at $v_x = 0.01$ m/s

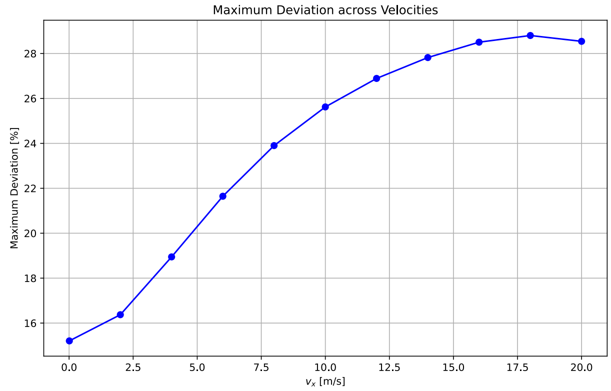

(b) Maximum deviation between model and reference across velocities

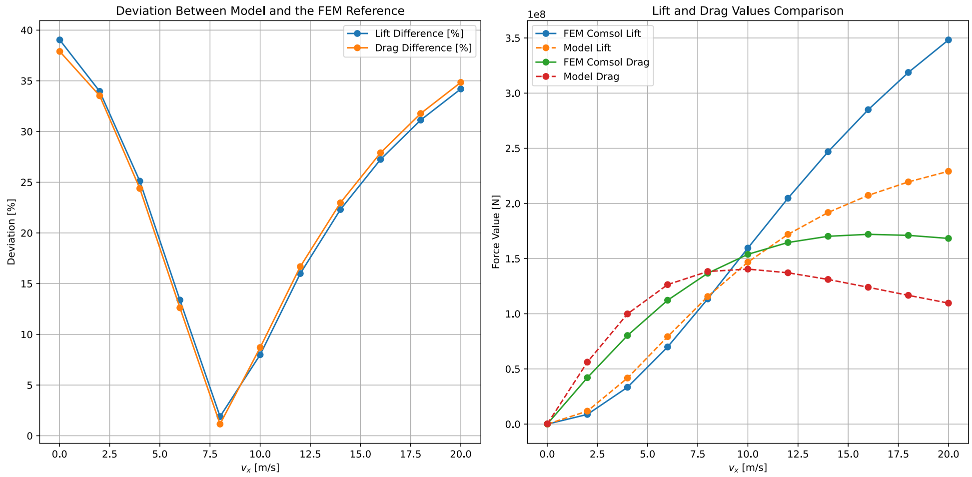

(c) Lift and drag comparison for varying v_x

Figure 3.12: Validation of model with varying velocity v_x. a) and b) current analysis. c) force analysis.

that significantly affect computation time and feasibility.

The current density distribution in Fig. 3.12a aligns with the FEM reference model. The lift and drag forces demonstrate that while the model accurately predicts the trend of increasing forces with velocity, their magnitude is sensitive to velocity changes. This sensitivity can be attributed to the skin effect and angle of diffusion at high speed, as mentioned above. The current density distribution in Fig. 3.12a-b shows significant deviation between the model and FEM reference, even at low speed ($v_x = 0.01$ m/s). The model also tends to overestimate the peak values of J_y. This discrepancy is consistently observed at both positive and negative maxima of the current density.

In Fig. 3.12c, the percentage of difference remains relatively high at low velocities, decreases around a mid-range speed of approximately 7.5 m/s, and then increases again at higher speeds. This suggests that the model has difficulty to accurately capture the behavior at low and high speeds, performing unexpectedly better in the mid-range velocities.

A hypothetical explanation for these discrepancies could be the potential inaccuracies in the data used for this final test. These inaccuracies might stem from measurement errors or assumptions during data collection. While efforts were made to ensure data reliability, these factors may have influenced the results. Another critical consideration is that the chosen FEM reference model in COMSOL, which simulates a 2D plate, might not have been the most appropriate for this study. Employing a 3D FEM model that accurately represents the ladder track could potentially yield significantly better results in all the tests conducted.

Next, v_x is kept constant at its initial value (see Table 3.2) while varying t_{ag}. The results are shown in Fig. 3.13.

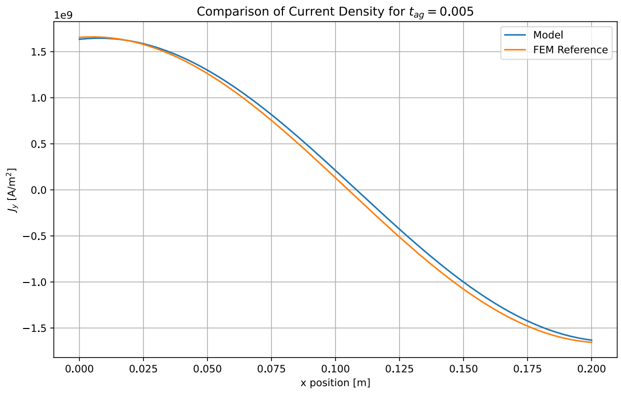

(a) Comparison of current density in the transverse conductors J_y for $t_{ag} = 0.005$ m

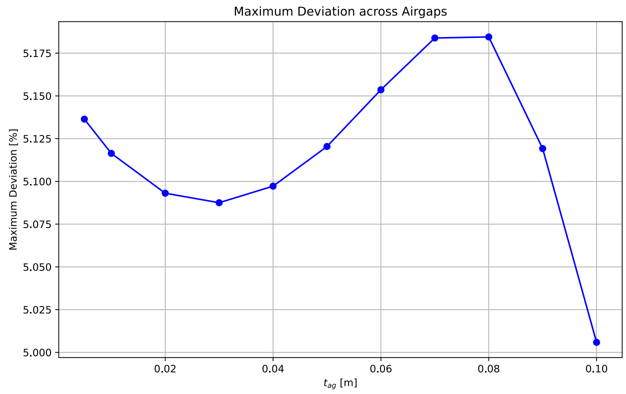

(b) Maximum deviation between model and reference across air gaps

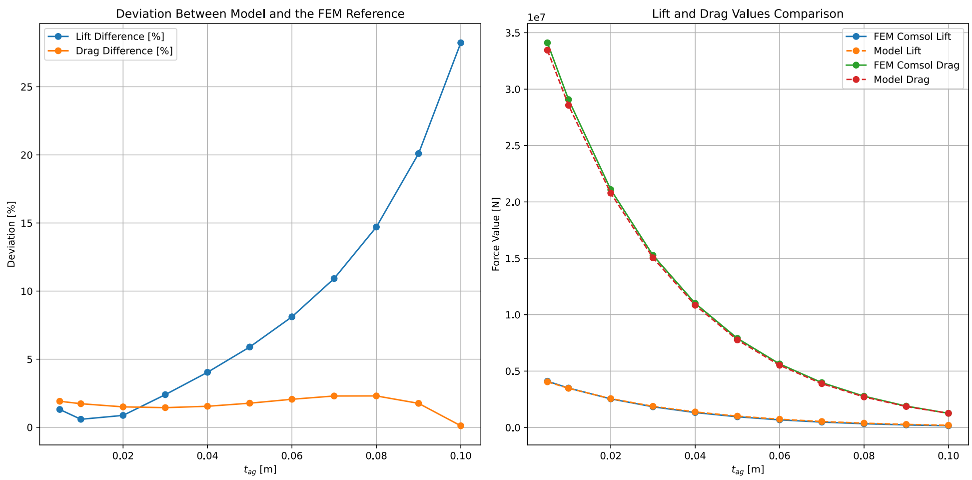

(c) Lift and drag comparison for varying air gap t_{ag}

Figure 3.13: Validation of model with varying air gap t_{ag}. a) and b) current analysis. c) force analysis.

Fig. 3.13a-b shows good alignment with the FEM reference model. The maximum deviation difference across air gaps for J_y and the drag force in c) remains relatively stable and small regardless of the air gap value. However, the lift force exhibits a different behavior, with the percentage difference increasing significantly as the air gap increases. A potential explanation is the following, as t_{ag} increases, the magnetic field strength decreases in the thickness of the track, reducing the coupling and amplifying the sensitivity of the lift. The lift force, derived from the derivative of the flux with respect to the z-axis, is more susceptible to variations in the current distribution and flux density in the thickness of the track. Therefore, any shifts or errors in current due to air gap changes have a more pronounced impact on lift than on drag.

Fig. 3.13c shows that small variations in the air gap lead to large relative changes in the lift force. At a speed of $v_x = 1.15$ m/s, the lift is nearly 10 times smaller than the drag. When the lift is significantly smaller than the drag, any absolute variation in lift will appear as a larger relative percentage deviation with respect to the FEM model, making these variations more noticeable in comparison to drag. Increasing the velocity could therefore enhance the results for lift by potentially increasing its magnitude, thereby making changes more apparent and less sensitive to small fluctuations or noise.

The following test concerned the impact of the thickness of the ladder track on the validity of the model. The results are shown in Fig. 3.14. Knowing that the model does not account for the skin effect, the current density is assumed to be uniform in the conductor's cross-section, which is not accurate for conductors with $t_c > \delta_{skin}$. With, in this specific case, $\delta_{skin} \approx 5$ mm.

The results for the thickness test exhibit a similar conclusion to the air gap test. The drag force remains relatively stable across varying thicknesses. However, since the thickness of the plate is already equal to the penetration depth, increasing the thickness directly results in errors in the lift force and current density. This behavior is consistent with the analysis of the air gap test, where the lift force is more sensitive to parameter.

The last test examines the impact of the discretization Δx value on the model's accuracy. The results are depicted in Fig. 3.15. Given the nature of the discretization validation, only the global variable (force) was considered for validation. Locally changing the discretization and comparing it with the current in the reference model does not provide meaningful insights. The local current distribution is significantly influenced by the discretization size, leading to discrepancies that are not reflective of the model's overall accuracy. Therefore, focusing on the global variable ensures a more accurate and relevant validation of the model's performance.

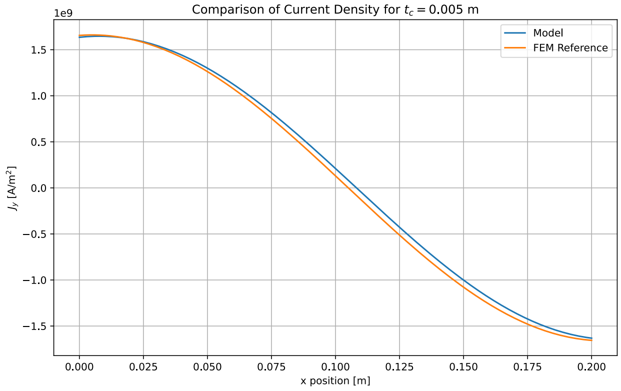

(a) Comparison of current density in the transverse conductors J_y for $t_c = 0.005$ m

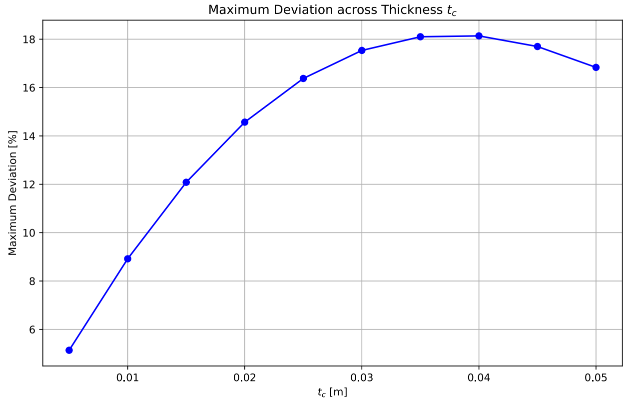

(b) Maximum deviation between model and reference across thicknesses

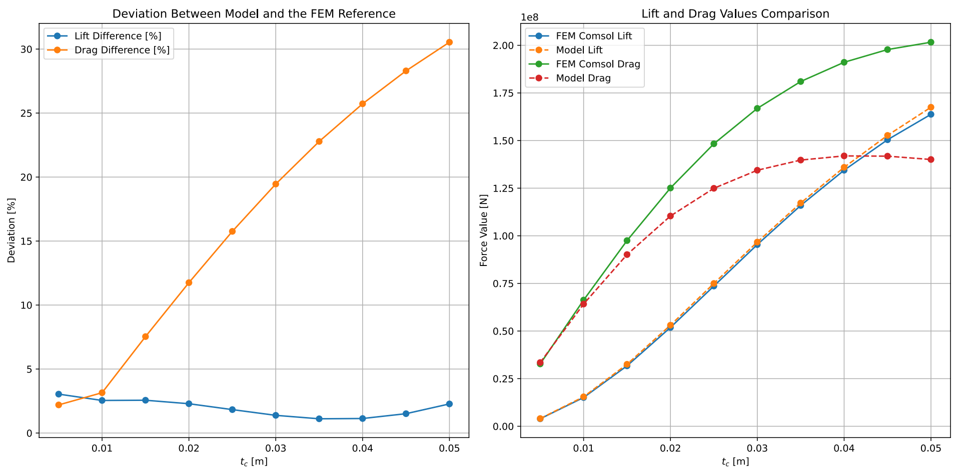

(c) Lift and drag comparison for varying thickness t_c

Figure 3.14: Validation of model with varying thickness t_c. a) and b) current validation. c) force validation.

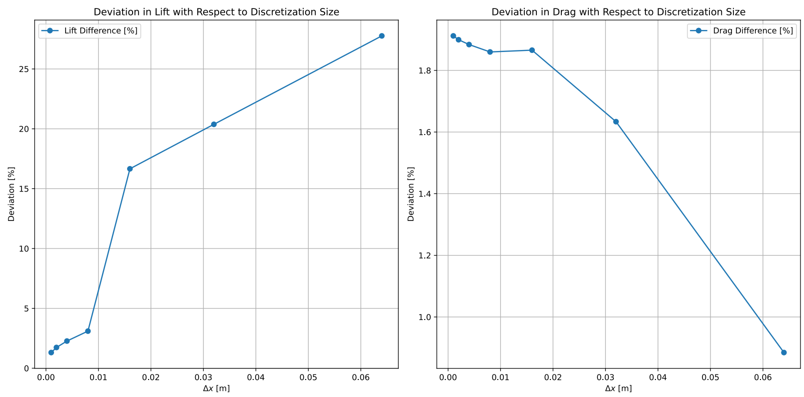

Figure 3.15: Validation of Lift and Drag Forces with Respect to Δx

The results of the discretization test are shown in Fig. 3.15. The lift force demonstrates a significant increase in percentage difference with larger Δx

values. This behavior is consistent with previous findings, where the lift force is more sensitive to variations in parameters. In contrast, the drag force percentage difference remains relatively stable and low, indicating a lower sensitivity to discretization changes for this global variable on the entire portion of track considered.

In summary, the validation tests reveal that the simplified plate model exhibits varying degrees of accuracy across different parameters. The model struggles to accurately predict current density and forces at both low and high velocities, with the skin effect and diffusion angle contributing to discrepancies at higher speeds. The lift force, in particular, shows greater sensitivity to changes in parameters like air gap and thickness compared to the drag force. Additionally, the choice of a slitted plate FEM model or a 3D ladder track FEM model, as opposed to a 2D plate model, may have introduced additional complexity but could potentially offer higher accuracy in the comparison between the analytical and FEM models. Nonetheless, the model provides a reliable foundation for further refinement and application in more complex scenarios.

A more thorough analysis using a 3D ladder track model in FEM, coupled with a higher initial velocity in the tests, could potentially yield significantly improved results in terms of deviation with respect to the reference. It is also important to note that this model has already been compared against a previously validated ladder track analytical model, yielding results that were very close. This comparison further suggests that the discrepancies observed in the current validation might stem from the choice of the reference model, reinforcing the potential benefits of revisiting the FEM model selection.

3.5 Conclusion on the Initial Model: Ladder Track

In this section, the ladder track model was developed and validated using a 2D FEM reference model. This model serves as a strong foundation for the plate models that will be explored in subsequent chapters. Mathematical tools such as equivalent inductances were introduced, which will facilitate the development and understanding of the more advanced plate track model.

Chapter 4

Simplified Plate Model

In this chapter, the development of the simplified plate track model is presented. The process begins with an explanation of how the ladder model aids in constructing and understanding the discrete simplified plate model. Following this, the analytical model is developed. The chapter concludes with a validation similar to the one done for the ladder model, this time using a 3D FEM plate model built on Comsol Multiphysics®.

4.1 From Ladder Track Model to Simplified Plate Model

The first model developed, the ladder model, does not allow for a complete conductive sheet modeling. The closest approach to a plate is achieved by choosing geometry parameters that lead to a slitted plate (see Fig. 4.1a).

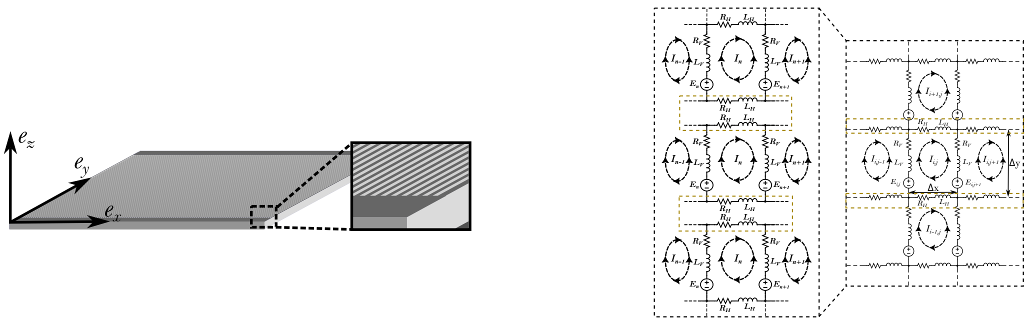

(a) Slitted plate model derived from ladder track geometry.

(b) Transition from the ladder model to the simplified plate model.

Figure 4.1: (a) Slitted plate representation and (b) transition from ladder model to first plate model.

However, the ladder model provides a good starting point. It introduces the necessary assumptions for discrete modeling of the plate track and provides mathematical tools useful for developing the more complex conductive sheets models in this chapter and the next.

The first simplified plate model developed in this chapter can be seen as taking multiple ladder track equivalent circuits and connecting them electrically in the transverse direction along the y-axis. Fig. 4.1 shows a simplified representation of this idea, while Fig. 4.2 illustrates the derivation of the equivalent circuit for the simplified plate model from the meshed domain.

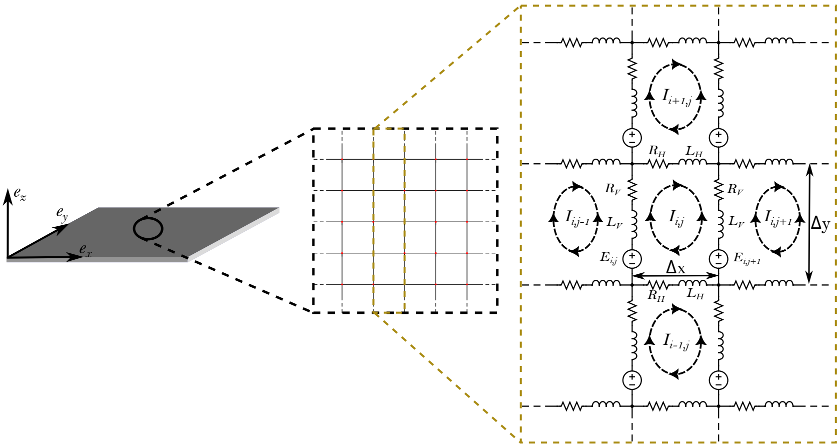

Figure 4.2: Derivation of the equivalent circuit for the simplified plate model from the meshed domain.

This simplified plate model can be developed using the same mathematical tools and methods as the ladder track model presented in Chapter 3.

4.2 Analytical Model Development

The equivalent circuit of the first simplified plate model is depicted in Fig. 4.3. This analytical model focuses on a transversal slice of the discrete mesh. The current loops are represented with two indices: one along the x-axis (i), indicating the row number, and one along the y-axis (j), indicating the column number of the current loops.

4.2.1 Derivation of the Induced Current Formula

Here, we show the analytical development for only one harmonic knowing it is the same for each harmonic of the system. Then, as for the ladder track model, the induced currents can, for each loop, be computed using Eq. 3.20.

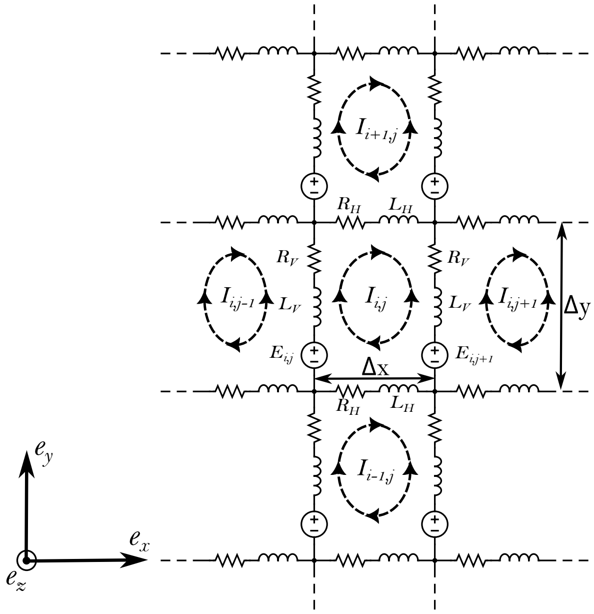

Figure 4.3: Equivalent circuit of the simplified plate model.

By applying the KVL to the center loop $I_{i,j}$, the following equation is obtained:

$$
\begin{aligned}
& R_H\left(2I_{i,j} - I_{i+1,j} - I_{i-1,j}\right) + R_V\left(2I_{i,j} - I_{i,j-1} - I_{i,j+1}\right) \\
& \quad + \sum_p \sum_m L_{Vp,m} \frac{d}{dt}(I_{i+p,j+m} - I_{i+p,j-1+m}) \\
& \quad + \sum_p \sum_m L_{Vp,m} \frac{d}{dt}(I_{i+p,j+m} - I_{i+p,j+1+m}) \\
& \quad + \sum_p \sum_m L_{Hp,m} \frac{d}{dt}(I_{i+p,j+m} - I_{i+1+p,j+m}) \\
& \quad + \sum_p \sum_m L_{Hp,m} \frac{d}{dt}(I_{i+p,j+m} - I_{i-1+p,j+m}) \\
& = E_{i,j} - E_{i,j+1}
\end{aligned}
\tag{4.1}
$$

where:

- $L_{Vp,m}$ denotes the mutual inductance between a transverse branch of loop $I_{i,j}$ and the corresponding transverse branch of the $I_{i+p,j+m}$ loop.
- $L_{Hp,m}$ denotes the mutual inductance for the longitudinal branches.
- $L_{V0,0}$ and $L_{H0,0}$ are the self-inductances of a transverse and a longitudinal branch of the $I_{i,j}$ loop, respectively.
- R_V and R_H are defined in Eq. 3.9.

As with the ladder model, a uniform meshing is generally considered, with transversal and longitudinal conductors having the same cross-section and sizes

Δx and Δy. However, local changes in meshing sizes can be implemented. The longitudinal discretization size is set equal to the coil pitch, $\Delta x = \tau_c$, as in the ladder track. The transverse discretization size, Δy, dictates the number of rows in the mesh and, consequently, the number of unknowns in the system. In the ladder track, there was only one unknown loop current, with the currents on the left and right being shifted versions of the computed current. Now, there are $N = \frac{w_c}{\Delta y}$ unknown currents, corresponding to the number of rows (loops) in the transverse slice of mesh considered.

Following the same development used for the ladder model, the Fourier series and phase shift principles (Eq. 3.10, 3.11) are applied, resulting in the following final equation for each current loop in the transverse slice of mesh:

$$\begin{aligned}
&2\left(R_V + R_H + j\omega_k v_x L_{Veq0} + j\omega_k v_x L_{Heq0} - \left(R_V + j\omega_k v_x L_{Veq0}\right)\cos(\omega_k \tau_c)\right) I_{i,j} \\
&\quad + 2j\omega_k v_x \sum_{p\neq 0}(L_{Heqp} + L_{Veqp}(1-\cos(\omega_k\tau_c)))I_{i+p,j} \\
&\quad - \left(R_H + j\omega_k v_x L_{Heq0}\right) I_{i+1,j} - j\omega_k v_x \sum_{p\neq 0} L_{Heqp} I_{i+1+p,j} \\
&\quad - \left(R_H + j\omega_k v_x L_{Heq0}\right) I_{i-1,j} - j\omega_k v_x \sum_{p\neq 0} L_{Heqp} I_{i-1+p,j} \\
&= E_{i,j}\left(1 - e^{j\omega_k \tau_c}\right)
\end{aligned} \tag{4.2}$$

In Eq. 4.2, equivalent inductances are used. They are defined as:

$$L_{Heq0} \triangleq L_{H0,0} + 2\sum_{m=1}^{N_m} L_{H0,m}\cos\left(m\omega_k\tau_c\right) \tag{4.3}$$

$$L_{Heqp} \triangleq L_{Hp,0} + 2\sum_{m=1}^{N_m} L_{Hp,m}\cos\left(m\omega_k\tau_c\right) \tag{4.4}$$

$$L_{Veq0} \triangleq L_{V0,0} + 2\sum_{m=1}^{N_m} L_{V0,m}\cos\left(m\omega_k\tau_c\right) \tag{4.5}$$

$$L_{Veqp} \triangleq L_{Vp,0} + 2\sum_{m=1}^{N_m} L_{Vp,m}\cos\left(m\omega_k\tau_c\right) \tag{4.6}$$

These equivalent inductances emerge from the same principles as those developed in the ladder track model. The primary difference here is the need to account for the influence of rows above and below the loop $I_{i,j}$. Equations 4.3 and 4.5 account for the influence of the loops located on the left and right of $I_{i,j}$ on the behavior of the this specific loop $I_{i,j}$. Equations 4.4 and 4.6 represent the mutual inductance based impact of the loops in the row $(i+p)$ on loop $I_{i,j}$. The Fig. 4.4 simplifies the understanding of these terms with a more visual representation.

These newly defined equivalent inductances exhibit similar behavior to the equivalent inductances analyzed in Section 3.3. However, for a large number p, the amplitude of the equivalent inductances decreases rapidly as shown in Fig.

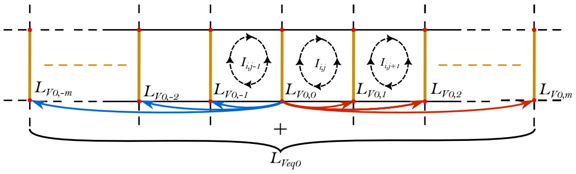

(a) Equivalent Inductance L_{Veq0}

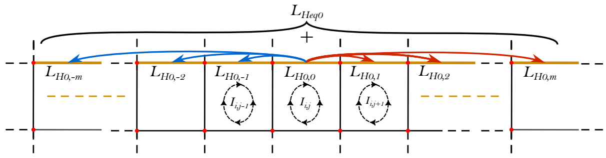

(b) Equivalent Inductance L_{Heq0}

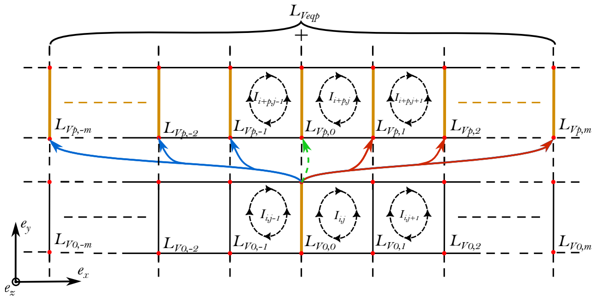

(c) Equivalent Inductance L_{Veqp}

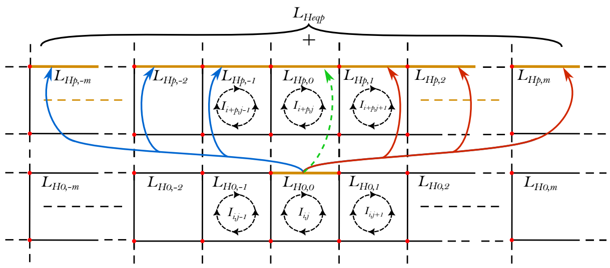

(d) Equivalent Inductance L_{Heqp}

Figure 4.4: Equivalent inductances for the simplified plate model.

4.5. This implies that the impact of the loops of rows in the mesh far from row i have a limited effect on the currents in row i itself. Consequently, it the value of p can be limited to a chosen number, denoted as p_{max}, depending on the discretization size Δy. A smaller discretization size along the y-axis, Δy, implies a larger number of rows in the mesh and also a larger p_{max}, as there are more rows to reach the same distance where the impact on row i becomes negligible.

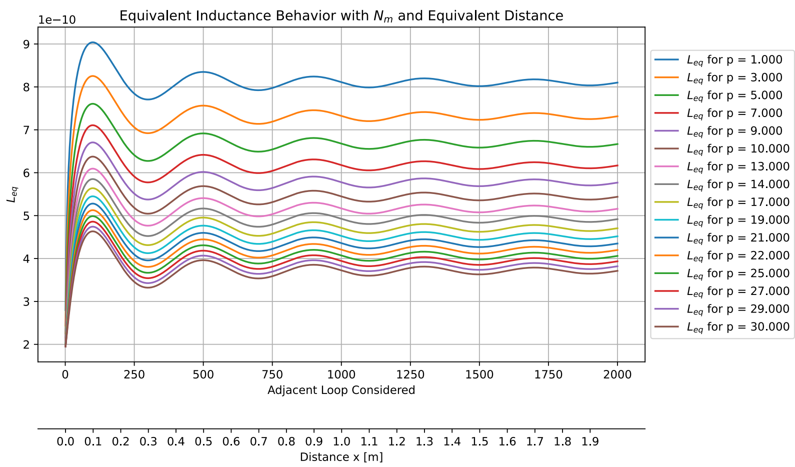

Figure 4.5: Behavior of equivalent inductances with respect to τ_c for the simplified plate model.

In the context of the plate model, the computation of induced voltages follows the same fundamental principles as employed in the ladder model. The key difference lies in the dimensions of the transverse branches over which the integration occurs. Unlike the ladder model, where the transverse branches span the entire width of the plate w_c, the transverse branches in the plate model have a length of Δy. Additionally, the y-position of each row is determined by the row index i and the distance between rows, Δy. The induced voltage for each loop can thus be expressed as:

$$E_{i,j} = \int_{i\Delta y}^{(i+1)\Delta y} \mathbf{v} \times \mathbf{B} \; dy \tag{4.7}$$

Here, the integration limits have been adjusted from $i\Delta y$ to $(i+1)\Delta y$, to reflect the length of the transverse branches.

A system of N equations, one for each current loop in the transverse slice, is thereby established. To solve the system of equations, it is represented in matrix form $AI = B$. Recognizing that the model focuses on a transverse slice of the mesh, and knowing that the currents and induced voltages on the left and right of this slice are merely shifted versions, the notation of the linear system can be simplified by removing the second index j from the currents and induced voltages expressions, i.e., $I_{i,j} \to I_i$ and $E_{i,j} \to E_i$.

- **Matrix** A: This matrix, of size $N \times N$, contains the resistive and inductive components of the system.
- **Vector** I: A vector of size N, representing the unknown currents I_i.
- **Vector** B: A vector of size N, representing the induced voltages E_i.

The matrix A is constructed in the following way:

- *Diagonal Elements*: Represent resistances of the loop and the self-inductances:

$$A_{i,i} = 2\left(R_V + R_H + j\omega_k v_x (L_{Veq0} + L_{Heq0}) - (R_V + j\omega_k v_x L_{Veq0})\cos(\omega_k \tau_c)\right)$$

- *Off-Diagonal Elements*: Represent the impact of upper and lower loops on $I_{i,j}$:

$$A_{i,i+1} = A_{i,i-1} = -\left(R_H + j\omega_k v_x L_{Heq0}\right)$$

- *Additional Terms related to Mutual Inductances*:

$$A_{i,i+p} = 2j\omega_k v_x \left(L_{Heqp} + L_{Veqp}(1 - \cos(\omega_k \tau_c))\right) \quad \text{for } p \in [-p_{max}, p_{max}]$$

$$A_{i,i+1+p} = A_{i,i-1+p} = -j\omega_k v_x M_{Heqp} \quad \text{for } p \in [-p_{max}, p_{max}]$$

Vector I:

$$I = \begin{bmatrix} I_0 \\ I_1 \\ \vdots \\ I_N \end{bmatrix}$$

Vector B:

$$B = \begin{bmatrix} E_1(1 - e^{j\omega_k \tau_c}) \\ E_2(1 - e^{j\omega_k \tau_c}) \\ \vdots \\ E_N(1 - e^{j\omega_k \tau_c}) \end{bmatrix}$$

System Representation:

$$AI = B$$

This approach transforms KVL equations into a solvable linear algebraic system. Solving this matrix equation provides the currents in each loop of the transverse slice of the mesh.

4.2.2 Derivation of the Static Forces

The F_{drag} and F_{lift} forces can be computed using the principles of the Lorentz force law, similar to the approach applied in the ladder model. The primary distinction in the simplified plate model lies in the integration limits.

Using the Lorentz force equation, the force can be calculated by evaluating the magnetic flux density $\mathbf{B}$ on each branch of the discrete plate:

$$d\mathbf{F} = I d\mathbf{l} \times \mathbf{B} \tag{4.8}$$

In this context, the drag force is associated with the transverse branches through B_z, while the lift force is related to both the longitudinal and transverse branches through the B_y and B_x components of the magnetic flux density, respectively.

An alternative method involves computing these static forces using the intercepted flux passing through the discrete loops of the plate. This method simplifies the expression of lift and drag forces and is the preferred approach for this implementation:

$$F_{\text{drag}} = I_{i,j} \frac{d\Phi_{i,j}}{dx}, \quad F_{\text{lift}} = I_{i,j} \frac{d\Phi_{i,j}}{dz} \tag{4.9}$$

The flux $\Phi_{i,j}$ intercepted by a loop can be expressed as:

$$\Phi_{i,j} = \iint \mathbf{B} \cdot d\mathbf{s} = \int_{x-\frac{\Delta x}{2}}^{x+\frac{\Delta x}{2}} \int_{i\Delta y}^{(i+1)\Delta y} B_z \, dx \, dy \tag{4.10}$$

In this context, the integration limits are adjusted from $x - \frac{\Delta x}{2}$ to $x + \frac{\Delta x}{2}$ along the x-axis and $i\Delta y$ to $(i+1)\Delta y$ along the y-axis.

Therefore, the drag and lift forces are computed by summing the individual contributions of each loop of the mesh over a longitudinal length of a period of the PM array.

4.3 Validation of the Simplified Plate Model

To validate the simplified plate model, a 3D plate FEM model was developed using *Comsol Multiphysics®*. Fig. 4.6 shows this FEM 3D model.

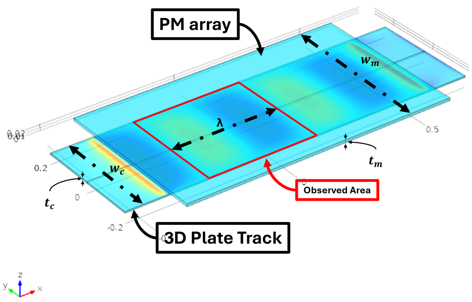

Figure 4.6: FEM 3D model used for validation. The highlighted red box indicates the observed area.

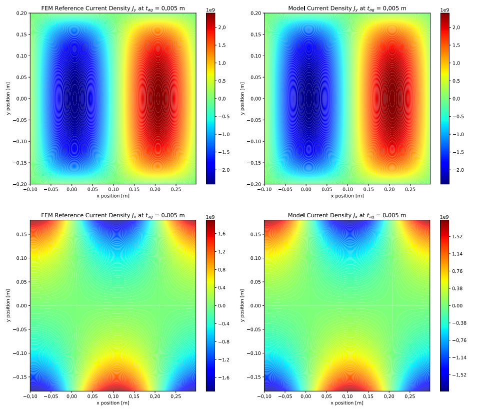

Figure 4.7: Comparison of induced currents J_y (top) and J_x (bottom) between the FEM reference and the model in the observed area for the initial values.

Given the periodicity of the system, the analysis was restricted to a section of the track that includes multiple periods of the PM array. To avoid edge effects from the PM array, the PM array was made larger than the track, although edge effects from the track still appear, they are negligible. Additionally, the track was extended beyond the array to avoid end effects of the track itself. The considered PM array extends over several wavelengths, ensuring that the observed area, highlighted by the red box, remains unaffected by the end effects of the array. The initial parameter values used for the PM-EDS are provided in Table 4.1.

In the simplified plate model, the B_z field is similarly defined as:

$$
\begin{aligned}
A &= 47.18e^{(-14.70t_{gap})} - 2.91 \\
B_z &= A\sin\left(\frac{\pi}{\tau_m}\left(x + \frac{\tau_m}{2}\right)\right)
\end{aligned}
\tag{4.11}
$$

The amplitude function A is determined using the same fitting procedure as previously described in the ladder model.

By varying these parameters similarly to the ladder track model, the validation of the simplified plate model in terms of current and forces was conducted.

Table 4.1: Electromagnetic and Structural Parameters of the Simplified Plate Model (adapted from [10]).

Symbol	Quantity	Value
τ_m	Pole pitch of the PMs	0.2 m
w_m	Width of the PMs	0.4 m
t_m	Thickness of the PMs	0.05 m
t_{ag}	Air gap thickness	5 mm
τ_c	Coil pitch	2 mm
w_c	Width of the track	0.4 m
t_c	Thickness of the track	5 mm
$w_{tc} \times w_{lc}$	Wire cross-section	$t_c \times \tau_c$ mm^2
$\sigma = \rho^{-1}$	Electrical conductivity	3.5×10^7 S/m
v_x	Translational speed	1.15 m/s
Δx	Discretization along x-axis	τ_c m
Δy	Discretization along y-axis	Δx m

4.3.1 Validation of Analytical Model Through Current Densities and Forces Comparisons

The validation of the simplified plate model begins with an examination of the variation in v_x, as illustrated in Fig. 4.8. In this case, the study was limited to a maximum velocity of 20 m/s, adhering to the constraints discussed in the ladder track model. This model demonstrates a clear improvement in accurately predicting the behavior and electromagnetic interactions within a plate track-based PM-EDS system. As anticipated, the error with respect to the FEM reference increases with v_x, primarily due to the omission of the skin effect and the angle of diffusion. The model tends to overestimate the LDR, reflecting an optimistic bias in its predictions.

Next, the validation proceeds by maintaining a constant v_x while varying t_{ag}, as shown in Fig. 4.9. The results demonstrate good alignment between the model and the FEM reference for both J_x and J_y, as well as for the lift and drag forces. The induced current J_y which directly influences the drag force, demonstrates a consistent deviation relative to the FEM reference. This consistency indicates that the analytical model accurately captures the behavior of J_y and F_{drag} with varying air gap distances. The lift force, which is more sensitive to variations in J_x, also shows a relatively low deviation, albeit slightly higher than that observed for the drag.

The next analysis focuses on the effect of the plate's thickness. The results are presented in Fig. 4.10. Due to the model's assumption of uniform current density across the conductor's cross-section, inaccuracies arise for conductors with $t_c > \delta_{skin}$. Since t_c is initially set equal to δ_{skin}, increasing the thickness quickly results in non-negligible errors. Therefore, maintaining an infinitesimally thin plate is recommended to mitigate these effects.

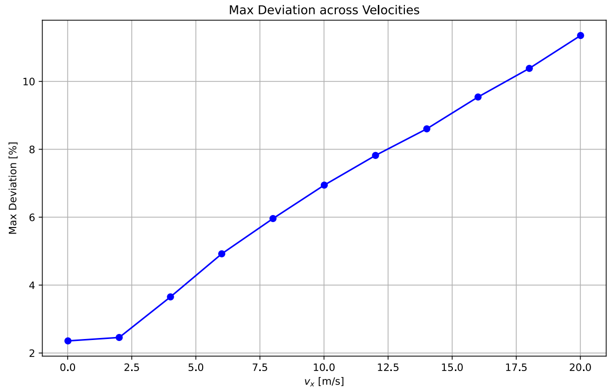

(a) Maximum deviation between model and reference in J_x across velocities.

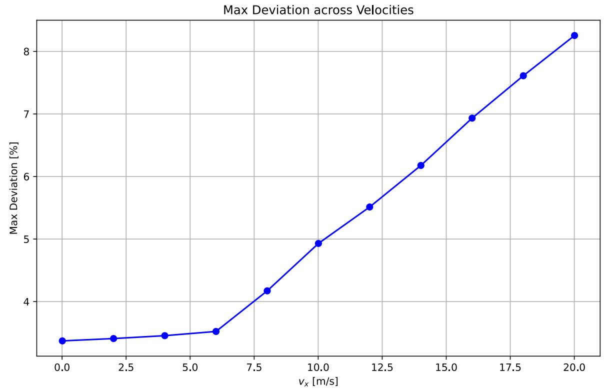

(b) Maximum deviation between model and reference in J_y across velocities.

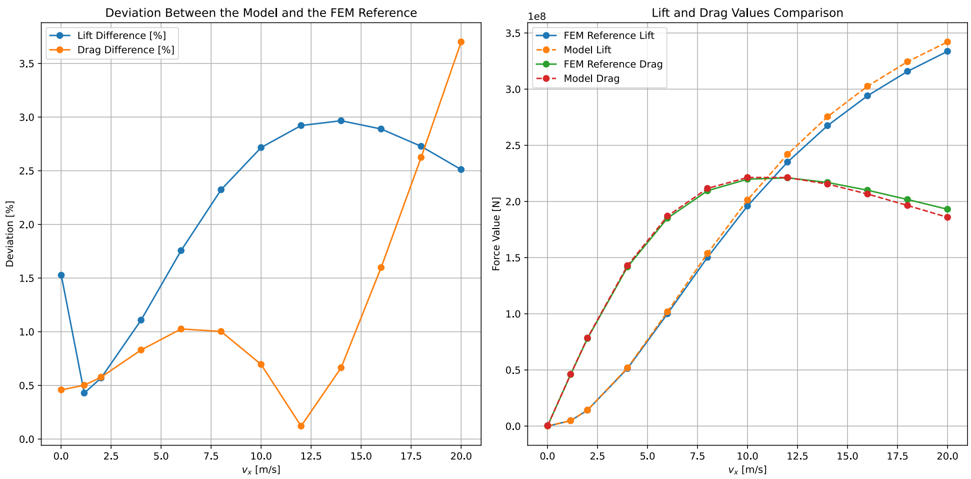

(c) Lift and drag comparison for varying v_x.

Figure 4.8: Validation of the simplified plate model with varying velocity v_x. a) and b) current density analysis. c) force analysis.

The final validation test examines the impact of discretization size $\Delta x = \Delta y$ on the model's accuracy, as shown in Fig. 4.11. For this validation, only the global variables were considered, as explained in Subsection 3.4.1. The results indicate that the forces derived from the FEM reference deviate as the discretization size increases. The behavior of the error in the drag force with increasing $\Delta x = \Delta y$ follows an expected trend, showing a gradual increase in error as the mesh becomes coarser. This is likely due to the reduced resolution in capturing the finer details of the current distribution, which primarily affects the drag force associated with the transverse current component J_y.

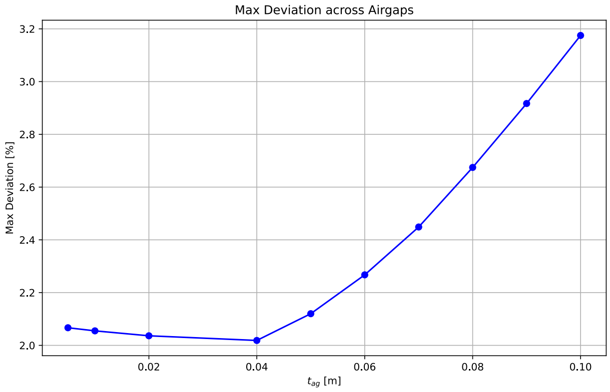

(a) Maximum deviation between model and reference in J_x across air gaps.

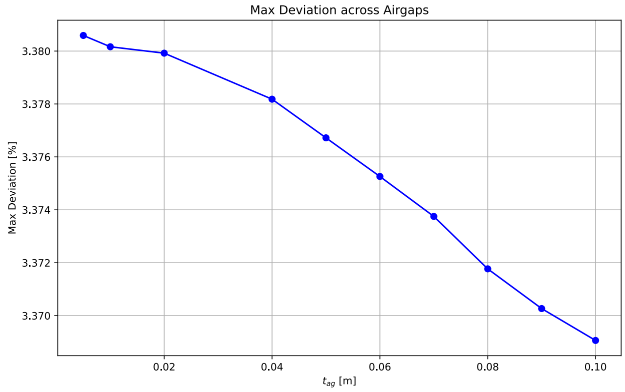

(b) Maximum deviation between model and reference in J_y across air gaps.

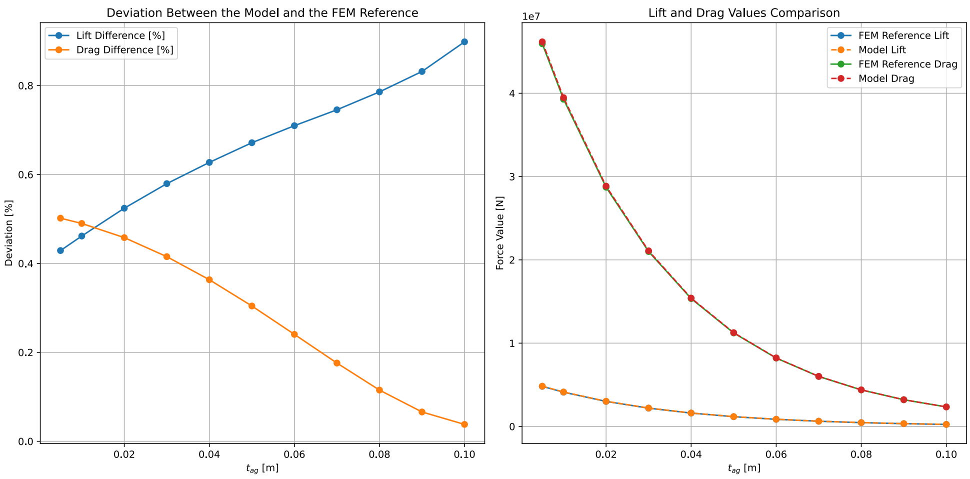

(c) Lift and drag comparison for varying air gap t_{ag}.

Figure 4.9: Validation of the simplified plate model with varying air gap t_{ag}. a) and b) current density analysis. c) force analysis.

However, the lift force error exhibits a more complex pattern. As $\Delta x = \Delta y$ increases, the error fluctuates rather than increasing steadily. This fluctuation likely occurs because, with a coarser mesh, the lift force computation involves averaging, which may sometimes result in more accurate values for this specific case using the parameters from Table 4.1.

In summary, the validation of the simplified plate model shows that it provides accurate results for both drag and lift forces across various parameters. The lift force is more sensitive to changes, particularly with increased thicknesses, but overall, the model offers precise and accurate results for thin plate, free from the velocity-related anomalies observed in the ladder track model.

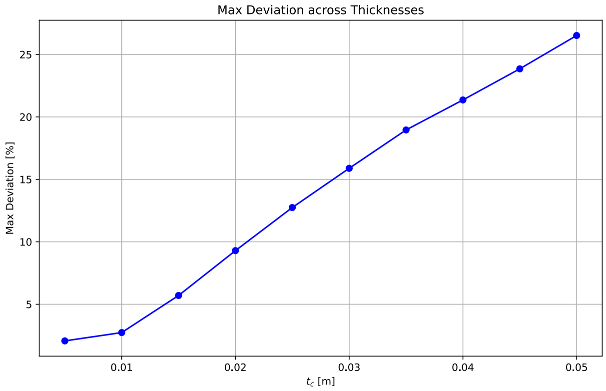

(a) Maximum deviation between model and reference in J_x across thicknesses.

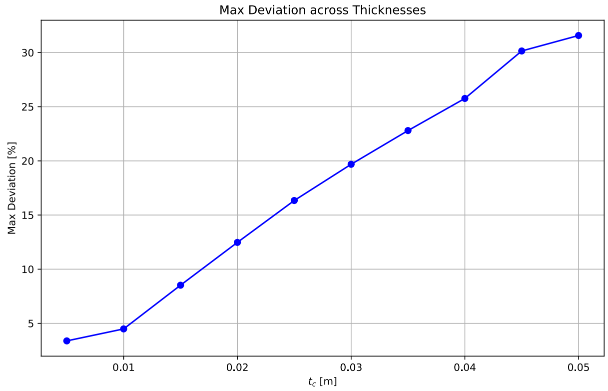

(b) Maximum deviation between model and reference in J_y across thicknesses.

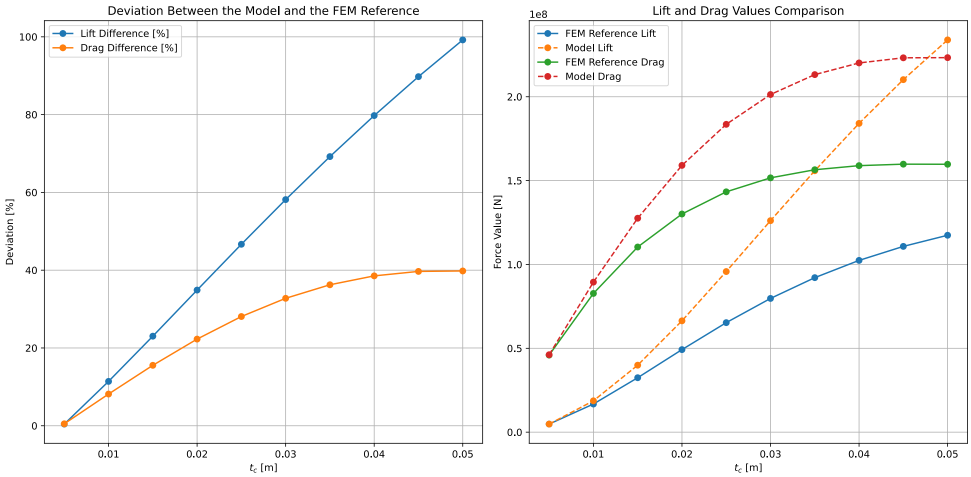

(c) Lift and drag comparison for varying thickness t_c.

Figure 4.10: Validation of the simplified plate model with varying thickness t_c. a) and b) current density analysis. c) force analysis.

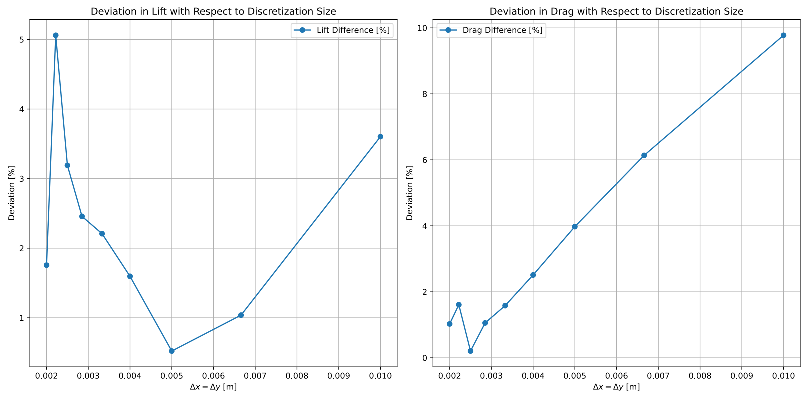

Figure 4.11: Validation of lift and drag forces with respect to the discretization size Δx and Δy. Showing the deviation between the values from the model and from the FEM reference model for the lift and the drag force.

4.4 Conclusion on the Simplified Plate Model

The development and validation of the simplified plate model have been presented in this chapter. This model offers a significant improvement in predicting the electromagnetic behavior of a plate track-based PM-EDS system, providing more precise and accurate results than the previous ladder track model.

The next chapter will build upon the concepts developed here to explore an advanced plate track model, incorporating additional complexities to create a framework for the TO.

Chapter 5

Advanced Periodic Plate Model

In this chapter, the final analytical model of this study is developed. The chapter begins by outlining the key differences between this final model and the previous "simplified" plate model, emphasizing how these enhancements facilitate the application of density-based topology optimization in subsequent chapters. The analytical development of the final model is then presented, building on the strong mathematical foundation established by the previous models. The model's accuracy is validated using the same 3D FEM model, constructed in Comsol Multiphysics®, already employed for the validation of the simplified plate track model. Following this, the introduction of holes into the topology by modifying the resistivity of mesh elements is discussed. The basic concept is explained, and the advanced model's validity and the feasibility of TO are confirmed through validation using the 3D FEM model on two slotted plate configurations.

5.1 From Simplified Plate Model to Advanced Plate Model

In the simplified model, the use of TO algorithms is not feasible since only a single transverse element of the mesh is considered. Given the periodicity in the model, introducing a hole in a row of this slice would effectively create a longitudinal slit along the entire plate track.

To address this limitation, the final model considers a larger slice of the mesh, as depicted in Fig. 5.1. Taking a larger window on the mesh can simply be seen as increasing the size of the coil pitch τ_c.

Within this window, holes can be introduced. In the context of the discrete mesh used, creating holes corresponds to increasing the resistivity of specific mesh elements.

This concept will be further explored in Section 5.3. The following section details the analytical development of the final model.

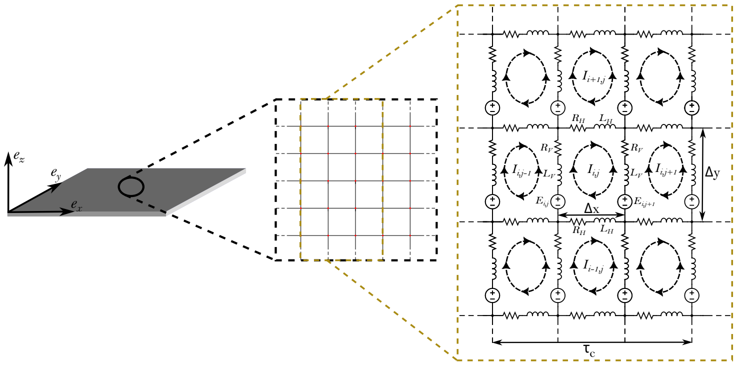

Figure 5.1: 3D plate to discrete advanced plate model.

5.2 Analytical Model Development

The analytical modeling of the advanced plate model closely parallels that of the simplified plate model. The primary distinction lies in the spatial shift value. In previous models, each column of the mesh had a size Δx and represented a shifted version of the adjacent column. The spatial shift value was equal to the coil pitch, with $\tau_c = \Delta x$. In the advanced plate model, the spatial shift value is again defined as τ_c, the size of the slice under consideration. Consequently, the shift size is no longer equal to Δx. As a result, the induced currents at the left and right boundaries of the widow are simply shifted versions of all the induced currents computed within it with a spatial shift equal to τ_c that differs from Δx.

For the remainder of this study, a uniform mesh is assumed, with $\Delta y = \Delta x$ and all branches having the same cross-section. This results in a slice of mesh of size τ_c, with $N_{\text{rows}} = \frac{w_c}{\Delta y}$ and $N_{\text{col}} = \frac{\tau_c}{\Delta x}$, representing the number of rows and columns in the window considered respectively. The equivalent circuit for the advanced plate model is shown in Fig. 5.2.

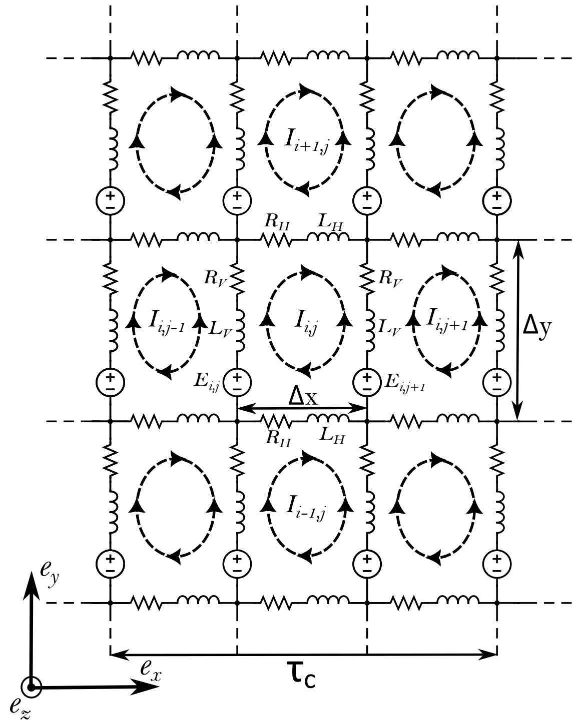

Figure 5.2: Equivalent circuit for the advanced plate model.

5.2.1 Derivation of the Induced Current Formula

Based on the same assumptions and following a similar development as in the previous models, the KVL for the central loop $I_{i,j}$ considering a single harmonic of the system is expressed as:

$$\begin{aligned}
&R_V(I_{i,j} - I_{i,j-1}) + j\omega_k v_x L_{Veq}^{0,0}(I_{i,j} - I_{i,j-1}) + \sum_{p\neq 0}\sum_{l\neq 0} j\omega_k v_x L_{Veq}^{p,l}(I_{i+p,j+l} - I_{i+p,j-1+l})\\
&+ R_V(I_{i,j} - I_{i,j+1}) + j\omega_k v_x L_{Veq}^{0,0}(I_{i,j} - I_{i,j+1}) + \sum_{p\neq 0}\sum_{l\neq 0} j\omega_k v_x L_{Veq}^{p,l+1}(I_{i+p,j+l} - I_{i+p,j+1+l})\\
&+ R_H(I_{i,j} - I_{i+1,j}) + j\omega_k v_x L_{Heq}^{0,0}(I_{i,j} - I_{i+1,j}) + \sum_{p\neq 0}\sum_{l\neq 0} j\omega_k v_x L_{Heq}^{p,l}(I_{i+p,j+l} - I_{i+1+p,j+l})\\
&+ R_H(I_{i,j} - I_{i-1,j}) + j\omega_k v_x L_{Heq}^{0,0}(I_{i,j} - I_{i-1,j}) + \sum_{p\neq 0}\sum_{l\neq 0} j\omega_k v_x L_{Heq}^{p-1,l}(I_{i+p,j+l} - I_{i-1+p,j+l})\\
&= E_{i,j} - E_{i,j+1} \qquad (5.1)
\end{aligned}$$

This equation utilizes new equivalent inductances, defined as follows:

$$L_{Heq}^{0,0} \triangleq L_H^{0,0} + 2\sum_{m=1}^{N_P} L_{Hm}^{0,0}\cos\left(m\omega_k\tau_c\right) \tag{5.2}$$

$$L_{Heq}^{p,l} \triangleq L_H^{p,l} + 2\sum_{m=1}^{N_P} L_{Hm}^{p,l}\cos\left(m\omega_k\tau_c\right) \tag{5.3}$$

$$L_{Veq}^{0,0} \triangleq L_V^{0,0} + 2\sum_{m=1}^{N_P} L_{Vm}^{0,0}\cos\left(m\omega_k\tau_c\right) \tag{5.4}$$

$$L_{Veq}^{p,l} \triangleq L_V^{p,l} + 2\sum_{m=1}^{N_P} L_{Vm}^{p,l}\cos\left(m\omega_k\tau_c\right) \tag{5.5}$$

Here, $L_V^{p,l}$ represents the mutual inductance between a transverse branch of loop $I_{i,j}$ and the corresponding transverse branch of loop $I_{i+p,j+l}$. Similarly, $L_H^{p,l}$ denotes the mutual inductance for longitudinal branches. The terms $L_V^{0,0}$ and $L_H^{0,0}$ are the self-inductances of the transverse and longitudinal branches of loop $I_{i,j}$, respectively. As in the previous model, the index p can be limited to a maximum value p_{max}, since loops too distant in the transverse direction from loop $I_{i,j}$ have a negligible impact through mutual inductance. The index l is restricted to loops within the window, while the index m refers loops in adjacent windows, affecting the induced currents through mutual inductance, limited to a number N_w of adjacent windows. For example, $L_{Vm}^{p,l}$ corresponds to the mutual inductance between a transverse branch of loop $I_{i,j}$ and the corresponding transverse branch of loop $I_{i+p,j+l}$ in slice m. The Fig. 5.3 tries to provides a visual representation of these principles to help the understanding.

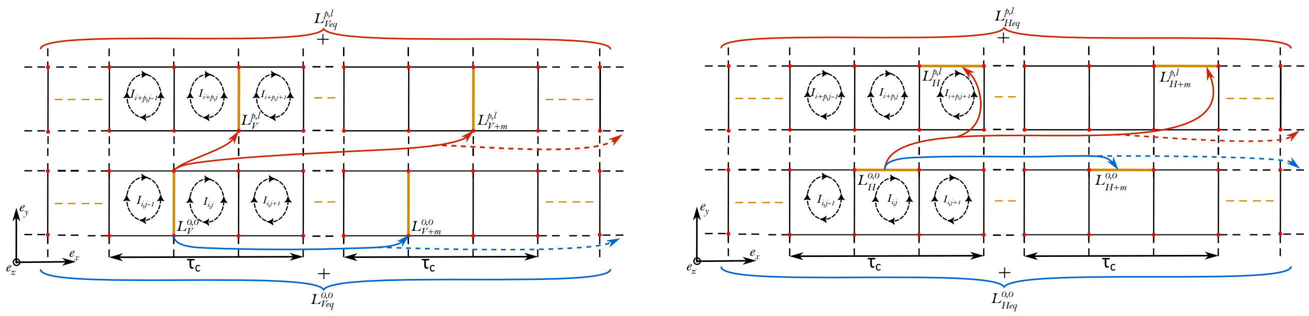

(a) Visualization of $L_{Veq}^{0,0}$ and $L_{Veq}^{p,l}$ for the advanced plate model.

(b) Visualization of $L_{Heq}^{0,0}$ and $L_{Heq}^{p,l}$ for the advanced plate model.

Figure 5.3: Equivalent inductances for the advanced plate model, visualizing the mutual inductance effects in both transverse and longitudinal branches.

In the validation of this model, a value of τ_c equal to the period of the PMs, $\tau_c = \lambda = 2\tau_m$, is selected. This choice will be discussed in Section 6.2. However, it is important to note that the coil pitch can be freely adjusted to take on higher or lower values. The value of the coil pitch significantly influences the behavior of the equivalent inductances, as illustrated in Fig. 5.4. Specifically, in this scenario where $\tau_c = \lambda$, $\cos(m\omega_k\tau_c) = 1$, which effectively eliminates any oscillatory behavior in the equivalent inductances. As a result, the number of adjacent windows considered, N_w, must be sufficiently large to ensure that the induced currents in the further distant loops exert a negligible impact on the slice of mesh τ_c under consideration.

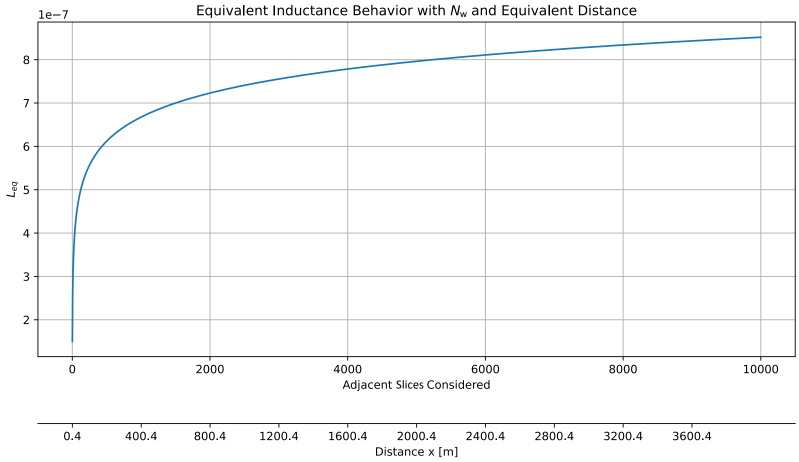

Figure 5.4: Behavior of equivalent inductances with respect to the number of adjacent mesh slices considered in the mutual computation, demonstrating the elimination of oscillatory behavior.

With $w_c = 2\tau_m$ and uniform discretization $\Delta x = \Delta y$, it follows that $N_{\text{rows}} = N_{\text{col}}$ within each mesh window.

Linear algebraic system formulation

The KVL Eq. 5.1 can be rewritten as:

$$\begin{aligned}
&2\left(R_V + j\omega_k v_x L_{Veq}^{0,0} + R_H + j\omega_k v_x L_{Heq}^{0,0}\right) I_{i,j} \\
&+ \sum_{p\neq 0}\sum_{l\neq 0} j\omega_k v_x L_{Veq}^{p,l} I_{i+p,j+l} + \sum_{p\neq 0}\sum_{l\neq 0} j\omega_k v_x L_{Veq}^{p,l+1} I_{i+p,j+l} \\
&+ \sum_{p\neq 0}\sum_{l\neq 0} j\omega_k v_x L_{Heq}^{p,l} I_{i+p,j+l} + \sum_{p\neq 0}\sum_{l\neq 0} j\omega_k v_x L_{Heq}^{p-1,l} I_{i+p,j+l} \\
&- \left(R_V + j\omega_k v_x L_{Veq}^{0,0}\right) I_{i,j-1} - \sum_{p\neq 0}\sum_{l\neq 0} j\omega_k v_x L_{Veq}^{p,l} I_{i+p,j-1+l} \\
&- \left(R_V + j\omega_k v_x L_{Veq}^{0,0}\right) I_{i,j+1} - \sum_{p\neq 0}\sum_{l\neq 0} j\omega_k v_x L_{Veq}^{p,l+1} I_{i+p,j+1+l} \\
&- \left(R_H + j\omega_k v_x L_{Heq}^{0,0}\right) I_{i+1,j} - \sum_{p\neq 0}\sum_{l\neq 0} j\omega_k v_x L_{Heq}^{p,l} I_{i+1+p,j+l} \\
&- \left(R_H + j\omega_k v_x L_{Heq}^{0,0}\right) I_{i-1,j} - \sum_{p\neq 0}\sum_{l\neq 0} j\omega_k v_x L_{Heq}^{p-1,l} I_{i-1+p,j+l} \\
&= E_{i,j} - E_{i,j+1}
\end{aligned} \tag{5.6}$$

For loops located at the left or right edge of the slice, slight modifications are required in the equation. Specifically, the influence of induced currents from the adjacent slices, which are shifted versions of the considered one, must be accounted for.

The induced voltage is calculated using a similar method as in the previous model (Eq. 4.7), with a slight modification. The initial value at $x = 0$, the left edge of the mesh slice, serves as the reference, and subsequent values are computed for each branch by shifting according to the discretization size Δx.

$$E_{i,j} = e^{(1jw_k \cdot \mathrm{j}\Delta x)} \int_{i\Delta_y}^{(i+1)\Delta y} \mathbf{v} \times \mathbf{B} \; dy \tag{5.7}$$

The magnetic field in the system is dynamic, moving with velocity v_x. This movement must be incorporated into the induced voltage calculations to accurately represent the electromagnetic behavior of the system. The velocity v_x is directly multiplied by the magnetic flux difference to compute the induced voltage. Additionally, the exponential term $e^{(1jw_k \cdot \mathrm{j}\Delta x)}$ accounts for the phase shifts introduced by position of the considered discrete branch.

The Eq. 5.6 for each loop within the window considered can be expressed in matrix form as:

$$\mathbf{AI} = \mathbf{B}$$

where:

- $\mathbf{A}$ is the coefficient matrix of size $(N_{\text{rows}} \times N_{\text{col}}) \times (N_{\text{rows}} \times N_{\text{col}})$, incorporating resistive and inductive terms.
- $\mathbf{I}$ is the vector of unknown currents $I_{i,j}$ of size $N_{\text{rows}} \times N_{\text{col}}$.
- $\mathbf{B}$ is the vector of electromotive forces $E_{i,j} - E_{i,j+1}$ of size $N_{\text{rows}} \times N_{\text{col}}$.

The elements of matrix $\mathbf{A}$ are defined as:

For adjacent loops:

$$\begin{aligned}
A_{u,u} &= 2\left(R_V + j\omega_k v_x L_{Veq}^{0,0} + R_H + j\omega_k v_x L_{Heq}^{0,0}\right) \\
A_{u,u\pm1} &= -\left(R_V + j\omega_k v_x L_{Veq}^{0,0}\right) \\
A_{u,u\pm N_{\text{col}}} &= -\left(R_H + j\omega_k v_x L_{Heq}^{0,0}\right)
\end{aligned}$$

For non adjacent loops:

$$\begin{aligned}
A_{u,\text{idx}} &= j\omega_k v_x \left(L_{Veq}^{p,l} + L_{Veq}^{p,l+1} + L_{Heq}^{p,l} + L_{Heq}^{p-1,l}\right) \\
A_{u,\text{idx}-1} &= j\omega_k v_x L_{Veq}^{p,l} \;, \qquad A_{u,\text{idx}+1} = j\omega_k v_x L_{Veq}^{p,l+1} \\
A_{u,\text{idx}+N_{col}} &= j\omega_k v_x L_{Heq}^{p,l} \;, \qquad A_{u,\text{idx}-N_{col}} = j\omega_k v_x L_{Heq}^{p-1,l}
\end{aligned}$$

With $u = iN_{col} + j$ and $idx = (i+p)N_{col} + (j+l)$.

For current loops located in the first column ($j = 0$), the interaction with the left neighbor wraps around to the last column of the same row:

$$A_{u,u-1} \rightarrow A_{u,(j+1)N_{\text{col}}-1} \cdot e^{(-j\omega_k \tau_c)}$$

For current loops in the last column ($j = N_{\text{col}} - 1$), the interaction with the right neighbor wraps around to the first column of the same row:

$$A_{u,u+1} \to A_{u,iN_{col}} \cdot e^{(j\omega_k \tau_c)}$$

The vector of unknown currents $\mathbf{I}$ is:

$$\mathbf{I} = \begin{bmatrix} I_{0,0} \\ I_{0,1} \\ \vdots \\ I_{0,N_{\text{col}}-1} \\ I_{1,0} \\ \vdots \\ I_{N_{\text{row}}-1,N_{\text{col}}-1} \end{bmatrix}$$

The vector $\mathbf{B}$ is:

$$\mathbf{B} = \begin{bmatrix} E_{0,0} - E_{0,1} \\ E_{0,1} - E_{0,2} \\ \vdots \\ E_{0,N_{\text{col}}-1} - E_{0,0}e^{j\omega_k \tau_c} \\ E_{1,0} - E_{1,1} \\ \vdots \\ E_{N_{\text{row}}-1,N_{\text{col}}-1} - E_{N_{\text{row}}-1,0}e^{j\omega_k \tau_c} \end{bmatrix}$$

Thus, the system of equations is expressed as:

$$\mathbf{AI} = \mathbf{B} \tag{5.8}$$

5.2.2 Derivation of the Static Forces

The computation of F_{drag} and F_{lift} in the advanced plate model follows the same fundamental principles as those described in Section 4.2.2. Using the Lorentz force equation (Eq. 4.8), these forces are derived by evaluating the magnetic flux density $\mathbf{B}$ on each branch of the plate, with the integration limits adjusted accordingly.

Additionally, the second method, which involves computing the static forces using the intercepted flux through the discrete loops of the plate, is the preferred one when it comes to the implementation (see Eq. 4.9).

5.2.3 Validation of the Advanced Plate Model

To validate the advanced plate model, the same 3D FEM model using *Comsol Multiphysics®* and described in Section 4.3 was employed (FEM model depicted in Fig. 4.6). The initial parameter values for the analytical model were carefully selected to ensure a meaningful comparison with the FEM model. These parameters, nearly identical to those used for the simplified model, are listed in Table 5.1.

The z-component of the magnetic flux density B_z is defined in Eq. 4.11.

Table 5.1: Electromagnetic and Structural Parameters of the Advanced Plate Model (adapted from [10]).

Symbol	Quantity	Value
τ_m	Pole pitch of the PMs	0.2 m
w_m	Width of the PMs	0.4 m
t_m	Thickness of the PMs	0.05 m
t_{ag}	Air gap thickness	5 mm
τ_c	Coil pitch	0.4 m
w_c	Width of the track	0.4 m
t_c	Thickness of the track	5 mm
$\sigma = \rho^{-1}$	Electrical conductivity	3.5×10^7 S/m
v_x	Translational speed	1.15 m/s
Δx	Discretization along x-axis	0.01 m
Δy	Discretization along y-axis	Δx m
$w_{tc} \times w_{lc}$	Wire cross-section	$t_c \times \Delta x$ mm^2

For the validation of this advanced plate model, the same tests and parameter variations as those performed for the previous model were conducted.

5.2.4 Validation of Analytical Model Through Current Densities and Forces Comparisons

The validation of the advanced plate model began with an examination varying v_x, similar to the previous models, all other parameters being constant at their initial values. The results are presented in Fig. 5.5, where the study was again constrained to a velocity of 20 m/s. As expected, the behavior observed mirrors that of the simplified model, with errors increasing with velocity due to the neglect of the skin effect and the angle of diffusion. The drag force F_{drag} at higher speeds will become smaller than the FEM reference value, leading to an increased error and an over-optimistic prediction of the LDR since the computed lift force is higher than the reference value at high speed.

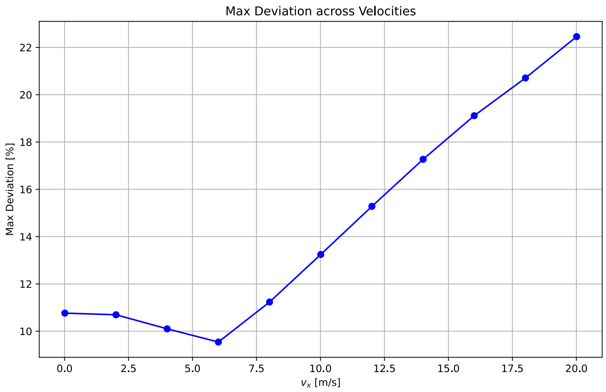

(a) Maximum deviation between model and reference in J_x across velocities.

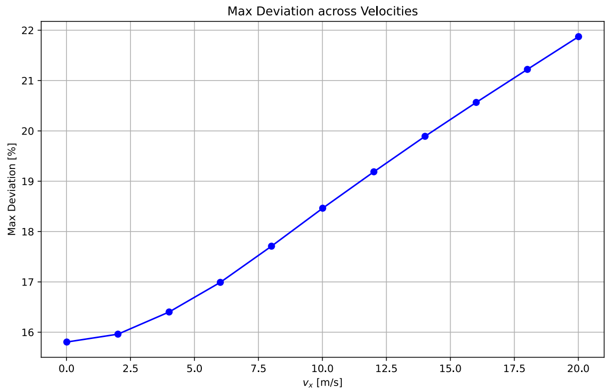

(b) Maximum deviation between model and reference in J_y across velocities.

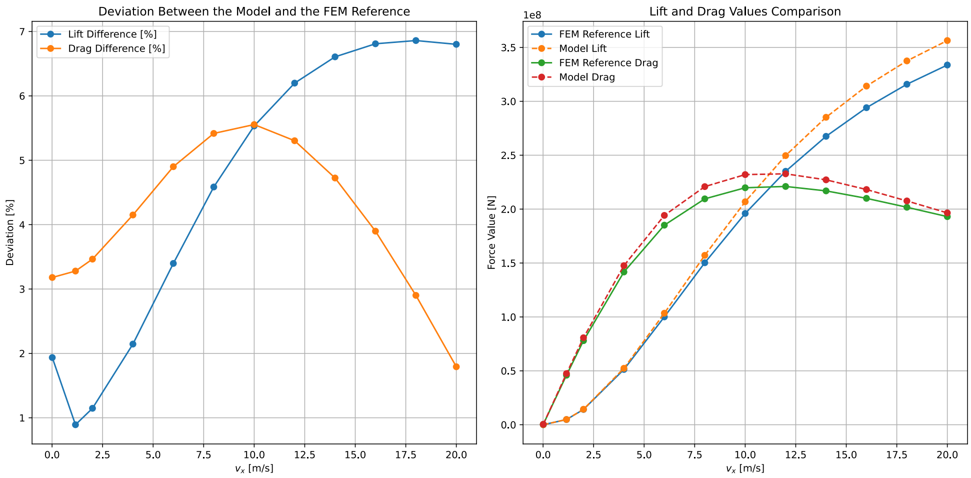

(c) Lift and drag comparison for varying v_x.

Figure 5.5: Validation of the advanced plate model with varying velocity v_x. a) and b) current density analysis. c) force analysis.

With v_x held constant, t_{ag} was varied, as shown in Fig. 5.6. The results once again align with those obtained from the simplified model.

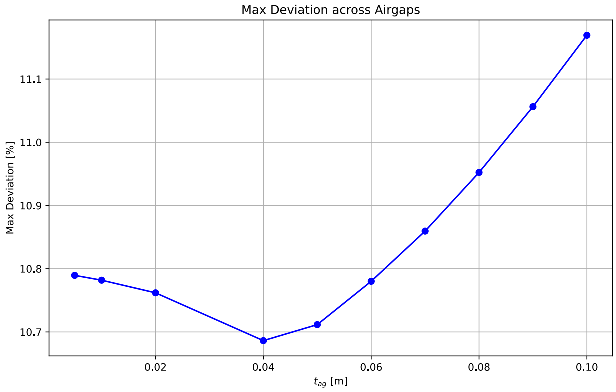

(a) Maximum deviation between model and reference in J_x across air gaps.

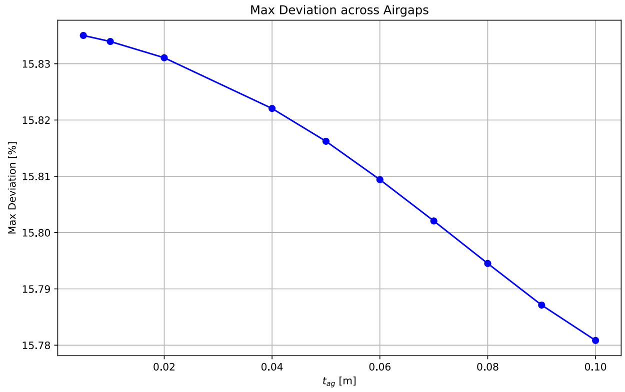

(b) Maximum deviation between model and reference in J_y across air gaps.

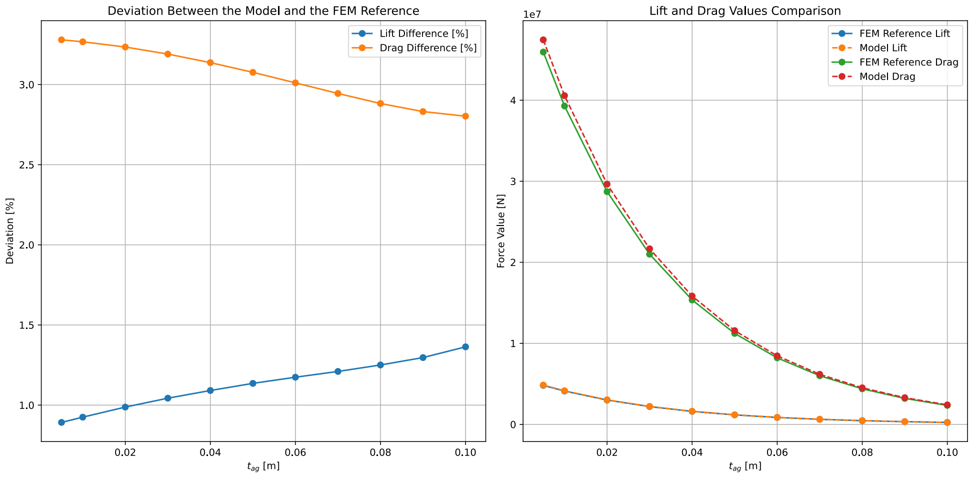

(c) Lift and drag comparison for varying air gap t_{ag}.

Figure 5.6: Validation of the advanced plate model with varying air gap t_{ag}. a) and b) current density analysis. c) force analysis.

The effect of conductor thickness was evaluated, with results depicted in Fig. 5.7. As with the simplified model, the assumption of uniform current density leads to similar inaccuracies when the thickness exceeds δ_{skin}, which is rapidly the case given the speed considered of $v_x = 1.15$ m/s, and the thickness of the plate t_c, roughly already equal to the depth of penetration.

Lastly, the impact of discretization size $\Delta x = \Delta y$ was examined, as shown in Fig. 5.8. Due to the increased complexity of the advanced model, more computational resources are required, limiting the feasible discretization size to $\Delta x = \Delta y = 1 \times 10^{-2}$ m to balance resource usage and computation time. The observed reduction in lift force error as the discretization size increases may be linked to the coarse grid smoothing out fluctuations in the vertical flux variations, leading to a more stable prediction of the lift force. Optimizing the model to reduce computational demands and processing time could allow for finer discretization, potentially aligning the results even more closely with those from the simplified plate model.

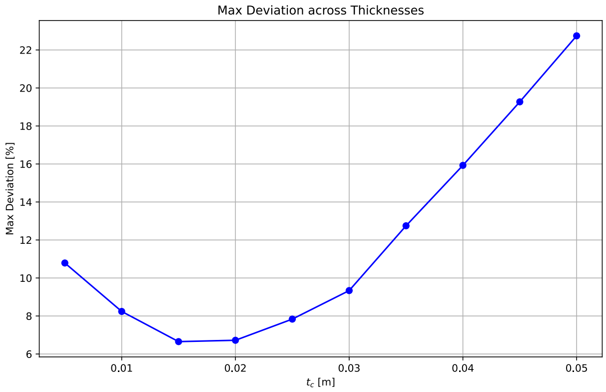

(a) Maximum deviation between model and reference in J_x across thicknesses.

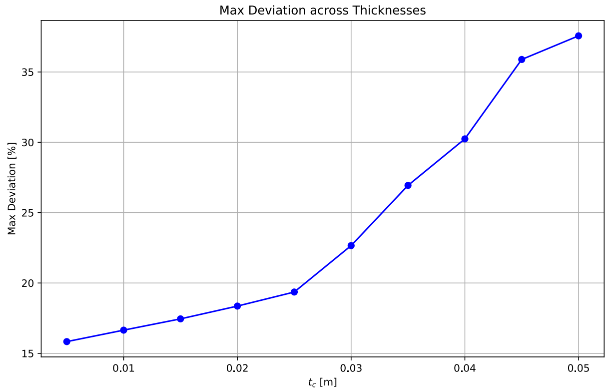

(b) Maximum deviation between model and reference in J_y across thicknesses.

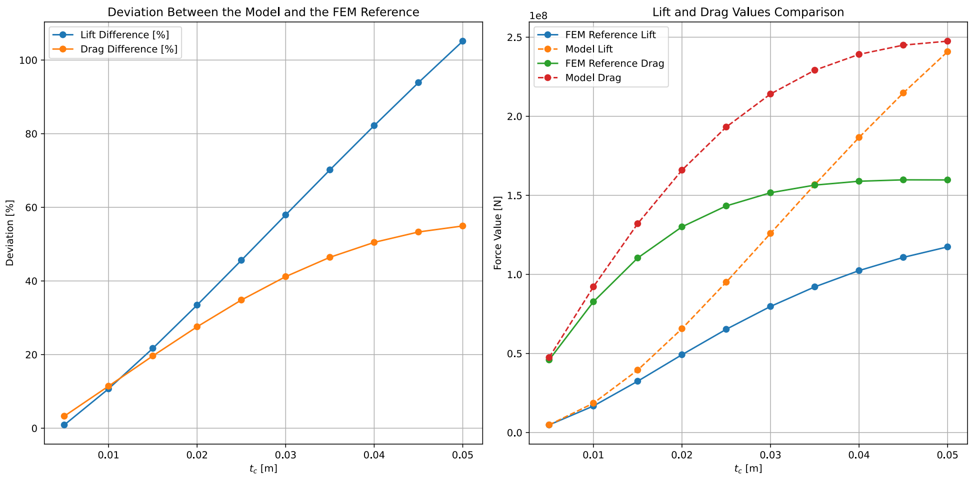

(c) Lift and drag comparison for varying thickness t_c.

Figure 5.7: Validation of the advanced plate model with varying thickness t_c. a) and b) current density analysis. c) force analysis.

In summary, the advanced plate model exhibits a behavior that matches the simplified model when compared to the FEM reference results, with primary differences arising from the increased computational demands and therefore the coarser meshing. Although the errors are slightly larger due to coarser discretization, the model remains accurate in predicting the electromagnetic interactions within the plate. This makes it suitable for further studies, particularly those involving TO, where the model's ability to predict interactions under varying topologies is crucial.

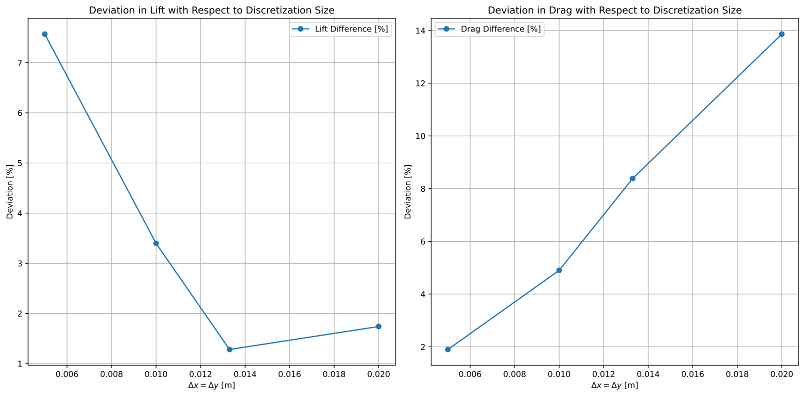

Figure 5.8: Validation of lift and drag forces with respect to the discretization size Δx and Δy. Showing the deviation between the values from the model and from the FEM reference model for the lift and the drag force.

5.3 Topology Modification

5.3.1 Resistivity Adjustments and Simulation of Holes

The advanced plate model enables change in topology by allowing for modifications in the resistivity of mesh elements contain in a window of size τ_c in the conductive sheet. This section details the adaptations made to the advanced model to incorporate resistivity changes, thereby facilitating the creation of holes within the sheet.

In this model, resistances are calculated based on the material resistivity and the geometrical dimensions of each element. As discussed in Section 3.2, the model development considered that the discrete transverse and longitudinal branches of the lumped parameter circuits comprise branches from two distinct mesh elements. By assigning a resistivity to each mesh element, the resistances in the advanced model are expressed as follows:

$$
\begin{aligned}
R_{Vl} &= \frac{\Delta y}{2 w_{tc} w_{lc}} \left(\rho_{bl} + \rho_{ul}\right), \\
R_{Vr} &= \frac{\Delta y}{2 w_{tc} w_{lc}} \left(\rho_{br} + \rho_{ur}\right), \\
R_{Hu} &= \frac{\Delta x}{2 w_{tc} w_{lc}} \left(\rho_{ul} + \rho_{ur}\right), \\
R_{Hb} &= \frac{\Delta x}{2 w_{tc} w_{lc}} \left(\rho_{ll} + \rho_{lr}\right).
\end{aligned}
\tag{5.9}
$$

In these equations, the subscripts associated with ρ refer to the specific positions of the mesh elements in a loop. The indices bl, br, ul, and ur denote bottom-left, bottom-right, upper-left, and upper-right, respectively. Fig. 5.9 provides a visual representation of this concept. Each branch previously considered in the analytical modeling is now divided into two, allowing for the independent adjustment of the resistivity of each mesh element.

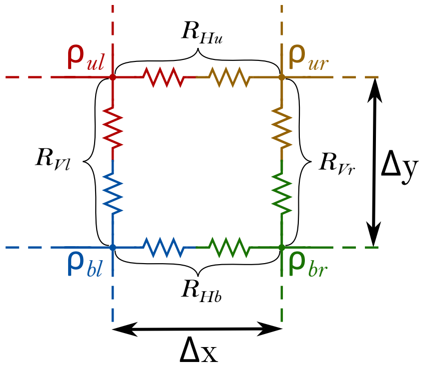

Figure 5.9: Simplified Visual representation of the modified resistance equation.

To simulate holes within the conductive sheet, the resistivity is set to a very high value, effectively representing an open circuit or zero conductivity. This approach enables the definition of specific regions within the slice of mesh where resistivity values can be increased to create holes.

5.3.2 Short Validation of Slotted Conductive Sheet Topologies

The validation process employs the same 3D FEM model as previously described, but introduces holes within the track to assess the model's accuracy in simulating the effects of topology changes on the track. Two distinct hole patterns are considered: the first pattern involves a simple central hole within the window of size $\tau_c = 2\tau_m$, while the second pattern consists of a more complex arrangement. This step is crucial for ensuring that the model accurately simulates the influence of holes introduction on the electromagnetic properties of the conductive sheet.

To simulate a hole, the electrical resistivity of the material ($\rho = 1/\left(3.5 \times 10^7\right) [\Omega \cdot m]$) within a mesh element is increased by a factor K. A sensitivity analysis was conducted using the second hole configuration to determine an appropriate factor K. The factor was incrementally increased starting from $K = 0$, and the resulting percentage change in the computed forces was monitored. The factor was considered sufficiently high to represent a hole in the mesh when the percentage change in forces became negligibly small. Fig. 5.10

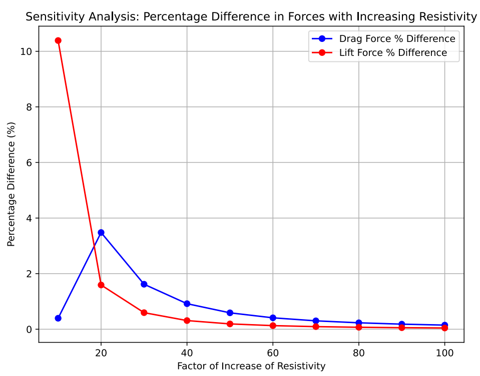

Figure 5.10: Sensitivity analysis: Percentage change in forces as resistivity factor K increases.

presents the graph illustrating the percentage change in forces as K increases. This analysis was performed using the same parameters as those for the advanced plate model, as specified in Table 5.1, but with $v_x = 18$ m/s. The starting values for $K = 0$ thus correspond to the lift and drag forces obtained with the advanced model using a simple conductive sheet at this given velocity and without holes.

Based on this analysis, a resistivity factor of $K = 60$ was selected as it results in a percentage change of less than 0.5%, making it a relatively good choice for simulating a hole.

By applying this factor to create holes in the analytical model, the changes in lift and drag forces can now be compared with the FEM reference model. This comparison validates whether the model accurately predicts the changes in electromagnetic interactions when the topology is altered. The comparison of the current density along the y-axis (J_y) and x-axis (J_x) for the two tested configurations is shown in Fig. 5.11 and Fig. 5.12. These tests were conducted using the parameters detailed in Table 5.1 with $v_x = 1.15$ m/s.

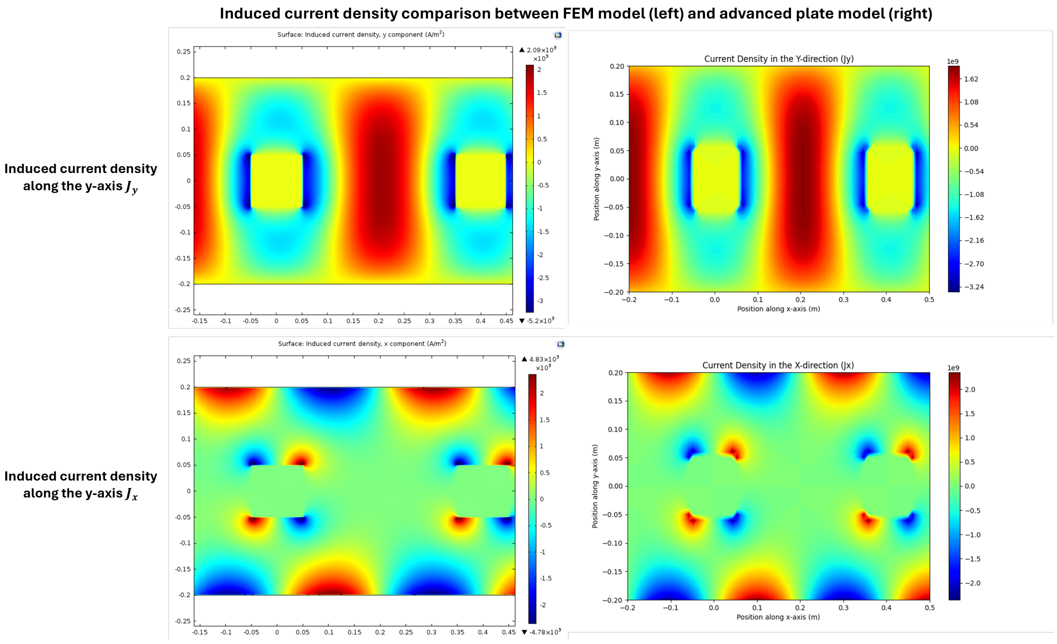

Figure 5.11: Comparison of current density distributions (J_y and J_x) between the FEM reference model (left) and the advanced model (right) for the first hole configuration. Top row: J_y; Bottom row: J_x.

The results indicate good agreement, with differences between the advanced model and the FEM reference model in lift and drag forces being 19% and 1.7%, respectively, for the single-hole configuration, and 6.2% and 2.5% for the second configuration. The lift force again being more sensitive.

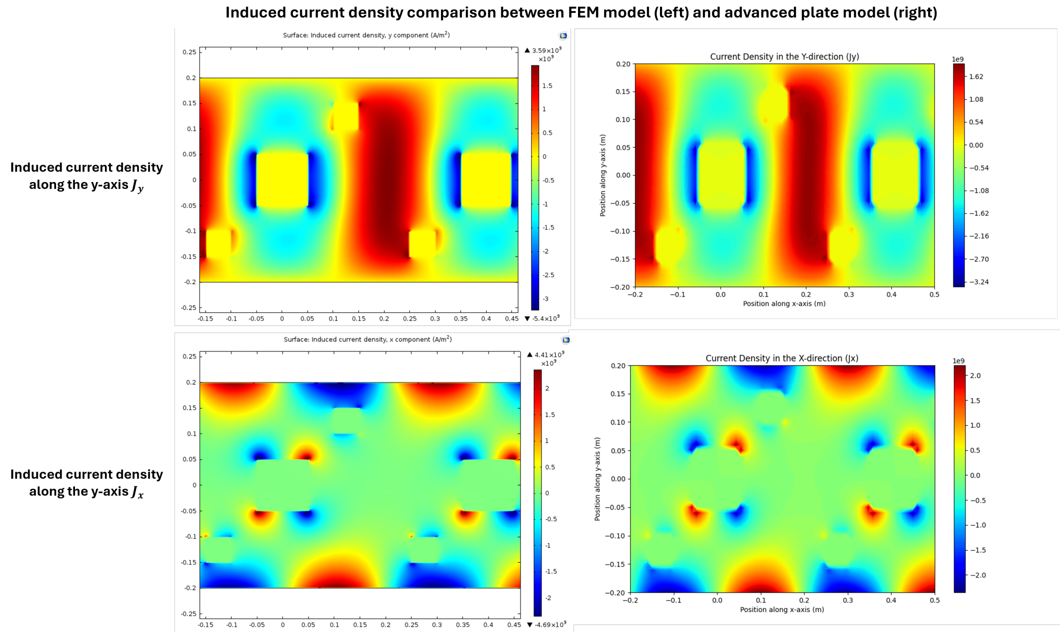

Figure 5.12: Comparison of current density distributions (J_y and J_x) between the FEM reference model (left) and the advanced model (right) for the second hole configuration. Top row: J_y; Bottom row: J_x.

These validations suggest that the advanced model effectively replicates the behavior observed in the 3D FEM reference model when introducing holes in the conductive sheet, highlighting its potential for use in further density-based TO.

5.4 Conclusion on the Advanced Plate Model

The advanced plate model's ability to modify the resistivity of elements within a mesh slice establishes a strong foundation for density-based topology optimization. This enhancement enables the exploration of diverse conductive sheet topologies, facilitating the optimization of PM-EDS system design and performance. With this groundwork laid, the subsequent chapter will focus on the practical application of a density-based TO method.

Chapter 6

Topology Optimization

In this chapter, the fundamental principles and practical applications of topology optimization within the context of this study are explored. The chapter begins with a comprehensive review of the state of the art in topology optimization tracing its historical evolution and its expansion into various engineering domains, including electromagnetism. Following this, the fundamental concepts and problem formulation of topology optimization are outlined, providing a solid foundation for understanding the optimization processes employed in this study. The chapter then transitions into a discussion on the specific application of topology optimization to the PM-EDS system. Here, the focus is on leveraging density-based topology optimization to enhance the system's performance, efficiency, and material usage.

6.1 State of the Art in Topology Optimization

The field of topology optimization has evolved into a vast and multifaceted domain within engineering, encompassing a wide range of applications from structural design to electromagnetism. Given the extensive scope of this discipline, it is important to recognize that the following state of the art offers only a glimpse into the broader landscape. This focused overview aims to elucidate key methodologies and approaches relevant to the context of the present study. Interested readers can refer to [66]-[68] among other papers for a broader view on this topic.

6.1.1 Historical Background and Evolution

Topology optimization is a sophisticated design method that has and still is revolutionizing engineering design across multiple disciplines. The roots of topology optimization can be traced back to the late 20th century when structural optimization techniques began to gain prominence. The early work in this area primarily focused on size and shape optimization, where the goal was to optimize the dimensions or the shape of a structure under given constraints. However, these methods were limited to predefined configurations, unable to explore new design possibilities where the topology, or the material layout itself, could be altered.

The breakthrough in topology optimization came with the development of methods that allowed the optimization of material distribution within a design domain without predefining the structure's shape. The pioneering work by Bendsøe and Kikuchi in 1988 [69] introduced the concept of topology optimization in the context of structural mechanics, where they utilized a homogenization method. This work laid the foundation for the vast field of topology optimization that we see today. Indeed, the method has expanded beyond structural mechanics into multiple other fields such as electromagnetism [70]-[75], fluid dynamics [76], thermal systems [77], acoustics [78],[79] and continues to intrigue, giving rise to new discoveries and innovations.

6.1.2 Fundamental Concepts

At its core, topology optimization aims to determine the optimal material distribution within a given design domain to achieve the best possible performance according to a specified objective function while satisfying a set of constraints that can be structural or performance-related, among others.

6.1.3 Topology Optimization Problem Formulation

A topology optimization problem is typically formulated as a constrained optimization problem, minimizing an objective function, subject to constraints that can be mathematically expressed as:

$$\begin{aligned}
\text{Objective:} \quad & \min_{\boldsymbol{\theta}} \; f(\mathbf{u}(\boldsymbol{\theta}), \boldsymbol{\theta}) \\
\text{Subject to:} \quad & g_i(\mathbf{u}(\boldsymbol{\theta}), \boldsymbol{\theta}) \leq 0, \quad i = 1, \ldots, m \\
& h_j(\mathbf{u}(\boldsymbol{\theta}), \boldsymbol{\theta}) = 0, \quad j = 1, \ldots, p \\
& \theta_{\text{low}} \leq \boldsymbol{\theta} \leq \theta_{\text{high}}
\end{aligned}$$

where:

- $\boldsymbol{\theta}$ represents the vector of design variables, which is bounded by θ_{low} and θ_{high}.
- $f(\mathbf{u}(\boldsymbol{\theta}), \boldsymbol{\theta})$ is the objective function. The term $\mathbf{u}(\boldsymbol{\theta})$ denotes the state variable, which is the solution to a governing physical problem (e.g., electromagnetic field, structural displacement) dependent on the design variables $\boldsymbol{\theta}$.
- $g_i(\mathbf{u}(\boldsymbol{\theta}), \boldsymbol{\theta})$ represents inequality constraints, functions of both the state variable $\mathbf{u}(\boldsymbol{\theta})$ and the design variables $\boldsymbol{\theta}$.
- $h_j(\mathbf{u}(\boldsymbol{\theta}), \boldsymbol{\theta})$ represents equality constraints, which are less common in topology optimization.

The optimization process is iterative, starting with an initial guess of the design variables and progressively updating until the objective function is minimized (or maximized) subject to the constraints. The update of the design variables is done through an “optimizer” [80]. Generally, there are two main kinds of optimizers, each with their pros and cons: gradient-based or gradient-free optimization algorithms. The former necessitate the computation of the gradient, also called sensitivity, of the objective function with respect to the design variables $\frac{dF}{d\theta}$. These gradient-based optimizers offer a faster convergence speed but tend to easily be trapped in local optima in the case of non-convex design spaces [80]. While gradient-free optimizers do not require the knowledge of the sensitivity, which can sometimes be difficult to compute, they tend to be more computationally demanding [75].

One of the most widely used gradient-based algorithms in topology optimization, and the optimizer we focus on in this study, is the Method of Moving Asymptotes (MMA), a gradient-based optimizer particularly well-suited for large-scale problems with many design variables and constraints, developed by Krister Svanberg in the late 1980s [81]. Convex functions are easier to optimize; this method leverages this by approximating the objective function and constraints with convex functions and solving the optimization problem by iteratively updating the design variables through convex optimization subproblems. The name "moving asymptotes" refers to the update in the bounds of the design variables at each iteration. More details on this method can be found in [81],[82]. In this study, an open-source implementation of the MMA algorithm was adapted to fit the specific needs of this research. This implementation is available on GitHub [83].

Obviously, using this gradient-based optimizer requires computing the sensitivity of the objective function with respect to the design variables. To do so, one of the most commonly used methods, and used in this study, is the Adjoint Variable Method [73],[75],[84] [85], a powerful technique that efficiently computes these gradients, especially for large numbers of design variables. In this section, the AVM is briefly described.

Here, the AVM is applied to a simplified system that aligns with the problem developed in this study. The system is expressed as [75],[86]:

$$\mathbf{A}(\boldsymbol{\theta})\mathbf{u} = \mathbf{B} \tag{6.1}$$

where $\mathbf{A}(\boldsymbol{\theta})$ is a matrix dependent on the design variables $\boldsymbol{\theta}$, $\mathbf{u}$ is the state variable (e.g., induced current), and $\mathbf{B}$ is the known right-hand side vector, which may represent external forces or other effects in the system.

The total derivative of the objective function $f(\mathbf{u}(\boldsymbol{\theta}), \boldsymbol{\theta})$ with respect to the design variables $\boldsymbol{\theta}$, is given as:

$$\frac{df}{d\boldsymbol{\theta}} = \frac{\partial f}{\partial \boldsymbol{\theta}} + \frac{\partial f}{\partial \mathbf{u}} \cdot \frac{d\mathbf{u}}{d\boldsymbol{\theta}} \tag{6.2}$$

However, directly calculating $\frac{d\mathbf{u}}{d\boldsymbol{\theta}}$ is computationally expensive. To overcome this, the AVM will introduce an adjoint variable $\boldsymbol{\lambda}$. To do so, we first give the residual equation of the system as:

$$\mathbf{L}(\mathbf{u}(\boldsymbol{\theta}), \boldsymbol{\theta}) = \mathbf{A}(\boldsymbol{\theta})\mathbf{u} - \mathbf{B} = 0 \tag{6.3}$$

Taking the total derivative of the residual equation with respect to $\boldsymbol{\theta}$, we obtain:

$$\frac{d\mathbf{L}}{d\boldsymbol{\theta}} = \frac{\partial \mathbf{L}}{\partial \boldsymbol{\theta}} + \frac{\partial \mathbf{L}}{\partial \mathbf{u}} \cdot \frac{d\mathbf{u}}{d\boldsymbol{\theta}} = 0 \tag{6.4}$$

Substituting the expression for the residual $\mathbf{L}(\mathbf{u}(\boldsymbol{\theta}), \boldsymbol{\theta})$, we have:

$$\frac{\partial \mathbf{A}(\boldsymbol{\theta})\mathbf{u}}{\partial \boldsymbol{\theta}} + \mathbf{A}(\boldsymbol{\theta}) \cdot \frac{d\mathbf{u}}{d\boldsymbol{\theta}} = 0 \tag{6.5}$$

Rearranging, we obtain:

$$\mathbf{A}(\boldsymbol{\theta}) \cdot \frac{d\mathbf{u}}{d\boldsymbol{\theta}} = -\frac{\partial \mathbf{A}(\boldsymbol{\theta})\mathbf{u}}{\partial \boldsymbol{\theta}} \tag{6.6}$$

Introducing Eq. 6.6 into the total derivative in Eq. 6.2 gives:

$$\frac{d\mathbf{f}}{d\boldsymbol{\theta}} = \frac{\partial \mathbf{f}}{\partial \boldsymbol{\theta}} + \frac{\partial \mathbf{f}}{\partial \mathbf{u}} \cdot \left(-\mathbf{A}^{-1} \frac{\partial \mathbf{A}(\boldsymbol{\theta})\mathbf{u}}{\partial \boldsymbol{\theta}} \right) \tag{6.7}$$

The adjoint variable $\boldsymbol{\lambda}$ can now be chosen such that the term multiplying $\frac{d\mathbf{u}}{d\boldsymbol{\theta}}$ vanishes, leading to the adjoint equation:

$$\mathbf{A}^T(\boldsymbol{\theta})\boldsymbol{\lambda} = -\frac{\partial f}{\partial \mathbf{u}} \tag{6.8}$$

Solving this adjoint equation yields the adjoint variable $\boldsymbol{\lambda}$, which can then be used to compute the sensitivity of the objective function as:

$$\frac{df}{d\boldsymbol{\theta}} = \frac{\partial f}{\partial \boldsymbol{\theta}} + \boldsymbol{\lambda}^T \frac{\partial \mathbf{A}(\boldsymbol{\theta})}{\partial \boldsymbol{\theta}} \mathbf{u} \tag{6.9}$$

In summary, the AVM provides an efficient method for calculating gradients in optimization problems, particularly when dealing with large-scale systems with many design variables, as it reduces the problem to solving only two linear systems: once for the state variable $\mathbf{u}$, and once for the adjoint variable $\boldsymbol{\lambda}$[75],[86].

6.1.4 Overview of Topology Optimization Approaches

Topology optimization has evolved into a highly versatile and powerful design tool with multiple approaches developed to address various engineering challenges. Each approach has its own strengths, weaknesses, and suitable application domains. Here, we provide a quick overview of two major topology optimization approaches: density-based methods [67] and level-set methods [15].

Density-Based Methods

The density-based method is the most widely used approach in topology optimization. It was first introduced in the late 1980s and has since become the foundation for many topology optimization applications.

In these methods, the design domain Ω is discretized, and each element is assigned a design variable, noted $\theta(\mathbf{x})$, representing its material density. A value of 0 indicates a void element at point $\mathbf{x}$, and a value of 1 indicates a point occupied by material. This discrete problem is relaxed to allow for intermediate values of the density, leading to a continuous design variable where $0 < \theta(\mathbf{x}) < 1$. This relaxation enables the use of gradient-based optimization algorithms, but it also leads to the presence of gray-scale regions. These gray areas representing partially present material can be challenging to interpret as mention by Sanogo, Satafa and Messine in [74]. Intermediate densities are penalized to encourage convergence to a binary 0-1 solution.

This penalization is often carried out by a judiciously choosing the Material Interpolation Scheme (MIS), making these gray-scale values less attractive to the optimizer. An MIS is a function $g(\theta(\mathbf{x}))$ that gives the material's properties for a given density value $\theta(\mathbf{x})$ at each point in the design domain Ω.

A well-known scheme is the Simplified Isotropic Material with Penalization (SIMP) approach, also called the power-law approach, first introduced by Bendsøe in [87]. In general, the power-law interpolation in electromagnetic topology optimization is defined as follows [14],[75]:

$$g(\theta(x, y)) = p_{\min} + (p_{\max} - p_{\min})\theta^n(x, y)$$

where $g(\theta(x, y))$ represents the property of the material at a point of the domain (x, y), $p_{\min}$ and $p_{\max}$ are the minimum and maximum property values, respectively, and $n > 1$ is the penalty factor. Increasing the penalty factor n reduces the likelihood of gray-scale regions by encouraging a binary material distribution. However, as mentioned in [74], a too-high penalty factor can lead to convergence problems.

Another MIS that aims to penalize the intermediate values of the design variables is the Rational Approximation of Material Properties (RAMP). Denoting $\theta(x, y)$ by θ to simplify the notation, the RAMP or rational interpolation is defined as [74],[14]:

$$g(\theta)) = p_{min} + \frac{(p_{max} - p_{min}) \cdot \theta}{1 + q(1 - \theta)}$$

with $q > 0$ as the penalization factor.

Fig. 6.1 illustrates the effect of increasing the penalty factor for these two schemes, effectively showing that the increase of the penalty factor implies a decrease in the intermediate values.

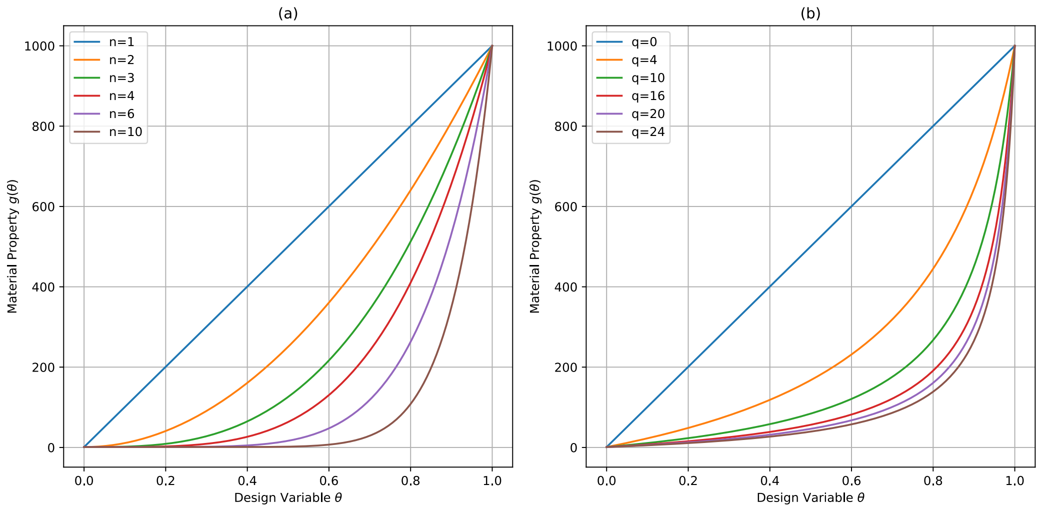

Figure 6.1: Material density interpolation schemes using a) the SIMP polynomial method and b) the RAMP method. Graph for the relative permeability $g(\theta)$ with limited values $(p_{min}, p_{max}) = (1, 1000)$ and different values of penalty factors (adapted from [14]).

Level-Set Methods

The level-set method [88],[89] is a boundary-based approach and is another popular method in topology optimization, particularly well-suited for problems where a clear interface between material and void is essential. This method represents the design domain using a level-set function $\phi(x)$ expressing the void or material domain by its sign, where:

$$\phi(x) = \begin{cases} > 0 & \text{for } x \text{ inside the material region,} \\ = 0 & \text{for } x \text{ on the boundary,} \\ < 0 & \text{for } x \text{ outside the material region.} \end{cases}$$

The boundary of the material region is represented by the zero level set of $\phi(x)$. The optimization process involves evolving the level-set function over time to minimize the objective function while satisfying constraints. The evolution of the level-set function is dictated by the Hamilton-Jacobi equation [75, 90], which governs the time-dependent behavior of the interface represented by the level-set function. Fig. 6.2 illustrates a fundamental example of level-set-based topology optimization, demonstrating the concept of the level-set function.

The general level-set method does not allow for the creation of new holes in the design. Indeed, holes in the initial guess design can only be merged or removed [80], and hence, the final design can therefore be sensitive to the initial guess.

As discussed by Gangl and Langer in [73], the introduction of new infinitesimal holes within the design domain can be achieved through the sensitivity

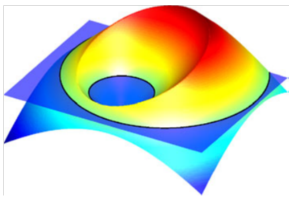

(a) An example of an level-set function ϕ.

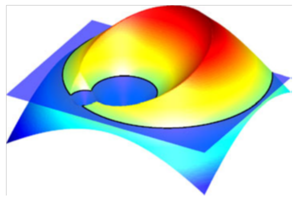

(b) An updated level-set function ϕ.

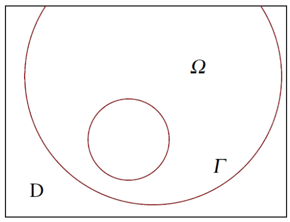

(c) The material domain Ω corresponding to a.

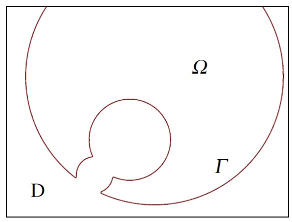

(d) The updated material domain Ω corresponding to b.

Figure 6.2: An example of the the working principal of Level-set method with the level-set function ϕ and the corresponding material domain Ω before and after a design update [15].

of the objective function with respect to the addition of such holes. This sensitivity is encapsulated by the topological derivative.

6.2 Application of Topology Optimization to the PM-EDS System

This section delves into the practical implementation of a density-based TO method within the context of this study, focusing on maximizing system performance, efficiency and cost through strategic material distribution within the conductive track. The primary objective of this study is not to develop designs that are immediately ready for manufacturing, but rather to explore innovative and efficient topologies that hold potential for further investigation and optimization. Consequently, the study will adhere to the basics of topology optimization, focusing on the discovery of promising design configurations rather than final, manufacturable solutions.

In this study, the design domain, which is generally discretized into finite elements, is defined within the advanced plate model presented in Chapter 5. The design domain corresponds to the discrete mesh considered within a segment of size τ_c in the advanced model, as illustrated in Fig. 5.2, and is then repeated indefinitely in the longitudinal direction. The design domain of size τ_c was chosen to correspond to the wavelength λ of the magnetic field produced by the PMs array.

Selecting $\tau_c = \lambda$ ensures that the optimization process captures the full range of the magnetic field interactions within a complete period of the PMs array. A larger design slice $\tau_c > \lambda$ would result in repetitive patterns of holes across the considered slice, adding unnecessary complexity and computational overhead without providing additional insights. Conversely, a smaller design $\tau_c < \lambda$ could reduce the computational burden but may miss critical interactions that occur over a full wavelength, potentially leading to suboptimal designs.

6.2.1 Formulation of the Optimization Problem

The primary objective is to optimize the topology of the conductive track to enhance key performance metrics such as the LDR, minimize the drag force, maximize the lift force, or maintain a certain level of performance while reducing material usage and, consequently, the initial cost. These metrics are critical for improving the efficiency and effectiveness of the system, as discussed in Chapter 2.

The optimization problem is initially formulated with the objective of minimizing the drag force F_{drag}, while ensuring that the lift force F_{lift} remains above a specified threshold $F_{\text{lift, min}}$. This strategy indirectly maximizes the LDR by prioritizing drag reduction while maintaining sufficient lift to ensure the vehicle's proper operation.

The optimization problem can be mathematically formulated as follows:

$$\begin{aligned} \text{Objective:} \quad & \min_{\boldsymbol{\theta}} F_{drag}(\mathbf{I}(\boldsymbol{\theta}), \boldsymbol{\theta}) \\ \text{Subject to:} \quad & F_{lift}(\mathbf{I}(\boldsymbol{\theta}), \boldsymbol{\theta}) \geq F_{lift,\text{min}} \\ & \theta_{\text{low}} \leq \boldsymbol{\theta} \leq \theta_{\text{high}} \end{aligned}$$

where:

- $\boldsymbol{\theta}$ represents the vector of design variables, which is bounded by θ_{low} and θ_{high}.
- $F_{drag}(\mathbf{I}(\boldsymbol{\theta}), \boldsymbol{\theta})$ is the objective function, representing the drag force, which is a function of both the state variable $\mathbf{I}(\boldsymbol{\theta})$, obtained from Eq. 5.8, and the design variables $\boldsymbol{\theta}$.
- $F_{lift}(\mathbf{I}(\boldsymbol{\theta}), \boldsymbol{\theta})$ represents the lift force, which serves as a constraint to ensure that the lift force remains above a minimum threshold $F_{lift,\text{min}}$.

The design variables in this context correspond to the material density of each element within the discretized mesh of the design domain. Referring to the N_{col} and N_{rows} parameters defined in Section 5.2, the mesh consists of $N_e = (N_{\text{col}} + 1) \times (N_{\text{rows}} + 1)$ elements, each associated with a density value θ_i. These density values, which range between $\theta_{\text{low}} = 0$ and $\theta_{\text{high}} = 1$, determine the material distribution within the design domain.

The iterative optimization process starts with an initial guess for the design variables $\boldsymbol{\theta}$, which are progressively updated to minimize the drag force F_{drag} while adhering to the lift force constraint. The initial design variables can be chosen and varied. The choice of the initial design may impact the final topologies obtained.

6.2.2 Material Interpolation Schemes

The MIS plays a crucial role in topology optimization by defining how material properties vary within the design domain as a function of the design variables. In this study, three MIS approaches were considered: the SIMP or power-law approach, the RAMP, and a linear interpolation scheme. These approaches differ in how they interpolate material properties between void ($\theta = 0$) and solid ($\theta = 1$) states.

The property of interest in this study is the electrical resistivity ρ of the material within each mesh element. As discussed in Section 5.3, the model has been relaxed to allow for the modification of the electrical resistivity of each element in the mesh. Thus, the interpolated property $\rho_i(\theta_i)$ is the electrical resistivity corresponding to the material density θ_i of a mesh element i.

Linear Interpolation Scheme

The linear interpolation scheme is the simplest of the three methods, providing a straightforward relationship between the material density θ and the material resistivity ρ. The resistivity at any mesh element in the design domain is given by:

$$\rho_i(\theta_i) = \rho_{max} + (\rho_{min} - \rho_{max}) \cdot \theta_i \quad \text{for } i = 1, \ldots, N_e$$

where:

- $\rho_{min} = \frac{1}{3.5 \times 10^7}\,\Omega\,\text{m}$ represents the resistivity of the material in its fully conductive state.
- $\rho_{max} = 60 \times \rho_{min}$ is the resistivity corresponding to the material's void state with $K = 60$, the increase factor of the initial resistivity chosen in accordance with Section 5.3.

SIMP or Power-Law Approach

The SIMP method introduces a non-linear relationship between the material density and resistivity. The resistivity is interpolated as:

$$\rho_i(\theta_i) = \rho_{max} + (\rho_{min} - \rho_{max}) \cdot \theta_i^n \quad \text{for } i = 1, \ldots, N_e$$

where n is the penalty factor.

RAMP Approach

The RAMP interpolation scheme offers an alternative approach, where the resistivity is given by:

$$\rho_i(\theta_i) = \rho_{max} + \frac{(\rho_{min} - \rho_{max}) \cdot \theta_i}{1 + q(1 - \theta_i)}$$

Here, q serves as the penalty factor.

Results and Comparison of MIS Approaches

It was observed that the final topologies obtained using the different MIS approaches were highly similar, with the designs converging close to a binary 0-1 solution even with the non-penalized linear approach. Given the faster convergence rates and the simplicity associated with the linear interpolation, it was selected as the default MIS for subsequent optimization results.

6.2.3 Adaptation of the Adjoint Variable Method to the PM-EDS Problem

The AVM was adapted to the specific needs of this study to efficiently compute the gradients of the objective function (drag force) and the constraint (lift force) with respect to the design variables $\boldsymbol{\theta}$.

The governing state equation for the system is given by (see Eq. 5.8):

$$\mathbf{A}(\boldsymbol{\theta})\mathbf{I} = \mathbf{B}$$

where $\mathbf{A}(\boldsymbol{\theta})$ represents the system matrix, which depends on the design variables and encapsulates the resistive and inductive components, $\mathbf{I}$ denotes the state variable, consisting of the vector of unknown induced currents, and $\mathbf{B}$ is the known right-hand side vector with the induced voltages, as detailed in Section 5.2.

Referring to Eq. 6.9 developed in the state of the art on TO (Subsection 6.1.3), the AVM for this study can be expressed in the following form:

$$\frac{dF_{drag}}{d\boldsymbol{\theta}} = \frac{\partial F_{drag}}{\partial \boldsymbol{\theta}} + \boldsymbol{\lambda}^T \frac{\partial \mathbf{A}(\boldsymbol{\theta})}{\partial \boldsymbol{\theta}} \mathbf{I}$$

Given that the drag force F_{drag} has no explicit dependency on the material density, but rather an implicit one through the induced currents, it can be expressed as:

$$\frac{dF_{drag}}{d\boldsymbol{\theta}} = \boldsymbol{\lambda}^T \frac{\partial \mathbf{A}(\boldsymbol{\theta})}{\partial \boldsymbol{\theta}} \mathbf{I}$$

Fig. 6.3 presents the computed gradients of the drag, lift, and LDR on the conductive track, evaluated over a domain of size $\tau_c = 2\tau_m = 0.4$ m with a track width of 0.4 m.

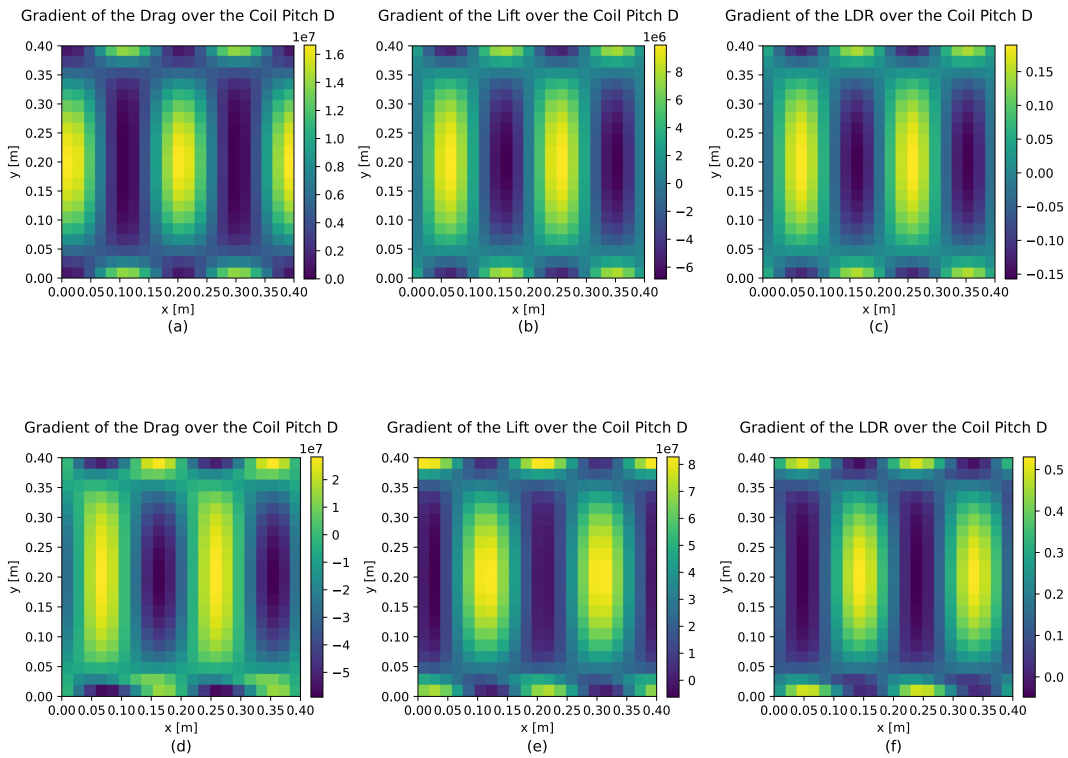

Figure 6.3: Gradient plots showing the gradient of the Drag, Lift, and LDR over the Coil Pitch τ_c for two different speeds: (a, b, c) Low speed ($v_x = 1.15$ m/s) and (d, e, f) Higher speed ($v_x = 18$ m/s).

Employing these gradients in the topology optimization process could introduce a bias in the resulting topologies. The presence of holes in the track causes the induced currents and the associated electromagnetic forces to vary with the position of the PM array above the track.

As the PM array moves over the conductive sheet, eddy currents are induced. In a uniform, unperforated sheet, these currents form consistent patterns, leading to stable electromagnetic forces. However, the introduction of holes disrupts these current paths, resulting in irregular distributions of induced currents and hence lead to fluctuations in the electromagnetic forces. Due to the periodic nature of the magnetic field, these force fluctuations exhibit a periodic behavior with a period matching the pole pitch τ_m of the PM array.

To obtain representative values for the drag and lift forces, it is essential to evaluate the forces at multiple positions of the PM array, spanning one pole pitch τ_m. Averaging the forces across these positions provide a value that more accurately reflects the overall performances of the system, rather than one dependent on the specific relative position of the PM array and that would lead to topologies optimized only for a specific position of the array.

6.2.4 Mitigation of Bias Through Averaged Forces

To address this bias, the forces were computed for multiple shifted positions of the PMs array within a pole pitch distance τ_m. The objective function was then redefined as the average of these forces, ensuring that the optimization results were robust to the relative position of the PMs array.

- **Averaged Drag Force**: The averaged drag force $\overline{F_d}$ is computed as:

$$\overline{F_{drag}} = \frac{1}{N_s}\sum_{i=1}^{N_s} F_{drag}(\mathbf{I}(\boldsymbol{\theta}, x_i), \boldsymbol{\theta})$$

  where x_i represents the shift position of the PMs array, and N_s is the total number of shift positions considered.

- **Averaged Lift Force**: Similarly, the averaged lift force $\overline{F_l}$ is computed as:

$$\overline{F_{lift}} = \frac{1}{N_s}\sum_{i=1}^{N_s} F_{lift}(\mathbf{I}(\boldsymbol{\theta}, x_i), \boldsymbol{\theta})$$

The sensitivities of the averaged drag and lift forces were calculated and are illustrated in Fig. 6.4.

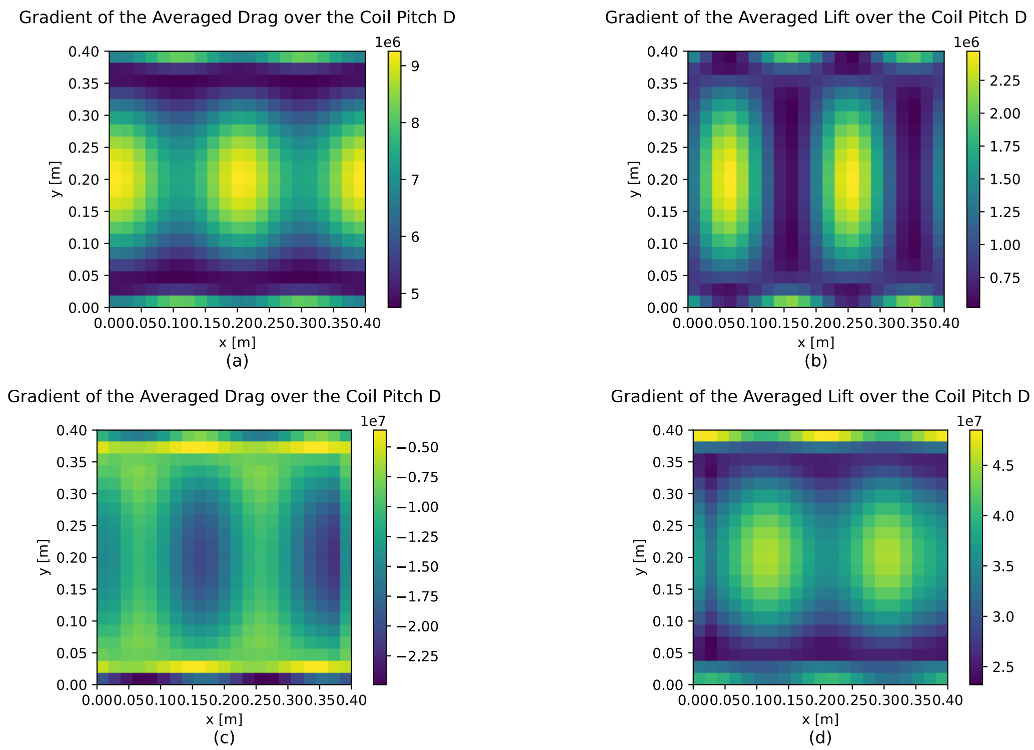

Figure 6.4: Gradient plots showing the gradient of the averaged Drag and Lift, over the Coil Pitch τ_c for two different speeds: (a, b) Low speed ($v_x = 1.15$ m/s) and (c, d) Higher speed ($v_x = 18$ m/s).

Chapter 7

Results and Discussion

In this chapter, the results of the density-based TO algorithm are presented and analyzed. The discussion begins with an overview of the reference model, which serves as a benchmark for assessing the performance of the optimized topologies. The first set of results focuses on optimizing topologies to enhance system efficiency and performance by maximizing the LDR. Following this, a second optimization is conducted with the goal of minimizing material usage. The resulting topologies from both optimizations are evaluated, leading to a discussion on intuitive design configurations.

7.1 Reference Topology and Velocity Influence

The full conductive sheet was used as a reference benchmark to evaluate the performance of the obtained topologies. This reference case represents the maximum achievable lift at any given speed, as the full conductive sheet offers the largest surface area for current induction. However, the associated drag with a full conductive sheet is also relatively high, which may not yield the optimal LDR.

The performance of the optimized topologies was evaluated by comparing their LDR with that of the full conductive sheet. This comparison determines whether the new designs offer substantial efficiency improvements. The lift constraints in the subsequent results correspond to a % of the obtained lift at a given speed v_x, using the reference topology. Fig. 7.1 illustrates the LDR values across a range of velocities for the FEM reference model and the advanced plate model, using two different discretization sizes: $\Delta x = \Delta y = 1$ cm and 2 cm.

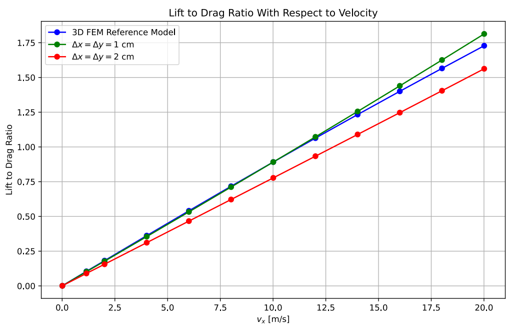

Figure 7.1: Comparison of Lift-to-Drag Ratio Across Velocities for Different Discretization Sizes

The vehicle's speed is a critical parameter in topology optimization, given the velocity-dependent nature of current distribution (e.g., skin effect, diffusion angle) and the associated electromagnetic forces. These dependencies suggest that the optimal topologies will differ depending on the velocity considered. This is further evidenced by the changing gradients with increasing speed, as shown in Figures 6.3 and 6.4.

Therefore, in this study, multiple velocities were considered in the topology optimization process to capture the full spectrum of system behavior. This approach could allow the design of a track system optimized for a given speed profile of a MAGLEV vehicle.

The initial TO conducted in this study, as outlined in Section 6.2, aimed to minimize the objective function—the average drag force—while constraining the average lift to a specified percentage of the lift achieved with the full conductive sheet at a given velocity.

7.2 First Topology Optimization: Performance Optimization

The results are presented in Fig. 7.2. The lift constraint was systematically varied from 10% to 100% of the lift produced by the full conductive sheet at the corresponding speed. Each data point in the figure represents a feasible design solution that meets the required lift performance criteria. The optimization process was initiated with a uniform material distribution ($\theta = \text{const.} = 0.5$) across the design domain, reflecting an initial assumption of homogeneity. The discretization used was limited to $\Delta x = \Delta y = 2$ cm, avoiding excessively time-consuming calculations.

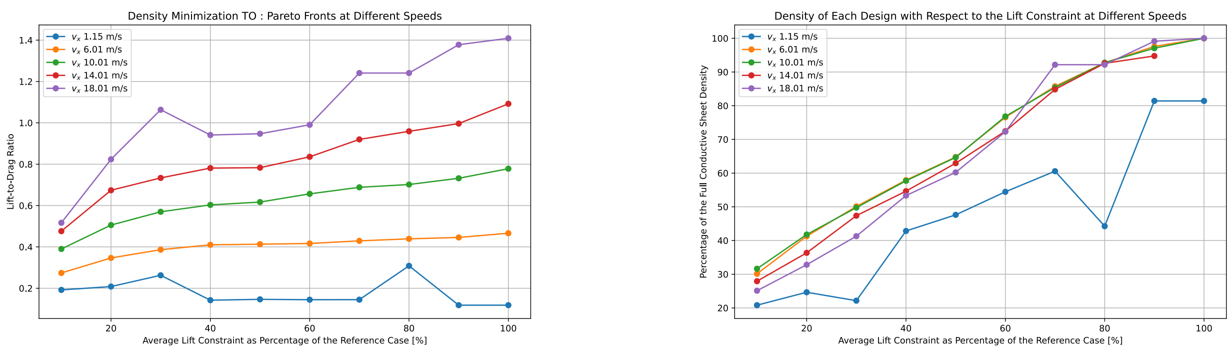

(a) Lift-to-drag ratio across various velocities and lift constraints.

(b) Material density corresponding to each optimized design.

Figure 7.2: Results of the topology optimization algorithm for different velocities and lift constraints. The left plot shows the Pareto fronts, while the right plot illustrates material density for every design obtained.

The plots provide insights into the behavior of the TO under different velocities. It is evident that as the lift constraint is relaxed, the optimization algorithm progressively removes material to reduce drag. However, this approach results in a disproportionate reduction in lift, leading to a lower LDR. This outcome indicates that the optimization process may be prone to local optima, where the strategy of material removal for drag minimization inadvertently leads to suboptimal designs.

Across all velocities, the full conductive sheet, serving as the benchmark, appears to offer the best performance in terms of LDR. However, it is essential to recognize that depending on the application, a slightly lower LDR with an associated reduction in material usage can be acceptable, provided that sufficient lift is maintained for the system's operation. Therefore, even though the full conductive sheet topology yields the highest LDR, the other obtained topologies may still be of interest.

7.2.1 Representative Topologies from Drag Force Minimization

For further analysis, several specific topologies have been selected to gain a deeper understanding of the behavior of the TO algorithm for different velocity range and changes in the average lift constraint (see Fig. 7.2). For each range of speed:

- **High-Speed Topologies:** Fig. 7.3 presents three designs obtained at high speed ($v_x = 18$ m/s) for varying values of the average lift constraint. The corresponding average LDR and the material density, expressed as a percentage relative to the full conductive sheet, are detailed in Table 7.1.

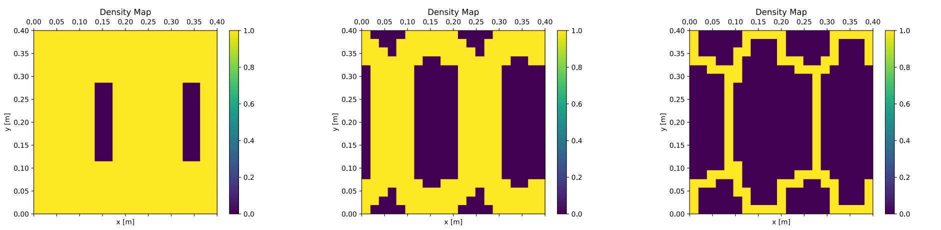

(a) 80% lift constraint (b) 50% lift constraint (c) 10% lift constraint

Figure 7.3: Designs at different lift constraints for high-speed ($v_x = 18$ m/s) range.

Design Constraint	LDR	Density (%)	LDR Decrease (%)
Full Plate Reference	1.41	100%	-
80% Design	1.24	91.83%	12.06055%
50% Design	0.947	59.41%	32.83997%
10% Design	0.517	23.58%	63.33008%

Table 7.1: Comparative analysis of high-speed range designs.

The topology shown in Fig. 7.3a, which achieved the highest LDR, closely resemble the full conductive sheet with strategic material removal in areas that reduce drag force, thereby lowering the track density by nearly 10%. However, as previously discussed, relaxing the lift constraint generally results in a reduction in average drag at the cost of a more significant decrease in lift, leading to a 12% decrease in the LDR. Despite this, the specific regions where material is removed offer valuable insights into potentially advantageous topologies. As the lift constraint is relaxed, as shown in Fig. 7.3b and Fig. 7.3c, the algorithm tends to remove material in regions that most significantly impact average drag. This results in coils-like designs, with decreasing widths as the lift constraint is progressively relaxed.

- **Intermediate-Speed Topologies:** Fig. 7.4 displays designs obtained at an intermediate velocity ($v_x = 6$ m/s) under the same lift constraints applied in the high-speed case. The corresponding performance parameters for these designs are detailed in Table 7.2.

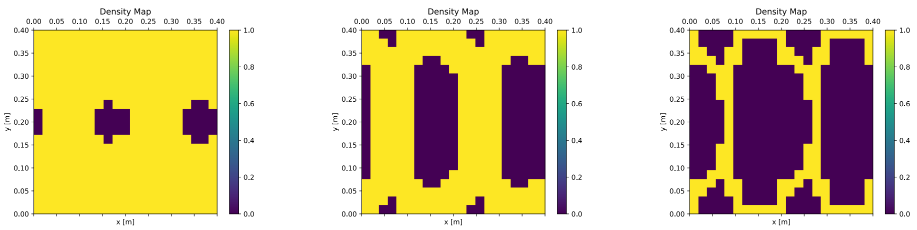

(a) 80% lift constraint (b) 50% lift constraint (c) 10% lift constraint

Figure 7.4: Designs at different lift constraints for intermediate-speed ($v_x = 6$ m/s) range.

Design Constraint	LDR	Density (%)	LDR Decrease (%)
Full Plate Reference	0.466	100%	-
80% Design	0.439	92.51%	5.79529%
50% Design	0.413	63.49%	11.37543%
10% Design	0.274	27.66%	41.20178%

Table 7.2: Comparative analysis of intermediate-speed range designs.

A similar analysis to that conducted for the high-speed case can be applied to these results. The designs exhibit comparable patterns in the areas where material is removed as the lift threshold is decreased.

- **Low-Speed Topologies:** In contrast, at lower speeds, some topologies with moderate material removal achieved slightly improved LDR compared to the full sheet reference case. Fig. 7.5 presents noteworthy designs obtained at $v_x = 1.15$ m/s, with the corresponding performance parameters detailed in Table 7.3.

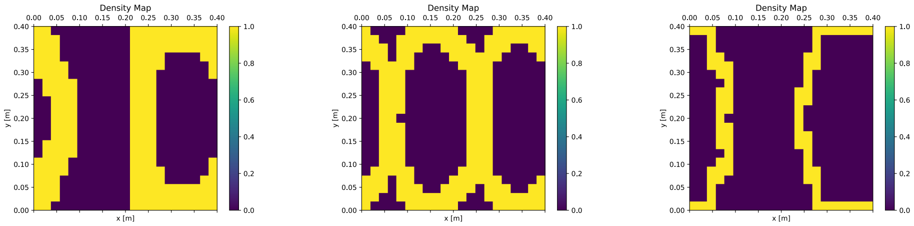

(a) 80% lift constraint (b) 50% lift constraint (c) 30% lift constraint

Figure 7.5: Topology designs at different lift constraints for low-speed ($v_x = 1.15$ m/s) range.

Design Constraint	LDR	Density (%)	LDR Increase (%)
Full Plate Reference	0.1	100%	-
80% Design	0.3	42.17%	200.00305%
50% Design	0.146	44.67%	45.9961%
30% Design	0.262	18.14%	161.99341%

Table 7.3: Comparative analysis of low-speed range designs.

These results suggest that at lower speeds, there is greater flexibility in material distribution, enabling some drag reduction without significantly compromising lift. As shown in Fig. 7.5a and Fig. 7.5c, the material density is considerably reduced, and the LDR outperforms the reference. Notably, Fig. 7.5a depicts a configuration similar to the simple discrete loop discussed in Subsection 2.1.2. Although low-speed designs may not be critical for long-term operational efficiency, discovering new topologies at such speeds remains valuable. Identifying innovative designs that enable higher lift at lower speeds could lead to systems achieving levitation more rapidly, thereby reducing the propulsion requirements at lower speeds and lowering the transition speed v_t defined in Subsection 2.1.2.

The impact of vehicle velocity on the optimized designs highlights the importance of accounting for a range of operating conditions during the optimization process. A discernible trend in hole configurations seems to emerge from intermediate to high velocities.

As discussed in Chapter 2, a trade-off is often sought between long-term efficiency, represented by the LDR, and initial cost, production cost, depending on the specific application. The initial optimization focused on maximizing efficiency through the LDR. The subsequent TO will shift focus toward optimizing material usage.

7.3 Second Topology Optimization: Material Usage Optimization

The material minimization problem is formulated similarly to the drag minimization problem, starting with the same initial assumption of a uniform material distribution across the design domain (i.e., $\theta = \text{const.} = 0.5$). However, in this case, the objective function is defined as the total material density in the track. The optimization process aims to minimize this objective while ensuring that the lift constraint is satisfied.

$$
\begin{aligned}
\text{Objective:} \quad & \min_{\boldsymbol{\theta}} \sum_{i=1}^{N_e} \theta_i \\
\text{Subject to:} \quad & F_{lift}(\mathbf{I}(\boldsymbol{\theta}), \boldsymbol{\theta}) \geq F_{lift,\min} \\
& 0 \leq \boldsymbol{\theta} \leq 1
\end{aligned}
$$

where:

- $\sum_{i=1}^{N_e} \theta_i$ represents the total material usage across all elements in the design domain.
- $F_{lift}(\mathbf{I}(\boldsymbol{\theta}), \boldsymbol{\theta})$ remains the lift force, constraint to at least a value of $F_{lift,\min}$ ensuring that sufficient lift is generated despite the reduced material.

The results of the material minimization optimization are illustrated in Fig. 7.6. The results exhibit a behavior similar to the previous test.

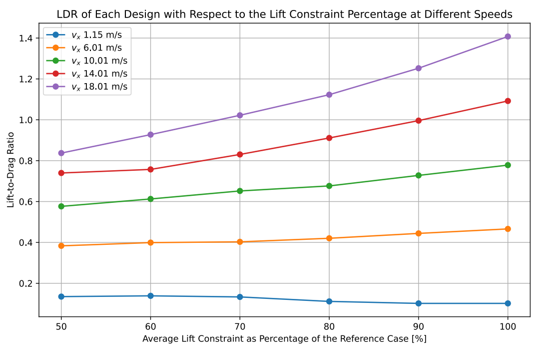

(a) Lift-to-drag ratio across various velocities and lift constraints for the material usage optimization.

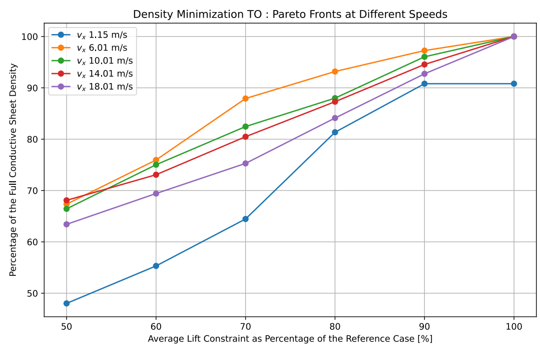

(b) Material density distribution corresponding to each optimized design for the material usage optimization.

Figure 7.6: Results of the density minimization-based TO for different velocities and lift constraints. The left plot illustrates the Pareto fronts in terms of lift-to-drag ratio, while the right plot depicts the material density for each optimized design.

Indeed, when the lift constraint is set near the maximum lift achievable with a full sheet, the optimization yields designs that are relatively conservative in terms of material removal. However, as the lift constraint is relaxed, similar to the first optimization results, the algorithm begins to aggressively reduce material, leading to a significant decrease in lift and, consequently, a reduction in the LDR until the minimum lift requirement is met. This observed tendency of the algorithm to "strip away" material until only the minimum lift is maintained underscores the potential challenge of local optima.

However, with the objective of minimizing the total density of the rail, the resulting holes in the track are generally placed in less strategical areas compared to the first TO, where holes were strategically placed in specific regions to minimize drag force. In this case, the algorithm focuses solely on reducing density until the lift force approaches the minimum acceptable level. For certain lift constraints, the algorithm can become trapped in local optima, resulting in designs characterized by sparse distributions of conductive material, often concentrated in narrow strips. These designs may suffer from reduced structural integrity, posing significant risks to the overall stability and functionality of the track.

7.3.1 Representative Topologies from Material Minimization

Several representative topologies resulting from the material minimization optimization are presented below, corresponding to different velocity regions:

- **High-Speed Topologies:** Figure 7.7 presents designs obtained at a speed of $v_x = 18$ m/s for varying lift constraints. The corresponding parameters obtained are detailed in Table 7.4.

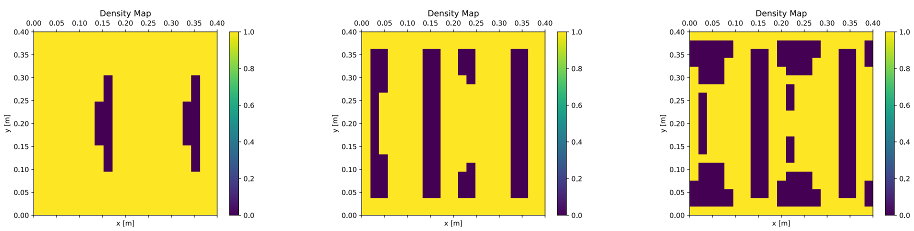

(a) 90% lift constraint (b) 70% lift constraint (c) 50% lift constraint

Figure 7.7: Designs at different lift constraints for high-speed ($v_x = 18$ m/s) range.

Design Constraint	LDR	Density (%)	LDR Decrease (%)
Full Plate Reference	1.41	100%	-
90% Design	1.25	92.74%	11.34949%
70% Design	1.02	75.28%	27.6596%
50% Design	0.837	63.49%	40.64026%

Table 7.4: Comparative analysis of high-speed range designs.

The material removal appears hazardous for most lift constraints at high speed, as the optimization aggressively removes material until the lift threshold is barely met. As observed in Fig. 7.7a, material is removed in regions similar to those in Fig. 7.3a. This suggests that these areas are optimal for material removal and allow for significant reductions in drag force. However, as the lift constraint is further relaxed, the resulting designs deviate significantly from previous TO outcomes and seem to represent local optima. For instance, Fig. 7.7c does not exhibit a lower density than Fig. 7.3b, for the same constraint despite the latter achieving a better LDR with a lower density, even though reducing total density was not the primary objective in that case.

- **Intermediate-Speed Topologies:** Fig. 7.8 shows the designs for $v_x = 6$ m/s for the same lift constraints with the associated Table 7.5.

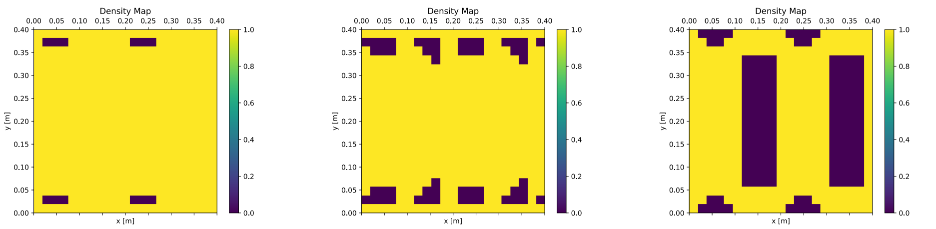

(a) 90% lift constraint (b) 70% lift constraint (c) 50% lift constraint

Figure 7.8: Designs at different lift constraints for intermediate-speed ($v_x = 6$ m/s) range.

Design Constraint	LDR	Density (%)	LDR Decrease (%)
Full Plate Reference	0.466	100%	-
90% Design	0.444	97.27%	4.7226%
70% Design	0.403	88.2%	13.52081%
50% Design	0.383	67.34%	17.81311%

Table 7.5: Comparative analysis of intermediate-speed range designs.

The same conclusions drawn from the high-speed case apply here as well. Although these results aim to minimize density specifically, a comparison with the first TO, where drag force was the objective function, reveals that for the same constraints, the track exhibits a higher density while achieving a lower LDR. Leading to designs that may not be worth considering. Additionally, Fig. 7.8c at this speed produces results that closely resemble those seen in Fig. 7.4b.

- **Low-Speed Topologies:** For the lower speed ($v_x = 1.15$ m/s), Fig. 7.9 shows specific designs obtained with the associated Table 7.6.

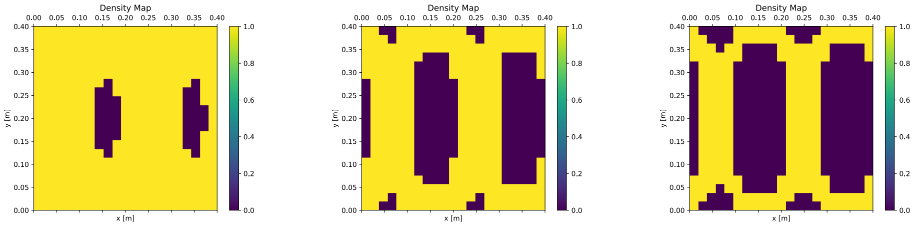

(a) 90% lift constraint (b) 70% lift constraint (c) 50% lift constraint

Figure 7.9: Topology designs at different lift constraints for low-speed ($v_x = 1.15$ m/s) applications range.

Design Constraint	LDR	Density (%)	LDR Increase (%)
Full Plate Reference	0.1	100%	-
90% Design	0.101	90.93%	0.99792%
70% Design	0.133	64.4%	32.9956%
50% Design	0.135	48.07%	34.9945%

Table 7.6: Comparative analysis of low-speed range topology designs.

At low speed, the designs are more consistent with the results obtained in the first TO. However, these designs still exhibit higher density for the same lift constraint and a lower LDR than the designs shown in Fig. 7.5.

The results obtained during this second TO, with the objective of minimizing the total density of the track, exhibit lower performances and higher densities compared to the designs generated in the first TO. Consequently, these results are less promising and may not warrant further investigation.

7.4 Intuitive Topologies: Exploring Alternatives to Standard Optimization

In this section, the focus shifts to an exploration of intuitive topologies at high speed $v_x = 18$ m/s, as this speed is the closest to the operational speed of the PM-EDS system and, therefore, has the most significant impact on operational efficiency. These topologies were selected based on insights derived from standard topology optimization results, as well as physical intuition regarding the system's behavior. The objective is to evaluate whether these intuitive designs can provide competitive or superior performance compared to the reference conductive sheet topology.

Three distinct intuitive designs were developed based on the prior TO results and the insights provided by the state of the art in Chapter 2. As discussed in Subsection 2.1.2, the ladder track, given specific geometric considerations, has the potential to achieve a higher LDR than the conductive plate track.

Intuitively, the optimized results should therefore converge toward a topology resembling a ladder configuration.

Therefore, topologies obtained for different lift constraints that exhibit design properties similar to the ladder track configuration are considered for further analysis.

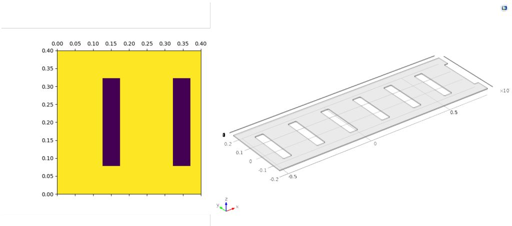

(a) Ladder-like topology.

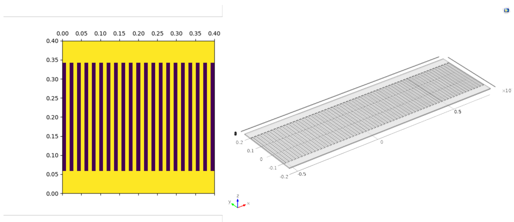

(b) Slitted plate design.

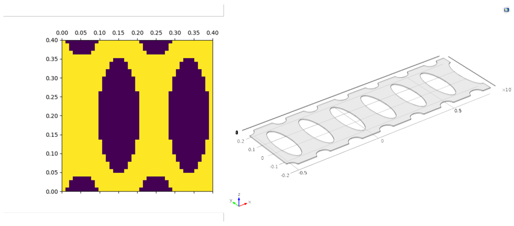

(c) Perforated sheet design with oval holes.

Figure 7.10: Comparison of intuitive topologies at high speed $v_x = 18$ m/s. Each design, inspired by insights from previous topology optimization results, offers different potential benefits.

7.4.1 Ladder-Like Topology

One of the intuitive topologies explored was a ladder-like structure, as shown in Fig. 7.10a. This design was inspired by the ladder track topology and the observation that the optimization process frequently initiated material removal in the same regions as the lift constraint was reduced. The results depicted in Fig. 7.3a, 7.4a, 7.7a, 7.9a served as the basis for this topology's development.

7.4.2 Slitted Plate Topology

The slitted plate design shown in Fig. 7.10b was intuitively selected to optimize performance by disrupting large eddy currents that typically result in energy losses through Joule heating. By introducing slits, the design aims to limit the formation of these currents, potentially reducing drag and improving the LDR ratio. Additionally, the slits strategically reduce material usage while still maintaining sufficient lift, making this design an effective compromise between performance and material efficiency.

7.4.3 Perforated Sheet with oval Holes Topology

Another intuitive topology investigated was a perforated sheet design, featuring a regular array of oval holes as depicted in Fig. 7.10c. This design was based on the observations made in earlier optimization results shown in Fig. 7.3b-c, 7.4b-c, 7.5b, 7.8c, 7.9b-c.

7.4.4 Performance Analysis

The intuitive topologies described above were evaluated against results obtained from a detailed 3D FEM model implemented in *Comsol Multiphysics®*. The objective was to validate the effectiveness of the simplified analytical models used in this study and to assess the performance of these intuitive topologies. The results of the comparison are presented in Fig. 7.11 and Table 7.7. A comparison of the induced current patterns can be found in Appendix B.

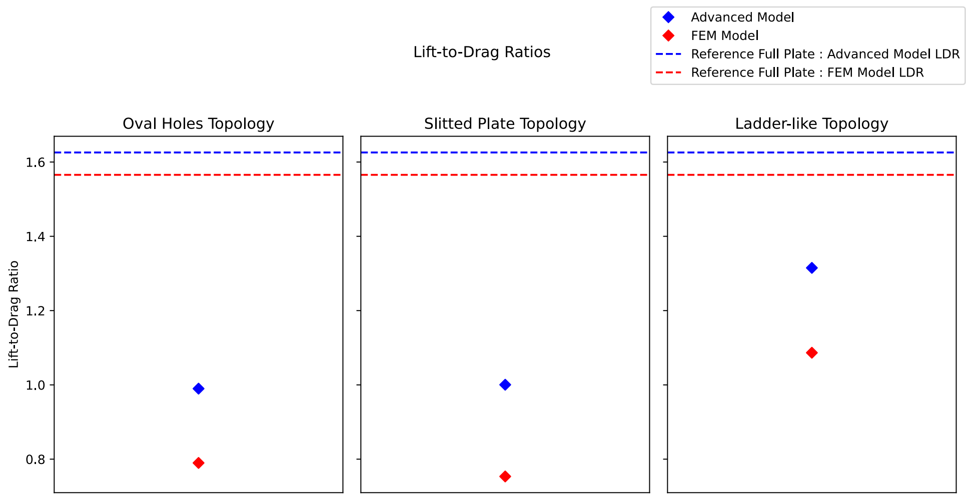

Figure 7.11: Comparison of Lift-to-Drag Ratios for different intuitive topologies. The blue markers represent the advanced model, and the red markers represent the FEM model. Dashed lines indicate the reference LDR of the full plate obtained from both models.

Topology	Density (%)	LDR Deviation (%)	Lift Deviation (%)	Drag Deviation (%)
Oval Holes	61.33	25.33	10.74	11.64
Ladder-like	85.13	21.03	16.05	4.12
Slitted Plate	63.77	32.77	32.96	0.14

Table 7.7: Deviation in Performance Metrics and Material Density for Intuitive Topologies Compared to FEM Results

Based on those results, the LDR deviation relative to the FEM model, and the total density of the designs, the most promising topology appears to be the ladder-like structure. This design offers a favorable balance between efficiency and material usage, achieving a relatively high LDR while enabling material reduction in the track.

These results could potentially be further improved through shape optimization of the different topologies. It is important to recognize that these topologies do not represent the optimal design. Rather, they are configurations of tracks that, based on physical intuition, system behavior, and previous optimization results, are likely to offer a favorable trade-off between performance and cost. As such, they may be wiser choices for certain types of applications.

7.4.5 Leveraging Intuitive Topologies as Initial Guesses in Optimization

The exploration of intuitive topologies was also motivated by the limitations observed in the standard topology optimization process, where the optimization frequently became trapped in local optima. This limitation resulted in designs that, while functional, were not necessarily the most innovative or efficient.

These topologies can serve as alternative starting points, guiding the optimization process toward promising regions of the design space that might otherwise remain unexplored through standard methods. Additionally, they can allow the optimization process to focus on enhancing the performance of the initial design. This approach has the potential to yield innovative designs that offer superior performance or efficiency.

While starting with these intuitive topologies offers advantages, it is important to recognize that this approach also carries the risk of biasing the optimization process toward certain design configurations. This bias may limit the exploration of other, potentially more effective designs. Additionally, these new starting points are heavily dependent on the availability and accuracy of the prior knowledge that inform them. In cases where such knowledge is limited or inaccurate, the resulting designs may be suboptimal.

Chapter 8

Future Work and Conclusion

The research presented here has advanced the understanding and application of topology optimization to the conductive tracks of Permanent Magnet Electrodynamic Suspension systems for MAGLEV trains. Central to this work is the development and validation of mathematical models that offer a robust framework for potentially simulating, discovering and optimizing new track topologies to enhance both performance and material efficiency.

The study began with the formulation of advanced analytical models based on equivalent electrical circuits, designed to capture the complex electromagnetic interactions within PM-EDS systems. The ladder track model served as the foundation, from which more sophisticated models, including the simplified and advanced plate models, were derived and rigorously validated against Finite Element Method simulations. These models have proven to be both accurate and efficient, confirming their applicability across various scenarios.

A key contribution of this research lies in the seamless integration of the advanced model with density-based TO methods. By adjusting resistivity within the model, the creation of holes and other topological variations within the conductive sheet was effectively simulated, enabling the exploration of innovative track designs.

Following the development of these models, the present study applied TO techniques to explore new conductive track configurations. The first optimization focused on performance, particularly the Lift-to-Drag ratio. The results highlighted the ability of certain topologies, such as ladder-like structures, to achieve high LDR while reducing material usage compared to conventional designs. However, the optimization process was often challenged by local optima, leading to suboptimal configurations.

A subsequent round of TO, aimed at material minimization, sought to reduce the initial cost and resource usage. However, this approach often resulted in topologies with lower performance metrics, including reduced LDR, indicating that material minimization alone may not yield the most effective designs.

The exploration of intuitive topologies, informed by TO results and prior knowledge, provided additional insights. These designs, such as the ladder-like topology, offered a promising compromise between performance and material efficiency and could potentially help in avoiding suboptimal solutions. However, the research also emphasized the potential biases introduced by relying on intuitive designs.

In conclusion, this research has laid a strong foundation for future work in the optimization of conductive tracks for EDS systems. The validated analytical models provide a reliable framework for further exploration, while the insights gained from the TO processes offer valuable guidance for the design of more efficient and cost-effective MAGLEV systems.

Future Work

Future work in this research could focus on enhancing the advanced plate model used for topology optimization of conductive tracks in PM-EDS systems. One area of improvement is the refinement of the inductance formulas, potentially developing new methods for computing equivalent inductances, which are critical to the model's accuracy. This could lead to better precision, especially for topologies with reduced material density.

Additionally, exploring alternative optimization strategies is essential. The density-based approach employed in this study often fell into local optima, limiting its effectiveness. Implementing techniques such as global optimization methods, multi-start approaches, or even transitioning to level-set methods could offer more robust and flexible optimization frameworks. These approaches might better capture the design complexities and lead to improved topologies.

Exploiting the observed periodicity in the optimized designs could also streamline the optimization process. By limiting the design domain to a smaller, periodic section, computational efficiency could be significantly enhanced, allowing for finer discretization and more accurate results.

In summary, future research should aim to refine the computational models, explore more advanced optimization techniques, and leverage design periodicity to improve both the efficiency and accuracy of topology optimization for PM-EDS system. These efforts would contribute to the development of more effective and cost-efficient solutions for high-speed rail technologies.

Appendix A

Validation of Inductance Formulas

In this study, it was necessary to compute the inductances and mutual inductances of rectangular conductors. The formulas utilized are derived from classical electromagnetic theory, specifically based on Neumann's formula for mutual inductance and the self-inductance calculations for rectangular conductors. The correctness of these formulas has been verified using a FEM model generated in *Comsol Multiphysics*®.

This model consists of a simple loop made of rectangular conductors inside which a current flows.

The total inductance of such a loop is given by:

$$L_{\text{tot}} = 2\left(L_V - M_V\right) + 2\left(L_H - M_H\right) \tag{A.1}$$

where L_V and L_H represent the self-inductance of a vertical conductor and a horizontal conductor, respectively. M_V and M_H denote the mutual inductance between the two vertical and the two horizontal conductors, respectively.

The validity of these formulas was tested by varying the shape of the conductors. These tests provided a better understanding of the validity region for our inductance computations.

In Fig. A.1, the conductors were taken with a squared cross-section. The size of this cross-section was then varied, providing insights into the required discretization for our model.

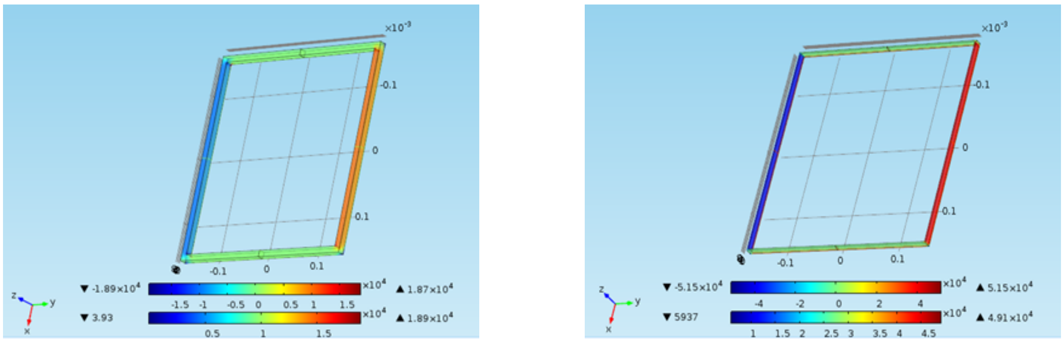

(a) (b)

Figure A.1

Figure	Comsol	Model	Deviation [%]
(a)	8.6049×10^{-7} [H]	8.9592×10^{-7} [H]	3.95
(b)	1.0063×10^{-6} [H]	1.0173×10^{-6} [H]	1.08

Table A.1: Deviations observed on the value of the inductance between *Comsol Multiphysics®* and the FEM model, while varying the cross-section.

Reducing the cross-section provides better results in terms of the inductance's value between *Comsol Multiphysics®* and the FEM model, as the deviation decreases.

In Fig. A.2, the thickness of the conductor was fixed at $1cm$. This test aimed to demonstrate the importance of maintaining a cross-section close to a square shape with a width equal to the thickness.

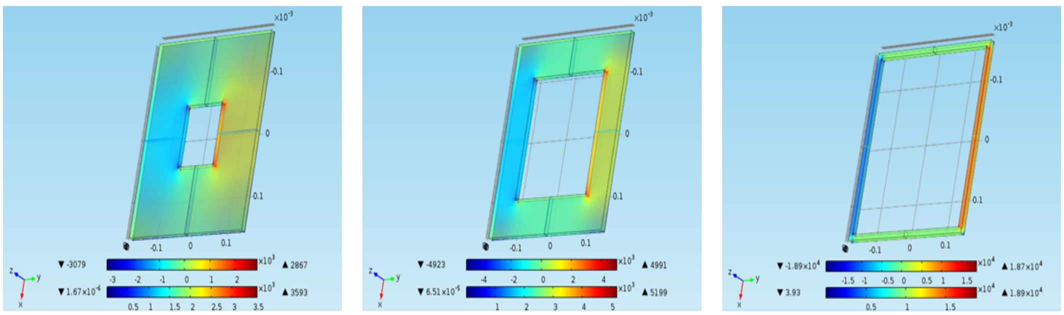

(a) (b) (c)

Figure A.2

As observed thanks to the Table A.2, getting closer to a square shape while keeping the width equal to the thickness, drastically reduces the deviations,

Figure	Comsol	Model	Deviation [%]
(a)	1.9357×10^{-7} [H]	4.0824×10^{-7} [H]	52.58
(b)	4.1664×10^{-7} [H]	5.6597×10^{-7} [H]	26.38
(c)	8.6049×10^{-7} [H]	8.9592×10^{-7} [H]	3.95

Table A.2: Deviations observed on the value of the inductance between *Comsol Multiphysics®* and the FEM model, while keeping a constant thickness and varying the shape.

going from 52.58% to 3.95%.

The final test aimed to show the impact of the length of the conductors while maintaining a squared cross-section. The results of this test are depicted in Fig. A.3.

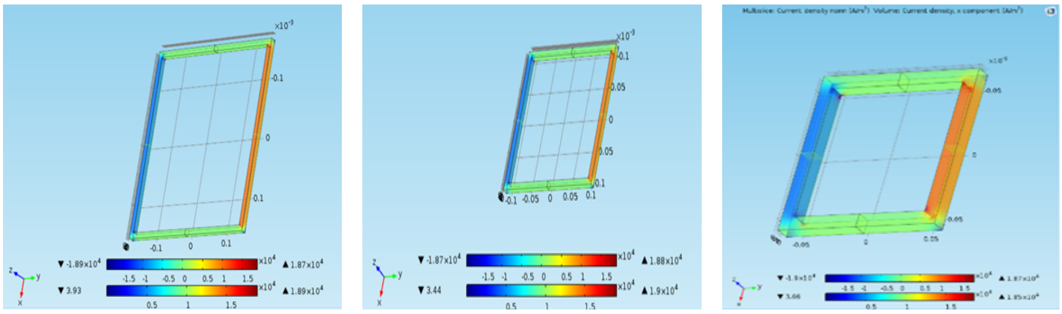

(a) (b) (c)

Figure A.3

Figure	Comsol	Model	Deviation [%]
(a)	8.6049×10^{-7} [H]	8.9592×10^{-7} [H]	3.95
(b)	5.1815×10^{-7} [H]	5.5017×10^{-7} [H]	5.82
(c)	2.1532×10^{-7} [H]	2.4206×10^{-7} [H]	11.05

Table A.3: Deviations observed on the value of the inductance between *Comsol Multiphysics®* and the FEM model, while varying the length of the conductors.

Reducing the length of the conductors shows bad impact on the inductance's value, as the deviation keeps increasing between *Comsol Multiphysics®* and the FEM model.

Based on these results, the mutual inductances and therefore the equivalent inductances L_{Veq} and L_{Heq} in the ladder model were computed using the formulas verified in this section when the distance between two conductors is small. For larger distances, the conductors can be considered as infinitely thin cylindrical wires. Consequently, the mutual inductances at larger distances are computed using the formulas developed by Dumont de Chassart et al. [91],[92], which provide the mutual inductance values between two parallel wires.

Following a thorough analysis and validation of the models employed in this study, it was determined that the Dumont formula should be utilized, even for short distances. The application of the previously validated formulas consistently resulted in greater deviations and less accurate outcomes when compared to the FEM models developed in this research. Specifically, the use of these formulas in computing the equivalent inductances led to erroneous results. The formula being extremely sensible to changes in the cross-section, length, size of the discrete conductors considered in this study.

Consequently, the Dumont formula was chosen for this study, and it is recommended that further investigation be conducted to either refine the existing formula or develop a new one tailored to future research employing the developed analytical models potentially leading to even more accurate results.

Appendix B

Intuitive Topologies: Induced Current Patterns Comparisons

Presented below are the induced current densities in both the y and x directions for the intuitive new track topologies developed in Section 7.4. In each figure, the top graphs depict the transverse current density, J_y, while the bottom graphs show the longitudinal current density, J_x. The left plots are derived from the advanced plate analytical model, whereas the right plots are obtained from the 3D FEM model (see Fig. 4.6).

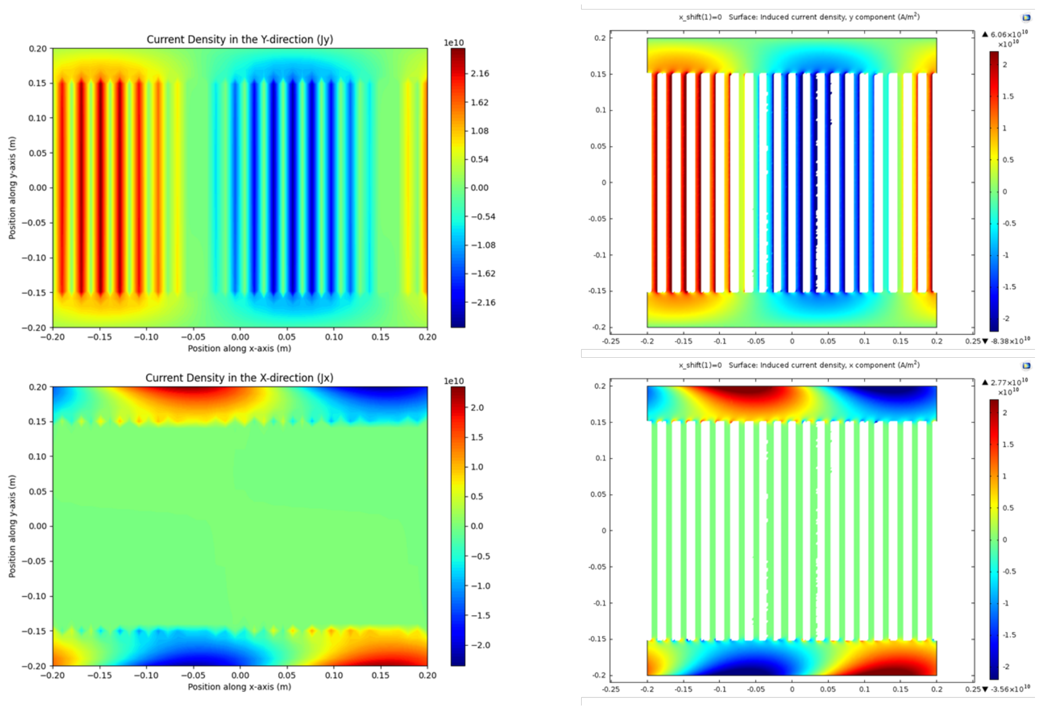

Figure B.1

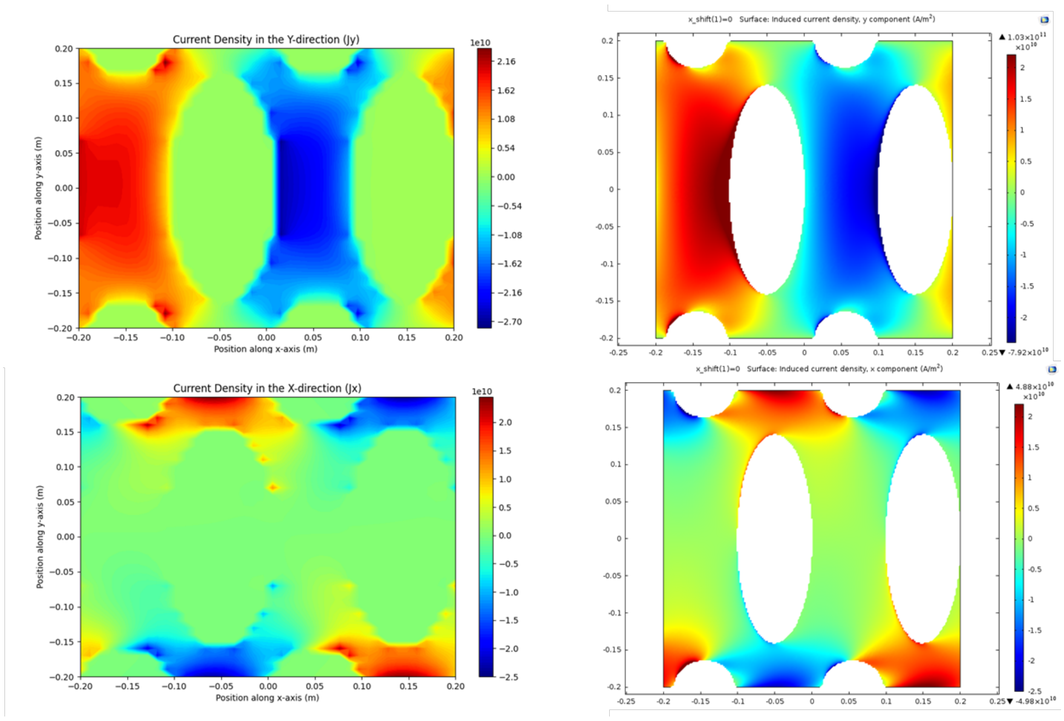

Figure B.2

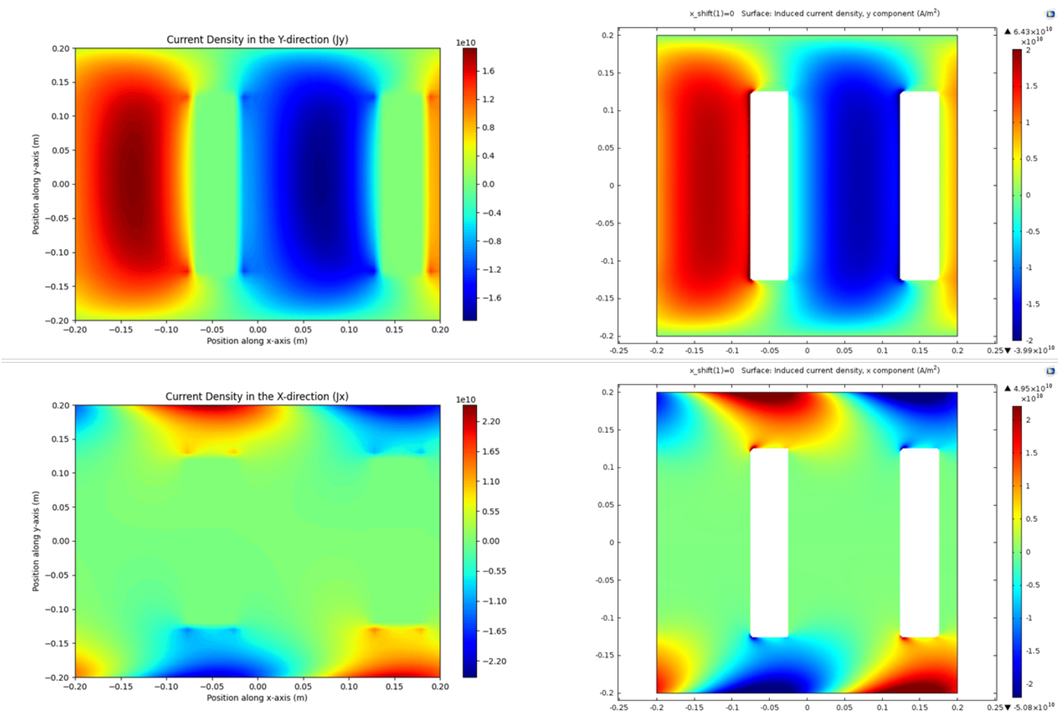

Figure B.3

Bibliography

[1] Z. Qadir, A. Munir, T. Ashfaq, H. S. Munawar, M. A. Khan, and K. Le, "A prototype of an energy-efficient maglev train: A step towards cleaner train transport," *Cleaner Engineering and Technology*, vol. 4, p. 100217, 2021.

[2] N. Paudel, *Dynamic suspension modeling of an eddy-current device: An application to MAGLEV*. PhD thesis, The University of North Carolina at Charlotte, 2012.

[3] K. Sawada, M. Murai, and M. Tanaka, "Magnetic levitation (maglev) technologies," *Japan Railway & Transport Review*, vol. 25, pp. 58–67, 2000.

[4] M. Kim, J.-H. Jeong, J. Lim, C.-H. Kim, and M. Won, "Design and control of levitation and guidance systems for a semi-high-speed maglev train," *Journal of Electrical Engineering and Technology*, vol. 12, no. 1, pp. 117–125, 2017.

[5] C. Ham, W. Ko, K.-C. Lin, and Y. Joo, "Study of a hybrid magnet array for an electrodynamic maglev control," *Journal of Magnetics*, vol. 18, no. 3, pp. 370–374, 2013.

[6] L. Beauloye and B. Dehez, "Permanent magnet electrodynamic suspensions applied to maglev transportation systems: A review," *IEEE Transactions on Transportation Electrification*, vol. 9, no. 1, pp. 748–758, 2022.

[7] J. Lim, C.-Y. Lee, J.-H. Lee, W. You, K.-S. Lee, and S. Choi, "Design model of null-flux coil electrodynamic suspension for the hyperloop," *Energies*, vol. 13, no. 19, p. 5075, 2020.

[8] Y. J. Chen and J. Feng, "Optimization of guideway coil dimensions for a magnetic levitation system," *IEEE Transactions on Magnetics*, vol. 33, no. 5, pp. 4335–4344, 1997.

[9] O. F. Storset and B. E. Paden, "Electrodynamic magnetic levitation with discrete track part ii: Periodic track model for numerical simulation and lumped parameter model," *IEEE Transactions on Magnetics*, 2005.

[10] L. Beauloye and B. Dehez, "Comparison of track topologies of permanent magnet electrodynamic suspensions," in *2023 14th International Symposium on Linear Drivers for Industry Applications (LDIA)*, pp. 1–5, IEEE, 2023.

[11] Y. Cai, G. Ma, Y. Wang, T. Gong, K. Liu, C. Yao, W. Yang, and J. Zeng, "Semianalytical calculation of superconducting electrodynamic suspension train using figure-eight-shaped ground coil," *IEEE Transactions on Applied Superconductivity*, vol. 30, no. 5, pp. 1–9, 2020.

[12] J. Bird and T. Lipo, "The experimental verification of the lift, thrust and guidance forces created by an electrodynamic wheel rotating over a split-sheet guideway," in *Maglev*, pp. 1–9, 2006.

[13] COMSOL®, "Electrodynamic wheel (edw) magnetic levitation using comsol multiphysics®." Presentation slides, not mentioned. Accessed on: 23 July 2023.

[14] S. Sanogo, F. Messine, C. Henaux, and R. Vilamot, "Topology optimization for magnetic circuits dedicated to electric propulsion," *IEEE transactions on magnetics*, vol. 50, no. 12, pp. 1–13, 2014.

[15] N. P. Van Dijk, K. Maute, M. Langelaar, and F. Van Keulen, "Level-set methods for structural topology optimization: a review," *Structural and Multidisciplinary Optimization*, vol. 48, pp. 437–472, 2013.

[16] H.-W. Lee, K.-C. Kim, and J. Lee, "Review of maglev train technologies," *IEEE transactions on magnetics*, vol. 42, no. 7, pp. 1917–1925, 2006.

[17] F. Li, Y. Sun, J. Xu, Z. He, and G. Lin, "Control methods for levitation system of ems-type maglev vehicles: An overview," *Energies*, vol. 16, no. 7, p. 2995, 2023.

[18] T. D. F. Cabral and F. R. Chavarette, "Dynamics and control design via lqr and sdre methods for a maglev system," *International Journal of Pure and Applied Mathematics*, vol. 101, no. 2, pp. 289–300, 2015.

[19] R. Ahmed, Y. L. Jun, M. F. Azhar, and N. U. R. Junejo, "Comprehensive study and review on maglev train system," *Applied Mechanics and Materials*, vol. 615, pp. 347–351, 2014.

[20] R. Palka and K. Woronowicz, "Linear induction motors in transportation systems," *Energies*, vol. 14, no. 9, p. 2549, 2021.

[21] G. Lv, Z. Zhang, Y. Liu, and T. Zhou, "Characteristics analysis of linear synchronous motor integrated with propulsion, levitation, and guidance in high-speed maglev system," *IEEE Transactions on Transportation Electrification*, vol. 7, no. 4, pp. 3185–3193, 2021.

[22] Z. Liu, Z. Long, and X. Li, *Maglev trains.* Springer, 2015.

[23] H.-S. Han and D.-S. Kim, "Magnetic levitation," *Springer Tracts on Transportation and Traffic. Springer Netherlands*, vol. 247, 2016.

[24] J. Eastham, M. Balchin, P. Coles, and D. Rodger, "Comparison of short primary linear machines for high speed maglev vehicles," *IEEE Transactions on Magnetics*, vol. 23, no. 5, pp. 2338–2343, 1987.

[25] G. Yang and Z. Tang, "The analysis of high-speed wheel-rail train and high-speed maglev train safety systems," in *Proceedings of ICSSSM'05. 2005 International Conference on Services Systems and Services Management, 2005.*, vol. 2, pp. 1403–1407, IEEE, 2005.

[26] T. Sasakawa, N. Tagawa, T. Herai, K. Nagashima, and S. Fujiwara, "A design of magnetic shielding for a superconducting magnetically levitated train," *Electrical Engineering in Japan*, vol. 124, no. 1, pp. 42–54, 1998.

[27] G. Ma, L. Xiao, T. Gong, J. Li, K. Liu, R. Wang, S. Li, J. Xu, Z. Zhao, and Y. Zhai, "Magnetic shielding design of onboard superconducting magnet for electrodynamic suspension train," *IEEE Transactions on Applied Superconductivity*, vol. 33, no. 4, pp. 1–9, 2023.

[28] J.-S. Choi and J. Yoo, "Design of a halbach magnet array based on optimization techniques," *IEEE Transactions on Magnetics*, vol. 44, no. 10, pp. 2361–2366, 2008.

[29] J. F. Hoburg, "Modeling maglev passenger compartment static magnetic fields from linear halbach permanent-magnet arrays," *IEEE transactions on magnetics*, vol. 40, no. 1, pp. 59–64, 2004.

[30] H. Zhu, H. Huang, J. Zheng, H. Shi, Y. Xiang, and K. Li, "A numerical calculation model of multi-magnet-array and 8-shaped null-flux coil for permanent magnet eds vehicle system," *IEEE Transactions on Magnetics*, vol. 58, no. 5, pp. 1–11, 2022.

[31] V. R. Vuchic and J. M. Casello, "An evaluation of maglev technology and its comparison with high speed rail," *Transportation Quarterly*, vol. 56, no. 2, pp. 33–50, 2002.

[32] J. Gou, "Development status and global competition trends analysis of maglev transportation technology based on patent data," *Urban Rail Transit*, vol. 4, no. 3, pp. 117–129, 2018.

[33] N. Prasad, S. Jain, and S. Gupta, "Electrical components of maglev systems: Emerging trends," *Urban Rail Transit*, vol. 5, pp. 67–79, 2019.

[34] M. Ono, S. Koga, and H. Ohtsuki, "Japan's superconducting maglev train," *IEEE Instrumentation & Measurement Magazine*, vol. 5, no. 1, pp. 9–15, 2002.

[35] A. Nakagawa and S. Matsuda, "Status of development and running tests on japan's superconducting maglev," *Transportation research record*, vol. 1916, no. 1, pp. 26–29, 2005.

[36] G. S. Nandkishor, P. P. Hanumant, *et al.*, "Introduction to maglev train a review," *JournalNX*, pp. 130–132, 2018.

[37] J. He, D. Rote, and H. Coffey, "Study of japanese electrodynamic-suspension maglev systems," tech. rep., Argonne National Lab., IL (United States). Energy Systems Div., 1994.

[38] M.-K. Song and Y. Fujino, "Dynamic analysis of guideway structures by considering ultra high-speed maglev train-guideway interaction," *Structural Engineering and Mechanics*, vol. 29, no. 4, pp. 355–380, 2008.

[39] A. Eastham and W. Hayes, "Maglev systems development status," *IEEE Aerospace and Electronic Systems Magazine*, vol. 3, no. 1, pp. 21–30, 1988.

[40] Y. Luguang, "Progress of high-speed maglev in china," *IEEE Transactions on applied superconductivity*, vol. 12, no. 1, pp. 944–947, 2002.

[41] Y. Luguang, "Progress of the maglev transportation in china," *IEEE Transactions on Applied superconductivity*, vol. 16, no. 2, pp. 1138–1141, 2006.

[42] D. Y. Park, B. C. Shin, and H. Han, "Korea's urban maglev program," *Proceedings of the IEEE*, vol. 97, no. 11, pp. 1886–1891, 2009.

[43] H. Martina and K. Johannes, "Disruptive technologies transforming urban mobility? the role of the ecobee urban maglev system in the seoul traffic vision 2030, south korea," , vol. 4, no. 3 S1, pp. 115–123, 2018.

[44] W. Saslow, "Maxwell's theory of eddy currents in thin conducting sheets, and applications to electromagnetic shielding and maglev," *Am. J. Phys*, vol. 60, no. 8, pp. 693–711, 1992.

[45] R. J. Hill, "Teaching electrodynamic levitation theory," *IEEE Transactions on Education*, vol. 33, no. 4, pp. 346–354, 1990.

[46] G. K. Tandan, P. K. Sen, G. Sahu, R. Sharma, and S. Bohidar, "A review on development and analysis of maglev train," *International Journal of Research in Advent Technology*, vol. 3, no. 12, pp. 14–17, 2015.

[47] Q. Han, C. Ham, and R. Phillips, "Four-and eight-piece halbach array analysis and geometry optimisation for maglev," *IEE Proceedings-Electric Power Applications*, vol. 152, no. 3, pp. 535–542, 2005.

[48] Z. Liao, J. Yue, and G. Lin, "Application research of hts linear motor based on halbach array in high speed maglev system," *IEEE Transactions on Applied Superconductivity*, vol. 31, no. 5, pp. 1–7, 2021.

[49] C. Ham, W. ko, and Q. Han, “Analysis and optimization of a maglev system based on the halbach magnet arrays,” *Journal of Applied Physics*, vol. 99, pp. 08P510–08P510, 04 2006.

[50] Y. Jiang, Y. Deng, P. Zhu, M. Yang, and F. Zhou, “Optimization on size of halbach array permanent magnets for magnetic levitation system for permanent magnet maglev train,” *IEEE Access*, vol. 9, pp. 44989–45000, 2021.

[51] W. Jiangbo, L. Chunsheng, X. Wei, and Y. Baofeng, “Optimization design of linear halbach array for eds maglev,” in *2008 IEEE Vehicle Power and Propulsion Conference*, pp. 1–5, IEEE, 2008.

[52] S. Li, “State of art and future development of magnetic levitation technology,” *Highlights in Science, Engineering and Technology*, vol. 31, pp. 167–176, 2023.

[53] M. T. Thompson, R. D. Thornton, and A. Kondoleon, “Flux-canceling electrodynamic maglev suspension: Part i. test fixture design and modeling,” *IEEE transactions on magnetics*, vol. 35, no. 3, pp. 1956–1963, 1999.

[54] T. Akinbiyi, P. Burke, and B. Ooi, “A comparison of ladder and sheet guideways for electrodynamic levitation of high speed vehicles,” *IEEE Transactions on Magnetics*, vol. 12, no. 6, pp. 879–881, 1976.

[55] D. M. Rote, “Passive damping in eds maglev systems.,” tech. rep., Argonne National Lab., IL (US), 2002.

[56] C. Yuwei, H. Guang, and L. Zhiqiang, “Vertical dynamic stability analysis of eds levitation systems based on halbach magnet arrays,” in *2009 Chinese Control and Decision Conference*, pp. 3726–3730, IEEE, 2009.

[57] R. F. Post and D. D. Ryutov, “The inductrack: a simpler approach to magnetic levitation,” *IEEE Transactions on applied superconductivity*, vol. 10, no. 1, pp. 901–904, 2000.

[58] T. Murai and H. Hasegawa, “Electromagnetic analysis of inductrack magnetic levitation,” *Electrical Engineering in Japan*, vol. 142, no. 1, pp. 67–74, 2003.

[59] L. Hoppie, F. Chilton, H. Coffey, and R. Singleton, “Electromagnetic lift and drag forces on a superconducting magnet propelled along a guideway composed of metallic loops,” tech. rep., Stanford Research Inst., Menlo Park, CA, 1972.

[60] J. Powell, “High-speed transport by magnetically suspended trains,” *ASME paper*, vol. 66, p. 1, 1966.

[61] J. R. Powell and G. Danby, “Magnetically suspended trains: The application of superconductors to high speed transport,” *Cryogenics and Industrial Gases*, vol. 4, no. 10, pp. 19–24, 1969.

[62] O. F. Storset and B. E. Paden, “Discrete track electrodynamic maglev part i: Modelling,” *IEEE Transactions on Magnetics*, pp. 410–447, 2005.

[63] H. A. Wheeler, “Formulas for the skin effect,” *Proceedings of the IRE*, vol. 30, no. 9, pp. 412–424, 1942.

[64] K. Halbach, “Application of permanent magnets in accelerators and electron storage rings,” *Journal of Applied Physics*, vol. 57, no. 8, pp. 3605–3608, 1985.

[65] J. Lim, C.-Y. Lee, Y. J. Oh, J.-M. Jo, J.-H. Lee, K.-S. Lee, and S. Choi, “Equivalent inductance model for the design analysis of electrodynamic suspension coils for hyperloop,” *Scientific reports*, vol. 11, no. 1, p. 23499, 2021.

[66] M. P. Bendsoe and O. Sigmund, *Topology optimization: theory, methods, and applications*. Springer Science & Business Media, 2013.

[67] O. Sigmund and K. Maute, “Topology optimization approaches: A comparative review,” *Structural and multidisciplinary optimization*, vol. 48, no. 6, pp. 1031–1055, 2013.

[68] G. I. Rozvany, “A critical review of established methods of structural topology optimization,” *Structural and multidisciplinary optimization*, vol. 37, pp. 217–237, 2009.

[69] M. P. Bendsøe and N. Kikuchi, “Generating optimal topologies in structural design using a homogenization method,” *Computer methods in applied mechanics and engineering*, vol. 71, no. 2, pp. 197–224, 1988.

[70] F. Campelo, J. Ramirez, and H. Igarashi, “A survey of topology optimization in electromagnetics: considerations and current trends,” *Academia*, vol. 46, p. 2010, 2010.

[71] K. Nomura, S. Yamasaki, K. Yaji, H. Bo, A. Takahashi, T. Kojima, and K. Fujita, “Topology optimization of conductors in electrical circuit,” *Structural and Multidisciplinary Optimization*, vol. 59, pp. 2205–2225, 2019.

[72] Y. Li, *Numerical methodologies for topology optimization of electromagnetic devices*. PhD thesis, Sorbonne Université; Zhejiang University (Hangzhou, Chine), 2019.

[73] P. Gangl and U. Langer, “Topology optimization of electric machines based on topological sensitivity analysis,” *Computing and Visualization in Science*, vol. 15, pp. 345–354, 2012.

[74] S. Sanogo and F. Messine, "Topology optimization in electromagnetism using simp method: Issues of material interpolation schemes," *COMPEL-The international journal for computation and mathematics in electrical and electronic engineering*, vol. 37, no. 6, pp. 2138–2157, 2018.

[75] F. Lucchini, R. Torchio, V. Cirimele, P. Alotto, and P. Bettini, "Topology optimization for electromagnetics: A survey," *IEEE Access*, vol. 10, pp. 98593–98611, 2022.

[76] J. K. Guest and J. H. Prévost, "Topology optimization of creeping fluid flows using a darcy–stokes finite element," *International Journal for Numerical Methods in Engineering*, vol. 66, no. 3, pp. 461–484, 2006.

[77] G. Marck, M. Nemer, and J.-L. Harion, "Topology optimization of heat and mass transfer problems: laminar flow," *Numerical Heat Transfer, Part B: Fundamentals*, vol. 63, no. 6, pp. 508–539, 2013.

[78] G. H. Yoon, J. S. Jensen, and O. Sigmund, "Topology optimization of acoustic–structure interaction problems using a mixed finite element formulation," *International journal for numerical methods in engineering*, vol. 70, no. 9, pp. 1049–1075, 2007.

[79] M. B. Dühring, J. S. Jensen, and O. Sigmund, "Acoustic design by topology optimization," *Journal of sound and vibration*, vol. 317, no. 3-5, pp. 557–575, 2008.

[80] A. J.-M. Thabuis, "Computational design and additive manufacturing of electromagnetic coils," tech. rep., EPFL, 2023.

[81] K. Svanberg, "The method of moving asymptotes—a new method for structural optimization," *International journal for numerical methods in engineering*, vol. 24, no. 2, pp. 359–373, 1987.

[82] C. Zillober, "A globally convergent version of the method of moving asymptotes," *Structural optimization*, vol. 6, pp. 166–174, 1993.

[83] A. Deetman, "Gcmma-mma-python: Python implementation of gcmma and mma optimization algorithms." https://github.com/arjendeetman/GCMMA-MMA-Python/tree/master. Accessed: August 10, 2024.

[84] R. El Bechari, F. Guyomarch, and S. Brisset, "The adjoint variable method for computational electromagnetics," *Mathematics*, vol. 10, no. 6, p. 885, 2022.

[85] D. Givoli, "A tutorial on the adjoint method for inverse problems," *Computer Methods in Applied Mechanics and Engineering*, vol. 380, p. 113810, 2021.

[86] M. L. . Simulation, "Adjoint method for pde-constrained optimization | pde-constrained optimization," 2022. Accessed: August 10, 2024.

[87] M. P. Bendsøe and O. Sigmund, "Material interpolation schemes in topology optimization," *Archive of applied mechanics*, vol. 69, pp. 635–654, 1999.

[88] G. Allaire, F. Jouve, and A.-M. Toader, "Structural optimization using sensitivity analysis and a level-set method," *Journal of computational physics*, vol. 194, no. 1, pp. 363–393, 2004.

[89] S. Zhou, W. Li, and Q. Li, "Level-set based topology optimization for electromagnetic dipole antenna design," *Journal of Computational Physics*, vol. 229, no. 19, pp. 6915–6930, 2010.

[90] H. Shim, V. T. T. Ho, S. Wang, and D. A. Tortorelli, "Level set-based topology optimization for electromagnetic systems," *IEEE transactions on magnetics*, vol. 45, no. 3, pp. 1582–1585, 2009.

[91] C. Dumont de Chassart, B. Dehez, and V. Kluyskens, "Fully analytical determination of inductances in windings with axial and azimuthal wires," in *ISEF 2013-XVI International Symposium on Electromagnetic Fields in Mechatronics, Electrical and Electronic Engineering*, 2013.

[92] C. Dumont de Chassart, M. Van Beneden, V. Kluyskens, and B. Dehez, "Semi-analytical determination of inductances in windings with axial and azimuthal wires," *COMPEL: The International Journal for Computation and Mathematics in Electrical and Electronic Engineering*, vol. 35, no. 1, pp. 2–15, 2016.

UNIVERSITÉ CATHOLIQUE DE LOUVAIN
École polytechnique de Louvain
Rue Archimède, 1 bte L6.11.01, 1348 Louvain-la-Neuve, Belgique | **www.uclouvain.be/epl**